

**EXTRACTING MATERIAL RESPONSE FROM SIMPLE
MECHANICAL TESTS ON HARDENING-SOFTENING-HARDENING
VISCOPLASTIC SOLIDS**

Thesis by
Nisha Mohan

In Partial Fulfillment of the Requirements for the degree of
Doctor of Philosophy



CALIFORNIA INSTITUTE OF TECHNOLOGY

Pasadena, California

2014

(Defended April 3, 2014)

Dedicated to my family and well-wishers, for their undaunted faith in me.

Acknowledgements

My graduate experience has been profoundly memorable. There have been many architects who have helped me think deeply about scientific problems and formulate them more rigorously. They also influenced me retain the other facets of my personality in balance, and I would like to thank them here.

The two most important people, my advisors Professors Julia R. Greer and Alan Needleman molded me into the person I am now. I express my utmost gratitude to Professor Julia R. Greer, for giving me the opportunity, guidance, and freedom to pursue my research project. She has provided me with a multidisciplinary research experience and an opportunity to be a part of the scientific community in workshops and conferences from which I have learned a lot. She has taught me to focus in any specific work in a well-organized manner. She has inspired my scientific thinking to be rigorous from the first day for which I am extremely thankful. Her motivating words have always encouraged me to take that extra step forward and think widely in research.

Prof. Needleman devoted enough time to advise me despite mail being the only feasible communication. In all my computational and theoretical glitches, he gave me the freedom to handle the complete problem with nominal hints. His style of answering my questions with deeper questions helped me explore out the answers on my own. He always inspired me to be analytical in questioning the conceivable errors in my assumptions. One of his adages, that I remember distinctly is that *'being a scientist gives you the right to be wrong'* and of course with the caution not to take advantage of it. I do feel honored to have worked under this inspiring combination. Through the years, they stayed empathetic and patient with me through my follies.

My thesis committee members Professors, Julia R. Greer, Michael Ortiz, Dennis M. Kochmann, Guruswami Ravichandran, and Sergio Pellegrino, are to be thanked for cautiously reading through my work, and also for being of excellent guidance. Particularly I am grateful to Prof. Dennis M. Kochmann for his time and guidance in helping me answer some last minute questions. I hope this thesis and the rest of my career live up to the faith Professors P.Baskaran, K.Padmanaban, and Rajakuperan have in me. My works today root back to the unparalleled guidance from them throughout my bachelors back in India.

Thanks to my lab-mates, for reminding me of the bigger picture, when I got lost into the modeling mode. It helped me rethink if I was actually answering the question I intended to, or if I was under the mere satisfaction of meaningful numbers. They made my stay in the group a cherishing and pleasant one.

My senior post-docs deserve a mention here. Dr. Siddhartha Pathak and I shared similar curiosities, debating about general science. He taught me that sometimes it is not bad to get crazy amidst research and try crazy new things. Dr. Shelby B. Hutchens was a seasoned mentor, who volunteered to save me from so many troubles by correcting my communication and language at times. I consider them to be the architects of the initial times of my research.

Winchell sessions with Pinaky Bhattacharyya, Sujeet Shukla and Vikas Trivedi, helped retain my intellectual identity. Amanda Shing, Subramanyam Duvuri, Rajkumar Palaniappan, Ramya K V, and Ramla Gabriel were awesome friends who kept my craziness alive. This list extends to all my friends. Last but not the least, I thank my parents, Mahalakshmi Ramadoss & Mohan Jayaraman and my brother Ajay Mohan without whom it would have been impossible to chase my dreams.

I would also like to express my gratitude to Cheryl Gause, Legaspi Tess, Cecilia Gamboa, and Christine Ramirez and the GALCIT members, who have facilitated a smooth transition into the Caltech community. I have to particularly thank Felicia Hunt, who has strongly contributed to the successful completion of my graduate study. I would also thank the Institute for Collaborative Biotechnologies (ICB) at Caltech (ARO Award #UCSB.ICB4b) for the funding for my graduate work.

Abstract

Compliant foams are usually characterized by a wide range of desirable mechanical properties. These properties include viscoelasticity at different temperatures, energy absorption, recoverability under cyclic loading, impact resistance, and thermal, electrical, acoustic and radiation-resistance. Some foams contain nano-sized features and are used in small-scale devices. This implies that the characteristic dimensions of foams span multiple length scales, rendering modeling their mechanical properties difficult. Continuum mechanics-based models capture some salient experimental features like the linear elastic regime, followed by non-linear plateau stress regime. However, they lack mesostructural physical details. This makes them incapable of accurately predicting local peaks in stress and strain distributions, which significantly affect the deformation paths. Atomistic methods are capable of capturing the physical origins of deformation at smaller scales, but suffer from impractical computational intensity. Capturing deformation at the so-called meso-scale, which is capable of describing the phenomenon at a continuum level, but with some physical insights, requires developing new theoretical approaches.

A fundamental question that motivates the modeling of foams is ‘how to extract the intrinsic material response from simple mechanical test data, such as stress vs. strain response?’ A 3D model was developed to simulate the mechanical response of foam-type materials. The novelty of this model includes unique features such as the hardening-softening-hardening material response, strain rate-dependence, and plastically compressible solids with plastic non-normality. Suggestive links from atomistic simulations of foams were borrowed to formulate a physically informed hardening material input function. Motivated by a model

that qualitatively captured the response of foam-type vertically aligned carbon nanotube (VACNT) pillars under uniaxial compression [2011, “*Analysis of Uniaxial Compression of Vertically Aligned Carbon Nanotubes*,” *J. Mech.Phys. Solids*, 59, pp. 2227–2237, Erratum 60, 1753–1756 (2012)], the property space exploration was advanced to three types of simple mechanical tests: 1) uniaxial compression, 2) uniaxial tension, and 3) nanoindentation with a conical and a flat-punch tip. The simulations attempt to explain some of the salient features in experimental data, like

- 1) The initial linear elastic response.
- 2) One or more nonlinear instabilities, yielding, and hardening.

The model-inherent relationships between the material properties and the overall stress-strain behavior were validated against the available experimental data. The material properties include the gradient in stiffness along the height, plastic and elastic compressibility, and hardening. Each of these tests was evaluated in terms of their efficiency in extracting material properties. The uniaxial simulation results proved to be a combination of structural and material influences. Out of all deformation paths, flat-punch indentation proved to be superior since it is the most sensitive in capturing the material properties.

Table of Contents

EXTRACTING MATERIAL RESPONSE FROM SIMPLE MECHANICAL TESTS ON HARDENING-SOFTENING-HARDENING VISCOPLASTIC SOLIDS	i
<i>Acknowledgements</i>	iv
<i>Abstract</i>	vi
Chapter 1	1
Introduction	1
1.1 Compliant Foams	2
Here the meso-scale mechanical response is an outcome of the integrated response of the individual properties of each nanotube and the collective response from the interactions between them.....	4
1.2 Mechanical Testing.....	4
1.3 Viscoplastic Material Modeling	5
1.4 Motivation.....	7
Chapter 2	10
Literature Review.....	10
2.1 Compression Models	10
2.2 Tensile Models.....	14
2.3 Nanoindentation Models.....	15
2.4 Atomistic Linkage Model	16
Chapter 3	20
Finite Element Model.....	20
3.1 Model Description	20
3.2 Model Formulation	21
3.2.1 Mesh Induced Numerical Effects	22
3.3 Constitutive Setup & Flow-Stress Function	26

3.4 Morphological Linkage.....	30
3.5 Basis of Output Analysis	33
Chapter 4	34
Compression Test.....	34
4.1 Introduction.....	34
4.2 Model Results vs. Experiments	34
4.2.1 Experimental Analysis.....	34
4.2.2 Deriving Relative Density: Image Analysis	39
4.2.3 Model Results	41
Chapter 5	49
Tension Test.....	49
5.1 Introduction.....	49
5.2 1D Model Analysis	50
5.3 Instability Analysis	54
5.3.1 Diffuse Necking Instability	54
5.3.2 Localized Necking Instability.....	57
5.3.3 Propagating Band Instability	59
5.4 Material Gradient Effects	62
5.5 Summary of Tensile Results.....	64
Chapter 6	66
Nanoindentation	66
6.1 Introduction.....	66
6.2 3D Model Setup.....	69
6.3 Conical Indentation.....	72
6.4 Flat-Punch Indentation.....	81
6.5 Material Inhomogeneity: Strength Gradient Effects	85
6.6 Material Space (Flow Stress) Exploration.....	86

Chapter 7	93
Comparative Study and Conclusions	93
7.1 Introduction.....	93
7.2 Summary	94
7.2.1 Strength Gradient.....	95
7.2.2 Hardening Function	96
7.2.3 Near and Plastic Compressibility	97
7.2.4 Plastic Normality	99
7.3 Conclusion and Future Work.....	99
Appendix A	102
Appendix B	105
Bibliography.....	115

List of Figures

- Figure 1:* SEM images of VACNT film over a substrate, at two different length-scales of (a) vertically aligned anisotropic tubes at length-scale of $> 100\mu\text{m}$ and (b) inter-twinned network of tubes at length-scale of $<10\ \mu\text{m}$ (Reprint under permissions from Dr. Shelby B. Hutchens and Dr. Siddhartha Pathak [5]) illustrating the hierarchical nature. 3
- Figure 2:* TEM images of VACNT film over a substrate, at two different length-scales of (a) isotropic network of tubes at a length-scale of $< 1\mu\text{m}$ and (b) individual nanotube at a length-scale of 1 nm (Reprint under permissions from Dr. Shelby B. Hutchens and Dr. Siddhartha Pathak [5]) illustrating the hierarchical nature. 3
- Figure 3:* A typical stress-strain curve for an elastic-plastic foam undergoing uniaxial compression showing the three distinct elastic, plateau, and densification regimes [2]. 8
- Figure 4:* (a) Compression and (b) Tensile responses from Molecular Dynamics simulation of Coiled Carbon Nanotubes (CCNTs) [45]. 17
- Figure 5:* (a) Typical initial undeformed finite element mesh showing the axis of symmetry (in green dot-dash line), the radius, R_0 and the total height, H_0 , (b) an illustration of mesh induced numerical instabilities. 22
- Figure 6:* The typical definition of the hardening-softening-hardening flow stress function with the transition strains denoted by ϵ_1 & ϵ_2 and the slopes of the three-piecewise linear functions given by h_1 , h_2 & h_3 , respectively. 27
- Figure 7:* SEM images of the foam pillars taken at 60 deg tilt angle. (a) Square Pillars on the substrate edge, (b) Circular Pillars on the substrate interior (Reprint under permissions, ACS Nano.) [62]. 35
- Figure 8:* Comparison of the stress-strain responses of two VACNT pillar systems grown on the same substrate. While the square pillars in (a) show a heavily sloped

plateau region, the same for the circular pillars shown in (b) is almost flat (as in foams) (Reprint under permissions, ACS Nano.)[62]..... 36

Figure 9: Evolution of deformation under compression shown as a series of SEM images at consecutive strains, for the two different material setups (a) pillars on the substrate edge, (b) pillars on the substrate interior (Reprint under permissions, ACS Nano.)[62]. 37

Figure 10: (a) Three variations of the SM function used in simulations and (b) their corresponding output stress-strain responses, reflecting a suggested reason for a sloped plateau phenomena to be the material inhomogeneity over the height of the pillar (Reprint under permissions, ACS Nano.)[62]..... 42

Figure 11: Plot of the hardening slope of the plateau regime vs. % Δ SM over the height of the pillar, showing a linear relationship. (Reprint under permissions, ACS Nano.)[62]. 43

Figure 12: Comparison of case 1 (green curve, representing circular pillar) vs. case 4 (step variation in SM, representing square pillar) and their corresponding stress-strain responses with an inset of the experimental curves. (Reprint under permissions, ACS Nano.)[62]. 44

Figure 13: Simulation results showing the evolution of the outer deformation profiles corresponding to the four different SM functions shown before. The deformation profiles are shown at progressive strains of 5, 10, 20, 30 and 40% s. 46

Figure 14: Strain rate contour plots for case 1 at four consecutive strains, showing the observed phenomena of the sequential buckling evolution..... 46

Figure 15: Plot of flow stress function with the Maxwell equivalent flow stress and the area equivalence terms shown..... 53

Figure 16: The hardness function as a function of plastic strain, (a) for material A ($h_2 = 5.0$, $h_3 = 15.0$, and $\epsilon_2 = 0.6$) and for material B ($h_2 = 5.0$, $h_3 = 5.0$, and $\epsilon_2 = 0.6$) and (b) their output stress-strain response. 55

Figure 17: Distributions of normalized plastic strain rate for material A(a& b) and B(c & d): (a) $\varepsilon_t = 0.50$ and (b) $\varepsilon_t = 0.76$ 56

Figure 18: (a) The hardness function for material B ($h_2 = 5.0$, $h_3 = 5.0$, and $\varepsilon_2 = 0.6$), material C ($h_3 = h_2 = 1.0$) and material D ($h_3 = h_2 = 0.5$) and (b) their respective output response. 57

Figure 19: Distributions of normalized plastic strain rate (a) material C at $\varepsilon_t = 0.3$ and (b) material D at $\varepsilon_t = 0.14$ 58

Figure 20: (a) The hardness function for material E ($h_2 = -3.90$, $h_3 = 5.0$, $\varepsilon_2 = 0.6$), material F ($h_2 = 0.5$, $h_3 = 15.0$, $\varepsilon_2 = 0.6$), material G ($h_2 = -3.90$, $h_3 = 15.0$, $\varepsilon_2 = 5.0$), and (b) the output response for Material E. 60

Figure 21: Distributions of normalized plastic strain rate material E (a) at $\varepsilon_t = 0.2$ (b) at $\varepsilon_t = 0.3$ and (c) at $\varepsilon_t = 0.5$ 61

Figure 22: Three Cases:1-3. (a) SM functions input, (b) the respectively normalized stress-strain curves of the three cases plotted..... 63

Figure 23: The typical stress-strain response of three modes of tensile deformation shown in the first row (a, b & c). The normalized plastic strain rate contour plots show the three distinct modes of instability in the second row (d, e & f)..... 64

Figure 24: Experimental indentations at different displacement rates showing a large displacement burst and more pronounced buckling signatures at the faster rates for foams. The inset images show the residual impressions of indentation [60]. 69

Figure 25: Plot of the normalized hardening functions $g(\varepsilon_p)$ used in the calculations..... 71

Figure 26: Nominal hardness, $H_{nom} = P/A_{nom}$, versus normalized indentation depth h/l , for a conical indenter with (a) $\phi = 9.5^\circ$, and (b) $\phi = 19.0^\circ$ 73

Figure 27: Nominal hardness, $H_{nom} = P/A_{nom}$, versus normalized indentation depth h/l , for a conical indenter with $\phi = 24.7^\circ$ 73

- Figure 28:* Contour distributions of the normalized plastic strain rate in the proximity of the indenter for (a) Mat. A with $\phi=9.5^\circ$ and $h/l=0.04$, (b) Mat. A with $\phi=24.7^\circ$ and $h/l=0.04$ 74
- Figure 29:* Ratio of true to nominal contact area, A/A_{nom} , versus indentation depth h/l , for a conical indenter with (a) $\phi=9.5^\circ$, and (b) $\phi=19.0^\circ$ 75
- Figure 30:* Ratio of true to nominal contact area, A/A_{nom} , versus indentation depth h/l , for a conical indenter with $\phi=24.7^\circ$ 76
- Figure 31:* Overall stress-strain response in uniaxial compression for materials A, B and C [65]. 77
- Figure 32:* Nominal hardness, $H_{\text{nom}} = P/A_{\text{nom}}$, versus indentation depth h/l , for a conical indenter with $\phi=19^\circ$, (a) with plastic incompressibility ($\beta_p = 0.33$) and (b) with near incompressibility ($\beta_p = 0.33$, $\nu = 0.49$). 78
- Figure 33:* Nominal hardness, $H_{\text{nom}} = P/A_{\text{nom}}$, versus indentation depth h/l , for a conical indenter with $\phi=19^\circ$, with near incompressibility ($\alpha_p = 0.33$, $\beta_p = 0.33$ & $\nu = 0.49$). 79
- Figure 34:* Nominal hardness, $H_{\text{nom}} = P/A_{\text{nom}}$, versus normalized indentation depth h/w , for a flat square indenter with (a) default $\beta_p = 0.28$, and (b) $\beta_p = 0.33$ 82
- Figure 35:* Nominal hardness, $H_{\text{nom}} = P/A_{\text{nom}}$, versus normalized indentation depth h/w , (a) for a flat square indenter near incompressibility, and (b) with plastic normality. 83
- Figure 36:* Contour distributions of the normalized plastic strain rate in the proximity of the indenter for (a) Mat. A, default at $h/w=0.28$, (b) Mat. A with incompressibility and plastic normality at $h/w=0.28$ 84
- Figure 37:* Plot of normalized hardness noted at a series of different punch displacements (legends indicate the hardness as a series at consecutive normalized punch displacement, h/l) vs. the percent of strength variation over the height of the material. 86

- Figure 38:* A schematic showing the methodology used to move the minima position in the directions of the arrows, indicating changes in depth and width of the minima..... 87
- Figure 39:* Plot of normalized hardness (H/σ_0) vs. normalized punch displacement (u/p), with each colored curve representing responses of individual cases of G (depth of minima). 88
- Figure 40:* The side view schematic of the 3-D contour plot of the cumulative plastic strain shown. The radius, r and depth, d of the plastic zone are shown, normalized with the side length, w and total height, h of the model respectively. 89
- Figure 41:* The plot of (a) normalized radius, r/w vs. punch displacement, u/p and (b) normalized depth, d/h of the ring of plastic zone formed vs. the normalized punch displacement, u/p as a series with respect to the minima depth increasing from ' $G=0.1$ ' to ' $G=0.9$ ' 90
- Figure 42:* The plot of (a) normalized radius, r/w vs. punch displacement, u/p and (b) normalized depth, d/h of the ring of plastic zone formed with the normalized punch displacement, u/p as a series with respect to the minima width increasing from ' $E2=0.1$ ' to ' $E2=0.5$ ' 91

Chapter 1

Introduction

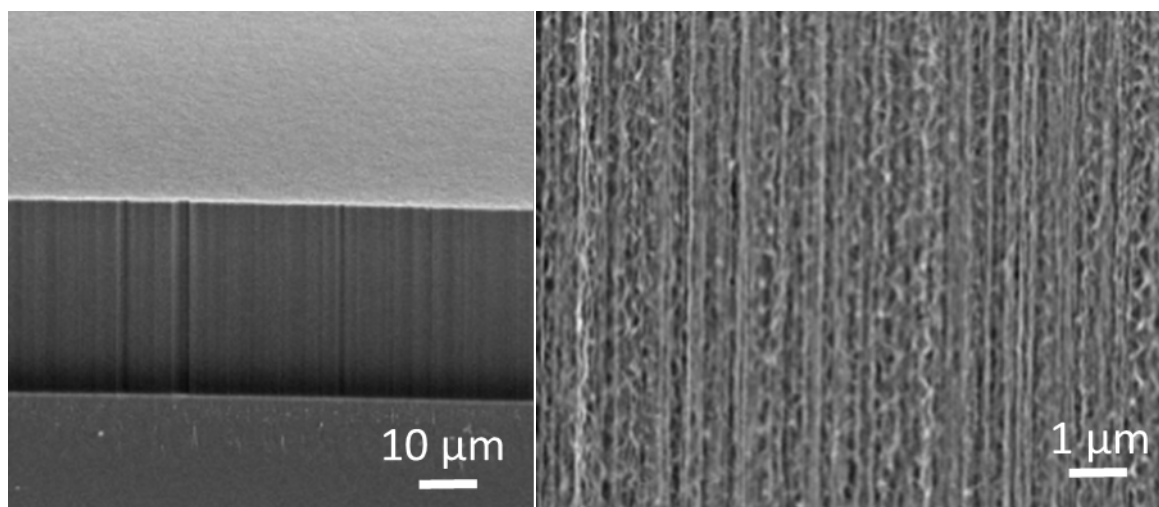
In theoretical mechanics-based approaches, modeling of a material's mechanical behavior spanning multiple length scales requires different theoretical methods. Computational chemistry (MD, DFT techniques)[1] and continuum mechanics are the best-known approaches for investigation of sub-microscopic and macroscopic properties respectively. Compliant foams are usually characterized by a wide range of desirable mechanical properties. These properties include viscoelasticity at different temperatures, energy absorption, recoverability under cyclic loading, impact resistance and thermal, electrical, acoustic and radiation-resistance and like.

Some foams containing nano-sized features are applied in meso to macroscopic devices. This implies a large difference in the length scales which subsequently renders the modeling of their meso-scale mechanics difficult. Continuum mechanics-based models capture some salient experimental features, like the linear elastic regime, followed by non-linear plateau stress. However, they lack mesostructural physical details. This makes them incapable of accurately predicting local peaks in stress and strain distributions that significantly affect the deformation paths. Atomistic methods are capable of capturing the physical origins of deformation at smaller scales, but suffer from impractical computational intensity. Capturing deformation at the so-called meso-scale, which is capable of describing the phenomenon at a continuum level but with some physical insights,

requires developing new theoretical approaches. A fundamental question that motivates modeling of foams is ‘how to extract the intrinsic material response from simple mechanical test data such as stress vs. strain response?’ Hence we attempt to formulate and test a mathematically motivated continuum model, to capture the mechanical behavior of foam-type materials.

1.1 Compliant Foams

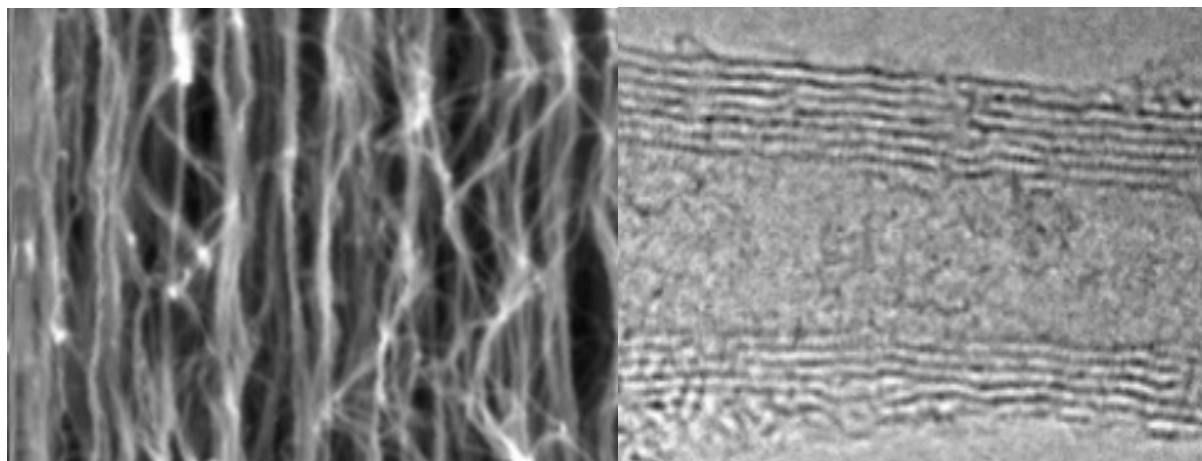
Compliant foam-like materials include examples such as polymeric foams, cellular solid-type foams, carbon nanotube foam systems and the like. Sponges and corals are examples of such naturally present compliant materials. These are interesting for their energy absorption mechanism [2] and the highly desired thermal, electrical, acoustic and radiation-resistant properties [3]. In crystalline solids, the evolution of surfaces, grain-boundaries, and dislocations under applied stress define the plasticity and yielding criteria of the material. Unlike crystalline solids, foams possess non-monolithic simpler repeating structure. They still show rich mechanical behavior within elastic or inelastic domains [2]. The source and mechanism of plasticity of these two systems differ greatly. Polymeric foams undergo predominantly undergo elastic deformation, whereas metallic foams are dominated by plastic deformation. Another example of foam behavior is the deformation of vertically aligned carbon nanotube tufts (VACNTs) which are predicted to exhibit plastic compressibility and plastic non-normality [4]. Mechanical response of such foam materials is a complex phenomenon due to its hierarchical microstructure spanning over multiple-length scales, as in the example of VACNTs shown in Figure 1 and Figure 2.



(a)

(b)

Figure 1: SEM images of VACNT film over a substrate, at two different length-scales of (a) vertically aligned anisotropic tubes at length-scale of $> 100\mu\text{m}$ and (b) inter-twinned network of tubes at length-scale of $<10\ \mu\text{m}$ (Reprint under permissions from Dr. Shelby B. Hutchens and Dr. Siddhartha Pathak [5, 6]) illustrating the hierarchical nature.



(a)

(b)

Figure 2: TEM images of VACNT film over a substrate, at two different length-scales of (a) isotropic network of tubes at a length-scale of $< 1\mu\text{m}$ and (b) individual nanotube at a length-scale of 1 nm (Reprint under permissions from Dr. Shelby B. Hutchens and Dr. Siddhartha Pathak [5, 6]) illustrating the hierarchical nature.

Here the meso-scale mechanical response is an outcome of the integrated response of the individual properties of each nanotube and the collective response from the interactions between them.

1.2 Mechanical Testing

Mechanical response of meso-scale materials is captured through a variety of mechanical tests, including uniaxial (compression and tensile) loading tests, nanoindentation, bending moment tests, plane strain or stress tests and notched fracture testing. Here, simple mechanical tests, modeled and investigated for foams are given as follows.

- 1) uniaxial compression,
- 2) uniaxial tension, and
- 3) indentation with conical and flat-punch tips.

This also helps in understanding the capability of such tests in characterizing the material properties from the simplest mechanical response data, such as the stress vs. strain response. The material properties include the gradient in stiffness along the vertical height, plastic and elastic compressibility, and hardening (explained in following chapters). The following reasons justify this choice of simple tests. Uniaxial compressive and tensile tests are motivated by the required understanding for energy absorption and dissipation applications.

Unlike under uniaxial compression, under nanoindentation, contact mechanics between the indenter tip and material surface, and free surface effects come into major play [7]. 3D effects and stress concentrations occur below the indenter's tip, and corresponding strain gradients are also formed [7]. This is expected to help in the capturing of the material properties, to which the uniaxial tests might be insensitive. The ratio of indentation hardness to compressive strength is one of the figures of merit, interesting for material characterization. This ratio is affected by

the material constitutive setup and hence it would be an interesting comparison with the ratios of other material constitutive setups, such as an elastic-plastic setup [8].

1.3 Viscoplastic Material Modeling

Since the modeling of compliant foam-type materials was intended, viscoplastic material setup was preferred at the outset. The general viscoplastic constitutive material model is defined as an equation relating plastic stress to plastic strain. This equation is rate-dependent and, if suitable, is expressed as a function of strain history, and other state variables. It is hard to derive the equations from the basic first principles and can only be derived from the experimental results of the relevant material. Viscoplastic constitutive equations are generally used to model the deformation behavior of materials that are deformed at high rates of strain, sensitive to strain-rate, and possess pressure-sensitive flow strength.

This formulation is highly dependent on the physical observations (from experimental results) that govern the mechanical response of the solid. However, there are two necessary regulations, which set boundaries that restrict the formulation freedom. They serve to verify the models validity. The first physical regulation is that the model has to satisfy the laws of thermodynamics. The first law of thermodynamics requires that the mechanical work done by applied stress must either be stored as recoverable internal elastic energy in the solid or mostly dissipated as heat [9]. The second thermodynamics law requires that under cyclic loading that starts and ends at an identical strain and internal energy (in adiabatic cases), the total work done must be positive or zero. The second physical regulation is that, the model must satisfy the condition of objectivity, or material

frame indifference. Significant other rules are also suggested to assure a unique solution to the problem and plastic stability, e.g., the Drucker's stability criteria [10].

Drucker's postulate is a combination of the normality condition and the convexity of the yield stress surface. It sets a maximum bound on the dissipation and hence stabilizes the material model. However, there are a few plasticity cases of materials like aluminum and steel which do not obey Drucker's postulate [11]. In addition, the preference of using the plastic normality condition in this particular model will be discussed in following sections. Material systems which do not follow this normality criterion also exist, e.g., geoplastic modeling of soils, anisotropic materials, and crystal plasticity models [12]. Therefore, these rules are preferred or disregarded in accordance with reference to the known material information.

Viscoplastic constitutive equations mainly consist of the following:

1. Strain rate decomposition into elastic and plastic components.

$$d_{ij} = d_{ij}^e + d_{ij}^p \quad (1)$$

2. Elastic stress-strain law.

$$d_{ij}^e = L_{ijkl}^{-1} \hat{t}_{kl} \quad (2)$$

3. Plastic flow potential, which determines the magnitude of the plastic strain rate, given the stresses, and resistance of the material to flow.

$$\dot{\epsilon}_p = \dot{\epsilon}_o (\sigma_e / g)^{1/m} \quad (3)$$

4. State variables, which characterize the resistance of the material to flow. The flow stress function is used as the state variable (g).

5. The plastic flow rule, which defines the components of plastic strain rate under loading. (see Chapter 3, for more details.)

6. Hardening laws that specify the evolution of the state variables with plastic strain, which is tailored for the materials used as specified under the previous physical regulations. (see Chapter 3, for more details.)

Flow plasticity theories are based on the assumption that a flow rule exists, and is used to determine the amount of plastic deformation with respect to plastic strain in the material. The flow stress functions can be visualized as the relative field of yield strength as a function of the plastic strain. It can also be physically defined as the instantaneous stress required for continued plastic deformation at any instant. Plasticity theories for rocks and concrete is one area where usage of pressure-dependent flow strength is required [11]. The detailed formulation of the specific viscoplastic model used here is explained in the following chapter.

1.4 Motivation

Polymeric foams are widely used as core materials for sandwich structures in automotive and aerospace industries. For example, they are used in crash padding of aircraft cockpit structures due to their high specific stiffness, and strength to weight ratios [2]. A variety of foams are also used in non-structural applications for cushioning, packaging, and insulating purposes because of their energy absorbing properties, good vibration resistance, and thermal and acoustic insulations [2]. The high strength of polymeric foams does not assure significant toughness. As soon as the yield point is reached, an individual cell layer/chain link/tubular connection will fail quickly with little dissipation of energy. Before we try to understand the complex interactions within composites, foam networks, and

the polymer matrix, the deformation mechanism at the meso-scale of foams needs to be understood well and that is where we concentrate our effort in this work.

Applications include components of highly compliant thermal contacts for micro-electro-mechanical-systems (MEMS) and microelectronics [13], dry adhesives [14, 15], thermally robust energy dissipating system [16-18], and energy absorption or impact mitigation [19-21]. The stress-strain behavior of foams is very different from that of metals. The onset of plastic yielding tends to occur at a stress peak followed by a lower stress level (plateau) during continued plastic flow [22].

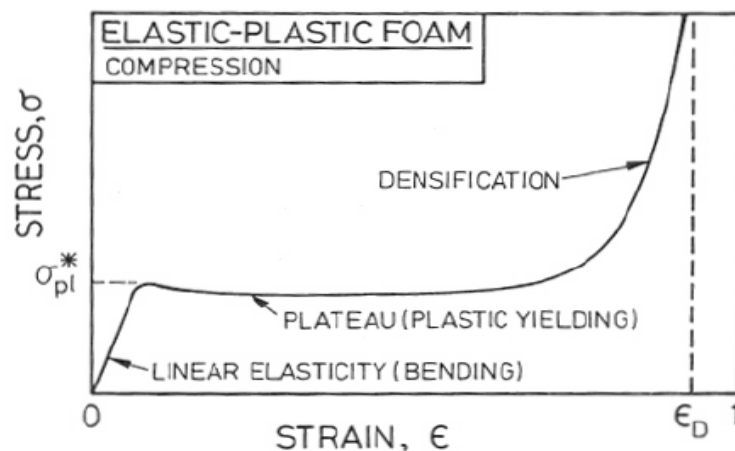


Figure 3: A typical stress-strain curve for an elastic-plastic foam undergoing uniaxial compression showing the three distinct elastic, plateau, and densification regimes [2].

The typical mechanical response of foams and cellular materials under compression has features (Figure 3) such as

1. The initial elastic deformation regime.
2. The first significant stress drop, signifying the initiation of the plateau region of stress, after which the plastic deformation starts.

3. The plateau region of stress with or without undulations in the curve that would correspond to some series of physical deformation. For example, consecutive cellular structure collapses (in materials like open cell-foams), indicating instability.

4. The unloading curve of different polymers, which shows varied trends from near-complete recovery to non-recovery.

This model aimed to capture the prominent features known from previous experimental reports. The possible correspondence of the model predictions under simple tests as uniaxial compression/tension and nanoindentation will contribute to the design of this material for relevant applications.

Also, it would be beneficial to evaluate the simple mechanical tests based on their sensitivity in correlation with each of the individual material properties. This would lead to an efficient way of characterizing the microstructural properties of materials and will help design materials with built-in hierarchy [5]. This work is meant to be a precursor for the in-depth understanding of the physicality of simple mechanical tests and their effectiveness in characterizing a material.

Chapter 2

Literature Review

An overview of existing literature reports is presented in this section. The inadequate number of mesoscale models of foam-type materials was a major motivation for this work. In this work, a 3D model was used, which levels over the discrete nature of the individual unit cells. Hence, it approximates the overall material setup to be an isotropic continuum constitutive relation, which is in the similar lines of the Deshpande-Fleck constitutive relation for foams [23]. This model differs from other foam models, for example, [13, 16, 24] in assuming the material setup to be an isotropic continuum one. The details of other such models and the unique features captured by them are summarized in this section.

The existing models for foams under each of the deformation paths (uniaxial compression, uniaxial tension, and indentation) can be categorized under the major divisions of

1. Finite Element Modeling,
2. Analytical Modeling, and
3. Atomistic Modeling.

2.1 Compression Models

A brief overview of existing compression models is summarized here. Most of the existing compression foam models are found to be 1D or 2D models in FEM (Finite Element Modeling). They try to explain one or two salient features of the

foam experiments with the help of phenomenological physical analogies. A 1D, non-linear, mass-bistable spring chain system is used for modeling open-cell foams. The snapping of the spring system was analogically used to capture the oscillatory signatures in the plateau regime of foam, explaining the energy absorption mechanism [25]. In another work, a series of 1D non-linear springs was used to capture the microstructural re-arrangements in foams with an analogy to snap buckling. It also captured the hysteresis [26]. Under such model assumptions, it was not possible to simulate the striking experimental features such as the unique initial jump in stress and the sloped plateau response, that were left out. Also, these models were meant to capture the collective behavior of stacks of foams, rather than a single foam layer under compression.

A particular type of foams with free-standing network of Carbon nanotubes is of interest here. Carbon nanotube foams subject to large deformations reversibly switch into different morphological patterns [27]. Each shape change corresponds to an abrupt release of energy and a singularity in the stress-strain curve. These transformations, simulated using a realistic many-body potential, are explained by a continuum shell model. With properly chosen parameters, the model provides closer results of nanotube behavior with non-linear instabilities [27]. In the work [28], it is proposed that the effective bending stiffness of single-walled nanotubes should be regarded as an independent material parameter not related to the representative thickness by the classic bending stiffness formula. Based on this concept, the modified formulas for the critical axial strain and the wavelength of axially compressed buckling are found to agree well with known molecular-dynamic simulations.

In a work employing atomistic simulations [29], the generic features associated with the dynamic compaction of metallic nano-foams at very high strain rates was

investigated. A universal feature of the dynamic compaction process is revealed as composed of two distinct regions: a growing crushed region and a leading fluid-type precursor. In another work, the bending free transverse, longitudinal and torsional vibrations of single-walled carbon nanotubes (SWCNTs) were investigated through nonlocal beam model, nonlocal rod model and verified by molecular dynamics (MD) simulations and found to have a good match [30]. The scale fitting parameters were derived from MD simulations. These inherent MD fitting parameters may not be guaranteed to hold for different experimental settings.

Compaction dynamics of metallic nano-foams has been of interest for mechanics modeling community. Three-dimensional nanometer-scale hydrodynamic, non-equilibrium MD simulations of the foam [31], show internal structure of pore collapse as well as provide detailed information on the foam state behind the shock front, and the shock induced chemistry. Interestingly these results matched with the continuum-scale models. This agreement is likely due to the more homogeneous structure of the foam in the MD simulations. All the wide variety of atomistic models are inherently limited to higher strain rates, which would not allow quasi-static loading and analysis. Whereas, the present work concentrates on quasi-static loading of foam-type materials.

There are also foam-constitutive analytical models with a spring-mass-damping system [2]. To summarize, there are models extending from simple usage of Euler's buckling criteria to Zbib's functional relationship, connecting the height of the sample to instability initiating stress [32]. Initial peak stress indicating the instability initiation and sloped plateau are some of the salient features that have not been captured.

A unique feature of this work is the hardening-softening-hardening flow-stress. The physical mechanism behind flow-stress hardening or softening of a material (it is named here as the material hardening response) is unique and subjective to the material and the deformation path. A few such examples are shown here to elaborate on it. In the case of compression of VACNT foam systems, their instability has been suggested to arise due to the competition between the Van der Waals force potential trying to deform, and elastic energy potential trying to restore the microstructure [33], thereby explaining the resilience. In VACNT systems, the relative tube density, tortuosity, and interconnection density are some of the morphological features affecting the hardening response. However, for foams in general, unit cell wall waviness, density, wall thickness, and interconnection density define the morphology [34]. In this model, all of these features are presumed to affect the material hardening response.

A clear distinction is to be noted between the material morphological mapping and capturing the material response. Morphological properties include the set of features mentioned before as the cell wall waviness, etc. However, the material response or property set denoted in this work, includes features such as the hardening response, strength inhomogeneity, plastic compressibility which are expected to arise out of the morphological properties. These material response or property set does not include the properties such as Young's Modulus and such. However, this model tries predicting the material properties such as the yield strength and indentation hardness, for a given material response. The exact relationship between such morphological details and material hardening response is unknown. Hence, no such relation is presumed. No attempt to extract the morphological properties from the mechanical response is made, rather, only the material response is traced back. Though the source of hardening might change

subjectively, if two material morphologies exhibit a similar hardening response, it is reasonable to unify them under a common name of ‘flow-stress hardening characteristic input’.

2.2 Tensile Models

For foams under tension, not many simulations are reported in meso-scale mechanics. Also the experimental results are rarer to find. In one such computational work, FEA (Finite Element Analysis) was carried out using the RVE (Representative Volume Element) construction with hyperelastic strain energy potential [35]. Only the linear tensile response of epoxy polymer foam was captured [35]. In another work [36], the methodology of transfer of relationships derived at the meso-scale to macroscale using a homogenization process was explored. Generally, from the only available tensile experimental report on the small-scale foam setups, foams exhibit a linear elastic regime, followed by non-linear oscillatory stress graph [37]. At the slowest tensile deformation rate studied, a crossover from chain scission or breakage to crazing is observed as the coverage increases, while for very large deformation rates, only chain scission is observed indicating the effect of strain rate under tensile loading. Another work [38], estimates the Young's modulus of isolated nanotubes by measuring, in the transmission electron microscope, the amplitude of their intrinsic thermal vibrations, finding that carbon nanotubes have exceptionally high Young's moduli, in the terapascal (TPa) range.

In another atomistic-scale work [39], the molecular mechanics study of interfacial binding of carbon nanotube/polymer composites was conducted. They used force-field-based molecular mechanics to calculate the binding energies and sliding frictional stresses between the nanotubes and different polymer matrices

and found that the binding energies and frictional forces play only a minor role in determining the strength of the interface, but that the helical polymer conformations are essential. They suggested that the strength of the nanotube/polymer interface may result from the molecular-level entanglement of the nanotube and polymer matrix. Though this work was concentrated on composites, the emphasis on nanotube entanglements contribution to tensile strength is worth mentioning. Scarcity of tensile experimental results of free-standing systems in the meso-scale further motivates this work. Therefore, we move forward trying to predict the possible deformation modes under foam tensile experiments.

2.3 Nanoindentation Models

In the FEA section, a work employing Gurson model for plastic deformation of porous elastic perfectly plastic material could not capture the undulations and the sloped plateau, which are generally observed in experiments of nanoindentation of foams [40]. To give an example in analytical modeling: a statistical representative model was formulated by generating a random array of foam cells. The positions, diameters, and lengths of unit cells were varied in a statistical manner and fed into an elastic beam model, capturing the elastic part of foams [41]. This was more of a structural response, rather than a material effect. Oliver and Pharr extended the model at nanoindentation scales [42] of the Doerner and Nix [43] method, replacing the inaccurate approximation of the cylindrical flat punch by an effective indenter shape. The Oliver and Pharr approach relies on a number of important assumptions, such as the absence of adhesion, of excessive (non-elastic) sink-in, or pile-up and of reversible plasticity. For example, pile-up (the accumulation of material on the side of the indent) will typically lead to an underestimation of the contact area, which can cause hardness to be greatly overestimated.

Flat-tip indentation experiments have been preferred by Y. Lu and D. M. Shinozaki, as they possess a well-defined elastic-to-plastic transition visible in the indentation load displacement curves [44]. They demonstrate that, given the proper definition of the viscosity function, in-built into their model, the experimental flat-tip indentation response can be described close enough, for polymeric materials at meso-scale. In MD simulations, a work modeled the interaction between CNT walls using the LJ potential law, with material parameterized energy density functions. It captures the recoverability and the sloped plateau, but not the initial jump in stress and undulations found in the plateau [45]. The same work also recommends compressibility effects to be supportive in capturing the foam response better, which favors the selection of plastic compressibility in our model.

2.4 Atomistic Linkage Model

Though there is a wide body of literature on MD simulations of CNTs, one particular work was found to motivate the study here, as the hardening function response used in this work under compression resembled the MD results of their work [46]. As emphasized before, a hardening-softening-hardening material response in this work was found capable of capturing some of the salient features of the experimental study on CNT systems. The same hardening-softening-hardening response was observed in a classical MD simulation study under compression in a study by J Wang et. al. [46]. They had also simulated results under tensile loading. Since the other deformation paths such as tensile modes effect on the hardening response was unknown, this work has a special mention here. They used many-body empirical (REBO) hydrocarbon potentials for short range interactions and standard Lennard-Jones (LJ) potential for long-range interactions between atoms. Such potentials are found to be reliably applied for general foams, polymers and CNT systems. They tried to correlate the mechanical

properties (from simple uniaxial tests) with respect to varying tortuosity of coiled carbon nanotubes (CCNTs). The results from the study surprisingly revealed a hardening-softening-hardening response of the SWCNT (Single Walled Carbon Nanotubes) system under uniaxial compression and tension tests. The physical reasoning observed from the simulations for such responses is summarized as follows.

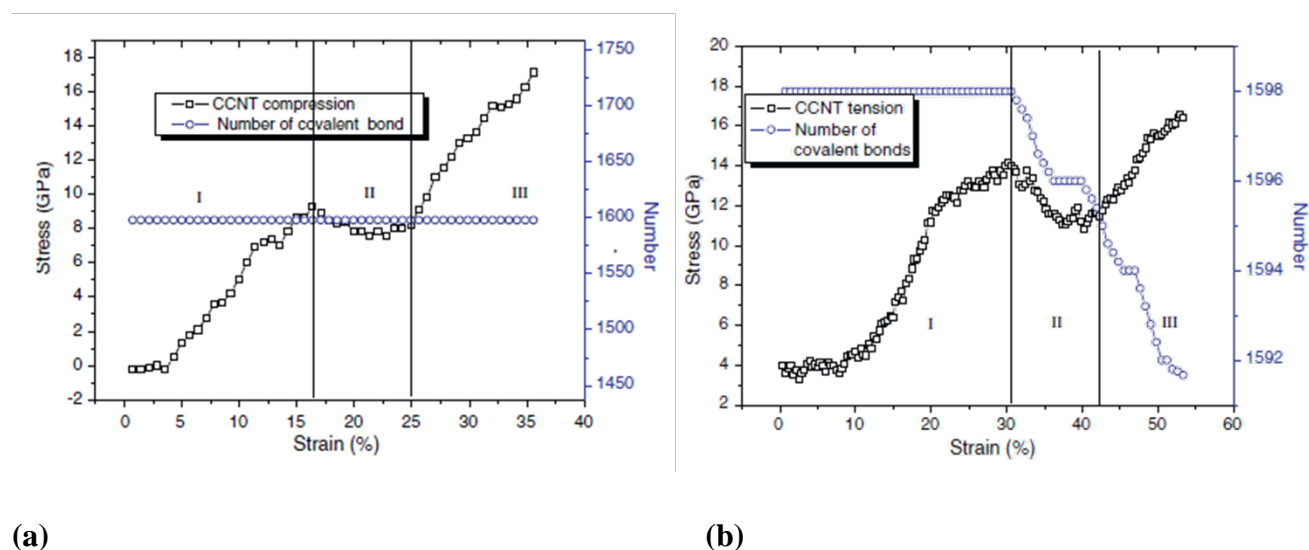


Figure 4: (a) Compression and (b) Tensile responses from Molecular Dynamics simulation of Coiled Carbon Nanotubes (CCNTs) [46].

Under compression (Figure 4(a)), in the first hardening regime, before the first transition strain is reached (first hardening to second softening), the hardening effect is attributed to the compression of the six-carbon rings and the torsion of the C–C bonds. Next, as compression continues beyond this transition point, an increasing number of C–C bonds are aligned perpendicular to the compression axis. This makes the compression stress decrease and hence softening follows. When the second transition strain is reached (second softening to third hardening), the distance between the walls of the CCNT rings become small enough to push against each other, resulting in hardening for the second time. Throughout this

process, the number of covalent bonds is observed to be constant, indicating no bond breakage [46].

In tension results too (Figure 4(b)), the stress-strain response is predicted to have the three regions as before under compression. However, the physical mechanism differs as the physicality of the tension test varies from that of compression. In the first region, the stress increases continually until it reaches a yield-like point, where the maximum stress is reached. Upon further tensile loading, a number of covalent bonds start breaking. The stress drops after this point, leading to a second region of softening. It was noticed that the bonds then start re-arranging themselves favorably to the direction of tensile loading. Hence, as this process starts taking over at the second transition strain, the material again starts hardening [46]. While transitioning from the compression test zone to tensile tests, this result supports retaining the hardening-softening-hardening material setup (explained in Chapter 3).

Here, the physical reasoning behind such a hardening-softening-hardening response differs subjective of the test condition. However, in the case of general foams this also needs to be speculated based on the specific material morphology, which might be derived from other smaller-scale models. From the results, the hardening-softening-hardening trend itself is presumed to hold under tension as well if the presented work is applied for CNT systems. As these MD results were specific to a foam system of CNTs [46], we do not generalize the hardening-softening-hardening response to hold for all foams and all deformation paths. Rather, we take it as the first and primary hardening space to be explored under other tests. We then extend the hardening space by exploring the other types of hardening functions.

Especially for the tensile deformation path, a hardening-softening-hardening function was not motivated for general foam type materials. Still, this mathematical motivation holds in the case of CNTs tensile modeling from [46]. Hence, setups which were completely hardening, hardening-softening were also explored. Similar lack of motivational small-scale models under indentation lead to exploration of different types of hardening functions. Literature reports exist on models able to capture the various instability modes under uniaxial and indentation deformation paths at various scales [47, 48] and such. However, the intention of this work is to formulate a model in terms of material responses such as plastic compressibility, normality, hardening functions and such, which have been reported to be essentially a function of inherent material properties or morphological properties. This would facilitate extracting the material response from the mechanical data and thereby also lead to reasonable speculations of the morphological and material properties.

It is to be noted that the hardening function is a coupled effect of material response and the deformation path, whereas the plastic compressibility, and normality describe the material property exclusively. Material characterization is hard for certain types of foams in the meso-scale and in this work, a mathematically motivated model is suggested to bring such a material characterization a bit closer to reality. The limitations for other models if any, comes from the lack of knowledge of suggestive links connecting the extracted constitutive functions to the material morphology. Whereas, in this work there are some suggestive links borrowed from small-scale models [46], connecting the extracted constitutive functions (material response) and the material morphological fields [46].

Chapter 3

Finite Element Model

3.1 Model Description

As explained in Chapter 1, the model formulation in this work falls within the paradigm of the general theory of viscoplastic models, with specifically designed constitutive function to simulate a foam material setup. This model with hardening-softening-hardening flow-stress function was initially formulated to capture the deformation mechanics of VACNTs under compression [4]. The varied spectrum of deformations and stress-strain behaviors observed [5] proved both the motivation and the validation for this choice of constitutive relation setup.

As shown in Chapter 2, the existing models for simulating foam behavior may not be equipped with certain necessary material responses as a function of the physicality of deformation path and material morphology. Hence, an attempt is made to include the possible material response features in this model. The elastic-viscoplastic model setup was chosen as a model closer to that of foams. Unique flow-stress function, with hardening-softening-hardening slopes, was formulated specifically for the set of polymeric foams based on a phenomenological physical reasoning, which was further motivated by the results of [49], showing the progression of plastic instability. It was initially written as a 2D axisymmetric code, and later it was expanded into a half-space 3D code for indentation to include 3D effects. Under such a model assumption which sets symmetrical boundary conditions, it is hard to capture any asymmetrical deformation modes.

The setup is also strain-rate dependent and allows plastic compressibility. Plastic non-normality is included into the model setup to account for the frictional and other dissipative effects in compliant systems, as in [50]. The unique combination of plastic non-normality and material rate dependence induces contradicting forces, favoring and opposing instability propagation, affecting the results non-linearly. Hence, this setup allows greater investigation space of material setups for simulating the relevant foam-type instability propagation. The formulation is explained in detail as follows, with special respect to the mentioned features.

3.2 Model Formulation

The model formulation is explained here within the framework of the initial 2D axisymmetric code. The additional features for the expansion to 3D will be discussed in Chapter 6. The constitutive setup remains the same in both versions. A Lagrangian finite deformation formulation is used, and with axisymmetric pillar finite element calculations are carried out (pillar of cylindrical coordinates r, z, h in the reference configuration with all field quantities independent of h) using the dynamic principle of virtual work. Initial, stress-free configuration of the pillar occupies dimensions as $(0 \leq r \leq R_o; 0 \leq z \leq H_o)$ as shown in Figure 5(a).

The framework of this model is formulated only for the loading phase. Except for a short ramp-up time, a constant velocity W is imposed at $z = H_o$, to ensure quasi-static loading. The surface at $z = 0$ is considered fixed to a substrate. Hence all velocity and displacement components of nodes at the bottom are constrained to be zero, simulating the bottom substrate. The remaining free surface boundary conditions are set to have zero tractions.

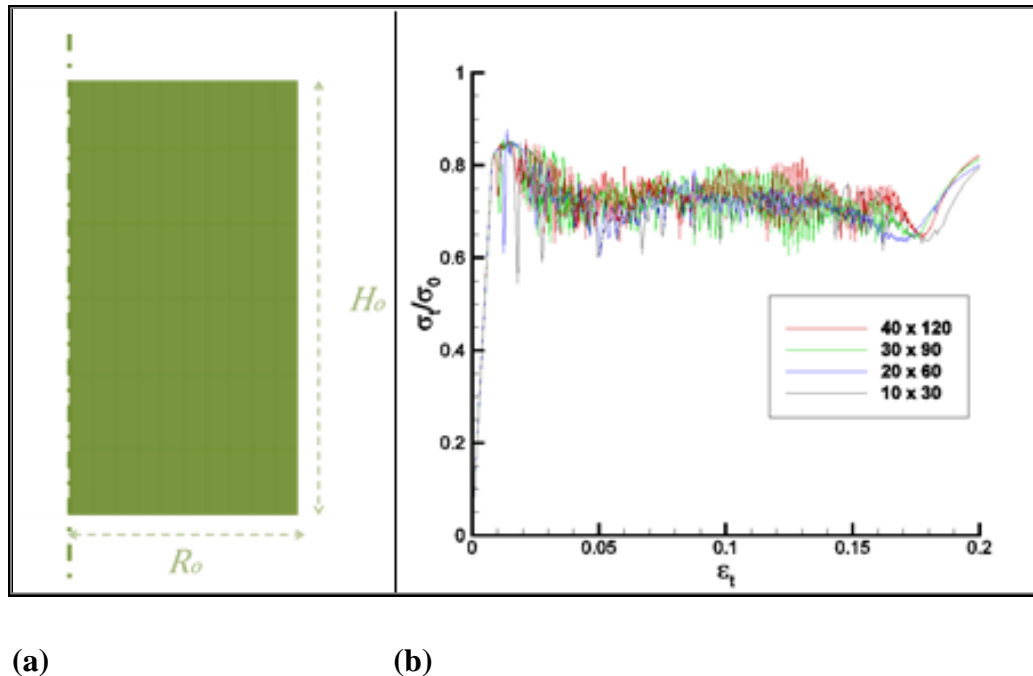


Figure 5: (a) Typical initial undeformed finite element mesh showing the axis of symmetry (in green dot-dash line), the radius, R_o and the total height, H_o , (b) an illustration of mesh induced numerical instabilities.

The finite element mesh is comprised of uniform square elements, each consisting of four crossed triangles. Time integration is carried out by the explicit Newmark β method with a lumped mass matrix as applied in [51]. The finite element discretization is carried out using the convected coordinate system representation of the governing equations with linear displacement crossed triangles as implemented before by Tvergaard and Needleman in [52, 53]. The constitutive update at consecutive strains is carried out via a rate tangent method [53, 54].

3.2.1 Mesh Induced Numerical Effects

A specific example of hardening-softening-hardening setup (material A) under compression is shown in (Figure 5 (b)), to demonstrate the mesh size effects. It is necessary to differentiate numerical instabilities from the true humps in the stress-

strain response. These numerical undulations are affected by the mesh setup, while the true trend of humps is retained on an average. As noted from the stress-strain curves of different mesh sizes, the mesh-induced numerical instabilities increase with smaller mesh element size. As the pillar radius to height ratio is kept at 1:3, mesh density of 1:3 is used to ensure square meshes, with uniform crossed triangles inside. Hence, the set of 40 x 120, 30 x 90, 20 x 60 and 10 x 30 meshes are taken to demonstrate the mesh effects. This is reflected in the curves as the increased number of oscillations. It can also be seen that with a mesh size of 20 x 60, the stress curve averages out the wiggles and starts showing the general trend of the curve. However, there are also false larger stress drops arising here, which were absent in the 40 x 120 and 30 x 90 meshes. This arises from the observation that the buckle amplitude was restricted by mesh size i.e. the amplitude of buckle is allowed to be smaller with smaller element size and visa versa. Therefore with larger mesh size than 30 x 90, buckles get larger thereby leading to larger drops in stress. This larger element size would give rise to only a single buckle, which is not the observed mode of instability in compression experiments of foam systems [5]. With further increase in mesh element size (a coarser mesh), the oscillations die down. Hence, optimizing the mesh size to have minimized numerical oscillations, while maintaining the multiple-buckle formation ability was a trade-off, concluding with 30 x 90 mesh.

This mesh was chosen pertinent only to compression deformation path, but retained for consistency in tensile simulations too. In contrast to compression, in tensile simulations, the numerical undulations were higher for a coarser mesh. Tensile computations had numerical artifacts also arising from mesh alignment issues, affecting the stress-strain response (see Chapter 5) which was overcome by reorienting the mesh accordingly.

Indentation simulations took longer computational time than uniaxial test simulations, running in half-space and hence the choice of mesh was a trade-off between computational time and accuracy of results. Finer uniform mesh (16 x 16 x 16) was employed in the vicinity of the indenter tip and the surrounding mesh (26 x 26 x 26) was coarsened out with a gradient in element size. Nevertheless, a mesh capable of converging results was employed. In this work, both the uniaxial test model (2D axisymmetric model) and the indentation models (3D half space model) had symmetries assumed, allowing only symmetric modes of deformation and instabilities to arise. Hence, asymmetric modes of instabilities are not explored in here.

The finite element formulation is based on the dynamic principle of virtual work, which can be written as

$$\int_V \boldsymbol{\tau} : \delta \mathbf{d} \partial V = \int_S \mathbf{T} \cdot \delta \dot{\mathbf{u}} \partial S - \int_V \rho \ddot{\mathbf{u}} \delta \mathbf{u} \partial V, \quad (4)$$

where V and S are, respectively, the volume and surface of the body in the initial configuration, \mathbf{T} , is the traction vector, and \mathbf{u} , is the displacement vector.

The constitutive relation is that of a compressible elastic-viscoplastic solid, formulated in terms of the Kirchhoff stress $\boldsymbol{\tau} = J\boldsymbol{\sigma}$, where J is the determinant of the deformation gradient and $\boldsymbol{\sigma}$ is the Cauchy (or true) stress. There is no fundamental physical reason for choosing to phrase the constitutive relation in terms of Jaumann rate of Kirchhoff stress rather than in Cauchy stress, except for the advantage of objectivity. The rate of deformation tensor is taken to be the sum of elastic \mathbf{d}^e and plastic \mathbf{d}^p parts.

The total rate of deformation tensor is decomposed into the elastic and plastic parts. Elastic strains are assumed to be small and are given by the following:

$$d_{ij}^e = L_{ijkl}^{-1} \hat{\tau}_{kl} = \frac{1+\nu}{E} \hat{\tau}_{ij} - \frac{\nu}{E} \text{tr}(\hat{\boldsymbol{\tau}}) \delta_{ij} \quad (5)$$

and the plastic flow rule is taken to be

$$d_{ij}^p = 3\dot{\varepsilon}_p p_{ij} / 2 \sigma_e \quad (6)$$

where,

L – Moduli tensor for isotropic solid,

$\hat{\boldsymbol{\tau}}$ - Jaumann rate of Kirchoff stress tensor,

\mathbf{p} – Deviatoric Kirchoff Plastic stress tensor given by $\mathbf{p} = \boldsymbol{\tau} - \beta_p \text{tr}(\boldsymbol{\tau})\mathbf{I}$,

$\dot{\varepsilon}_p$ – Plastic strain rate,

σ_e – Effective equivalent stress corresponding to the instantaneous $\dot{\varepsilon}_p$.

The equivalent stress is formulated as

$$\sigma_e^2 = 3\tau_{ij}q_{ij}/2 \quad (7)$$

where \mathbf{q} is introduced as $\mathbf{q} = \boldsymbol{\tau} - \alpha_p \text{tr}(\boldsymbol{\tau})\mathbf{I}$, to induce plastic non-normality.

When $\alpha_p = \beta_p$, the system reduces to a condition of plastic normality and under

$\alpha_p = \beta_p = 1/3$, it further reduces to the well-known von-Mises isotropic

hardening solid. Also, the $\alpha_p = \beta_p$ condition, corresponds to plastic normality. It

is made sure that the dissipation stays positive as per the laws of thermodynamics.

For that, the dissipation rate calculation was checked as follows:

$$\tau_{ij}d_{p(ij)} = 3\dot{\varepsilon}_p \tau_{ij} p_{ij} / 2 \sigma_e = 3\dot{\varepsilon}_p (\tau_{ij}\tau_{ij} - \beta_p \tau_{kk}^2) / 2 \sigma_e. \quad (8)$$

To have positive dissipation, the term in parenthesis has to be positive, as all other terms remain positive. For the term in parenthesis to be positive, there is a limit on the stress triaxialities followed.

The condition of plastic non-normality is chosen because it has been shown to successfully capture the dissipative, frictional behavior in dilatant solids [55]. For example: in soil mechanics, this non-normality condition has been commonly utilized in modeling, and shown to account for the frictional dissipations. This is similar to the way inter-chain, or inter-cellular friction plays a role governing the deformation in polymers and cellular structures.

3.3 Constitutive Setup & Flow-Stress Function

The plastic response of the rate-dependent hardening viscoplastic solid is given by

$$\dot{\epsilon}_p = \dot{\epsilon}_o (\sigma_e/g)^{1/m} \quad (9)$$

where, m is the rate hardening exponent, and g is the flow stress function, given by

$$g(\epsilon_p)/\sigma_0 = \begin{cases} 1 + h_1 \epsilon_p, & \epsilon_p < \epsilon_1 \\ 1 + h_1 \epsilon_1 + h_2 (\epsilon_p - \epsilon_1), & \epsilon_1 < \epsilon_p < \epsilon_2 \\ 1 + h_1 \epsilon_1 + h_2 (\epsilon_2 - \epsilon_1) + h_3 (\epsilon_p - \epsilon_2), & \epsilon_p > \epsilon_2. \end{cases} \quad (10)$$

The flow-stress function would be better visualized as the relative yield strength property of the material as a function of plastic strain (Figure 6). It allows for tailoring the material hardening/softening characterization over the range of plastic strain as a hardening back stress. The value of ϵ_1 specifies the plastic strain at which the transition from hardening to softening takes place, and ϵ_2 specifies the strain at which the second transition back to hardening occurs. In this work we

explore a wider range of possibilities including, for example, cases where h_2 is positive and other cases, where $h_2 = h_3$, in which case the value of ϵ_2 is irrelevant.

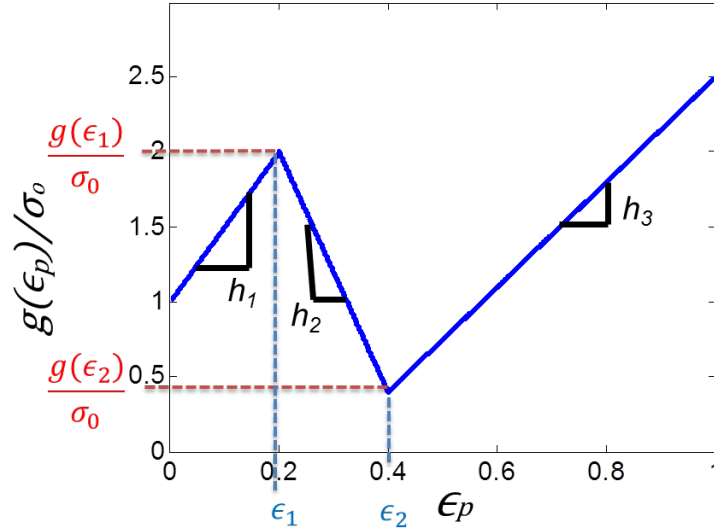


Figure 6: The typical definition of the hardening-softening-hardening flow stress function with the transition strains denoted by ϵ_1 & ϵ_2 and the slopes of the three- piecewise linear functions given by h_1 , h_2 & h_3 , respectively.

Though the motivation to start with a hardening-softening-hardening function was from [49], the phenomenological physical support taken here, for using it in a foam modeling setup, is explained as follows: 1) The first hardening slope is always taken to be positive. A reason for the initial positive hardening slope is to facilitate a smoother continuity from the previously positive sloped elastic regime. In the absence of the initial hardening, the post-elastic structure becomes too compliant and is unable to recover at higher strains. 2) In the course of our model development, it was found that the second softening regime that follows the initial hardening was necessary to initiate a material instability under uniaxial tests. The material instability is affirmed from the corresponding stress-strain signature and the evolution of strain contour. Though, the physical interpretation is not

concretized for general foams, these two hardening-softening regimes are intuitively expected for materials undergoing uniaxial compression and tension. Initial hardening is associated with resistance to loading while the second softening is associated with materials instabilities.

It is hard to draw clear lines on whether the instability propagates only as a material instability or also as a structural instability. However, the initiation as a material instability is found to occur only with the second negative sloped region.

3) The third hardening regime was found to support the structure from collapsing in the course of deformation, through material hardening. This does not imply that a higher degree of hardening would better support the structure; if the transition between regimes II and III is too sharp, it can create shock-hardening. In the case of compression, the material densification occurs after certain limiting plastic strain and hence hardens afterwards. Under tension, a slight densification occurs in the lateral direction and in some cases of foams, this is accompanied by re-arrangement of material links favorable to the tensile loading direction. These expectedly lead to third hardening regime. These are intuitive explanations for the choice of the hardening-softening-hardening function primarily. Also, mesh distortions were noticed to be higher in a hardening-softening setup as the material continues yielding at lower stress levels. Therefore, the third hardening regime was also included.

During the course of model development, this function was explored and found to simulate reasonably well, capturing the physical modes of deformation found under experimentation. The detailed parameter space used for exploration will be explained in parallel in further sections, as each test mode required different settings. While formulating the hardening function, it was noted that the hardening function needs to be always positive to satisfy the second law of

thermodynamics. It is to be noted that the thermal considerations are highly important. However, as the essence of instabilities considered here lies in its mechanical aspects, it was not taken into account. This work focused only on the mechanics of quasi-static instability propagations under conditions in which thermal effects were not needed to be explicitly considered.

As we formulate the tests under quasi-static loading, dimensionless parameters would be sufficient to characterize the test. Hence, density needs to be specified and is taken to be $\rho = 10^{-4} \sigma_o / (\dot{\epsilon}_{ref} H)^2$ in non-dimensional form. For a quasi-static response, the values of parameters such as Young's modulus E , reference stress σ_o , pillar length H , and radius R do not separately affect the response. The response depends on the values of appropriate ratios, and since the focus here is on quasi-static response, these ratios are reported. The fixed parameters (and parameter ratios) are $E/\sigma_o = 100$, $\alpha_p = 0.2$, $\beta_p = 0.28$, $m=0.02$, and the pillar aspect ratio was fixed at $H_o/R_o=3$. The values of these variables are fixed as such during the course of model development, found to capture the foam response better.

However, dynamic, rather than quasi-static, response also comes into the picture because, even though the response is generally quasi-static at lower loading rates, dynamic snapping can occur due to the up-down-up shape of flow-stress function, as seen in Figure 6. Hence, dynamic finite element calculations are carried out for the instabilities that are expected to occur and for ease of convergence of numerical schemes. In some cases, the post instability response can be difficult to calculate quasistatically.

Initially, the system of VACNTs was taken as an example of foam-type material to be modeled. Hence, experiments on VACNTs were used as the first

validation check. It proved to capture most of the salient features observed [4, 5], compared to other models in Chapter 2 such as, the following:

1) The oscillatory plateau region within the stress-strain curve, where each undulation corresponded to the formation and propagation of individual instabilities [4, 5]. This submitted work further explained the detailed mechanism of the sequential buckle propagation. (Compression results are extended in this work, in Chapter 4.)

2) It also captured the initial peak corresponding to the first buckle propagation created by the elastic-viscoplastic transition and

3) The densification, following the plateau region.

3.4 Morphological Link

Experiments on a sample variety grown under different or similar control conditions have shown different trends of compression instability initiation and propagation. The relationship between the mechanical properties as yield-like, plateau stress, and the physical morphological attributes such as the local density variations of the material remains unknown as explained in Chapter 2. No such relationships are needed, while modeling, as it does not intend to trace back the morphological attributes. However, to relate the experimental results to the model results, a relationship between an experimentally available morphological data and a material function input in the model is needed. Though no such exact relations are known or presumed here, it has been hypothesized that a local density variation over the height of the pillar causes the humps in the plateau stress under compression [5]. Therefore, quantifying the local variations in density along sample heights, using image analysis techniques was speculated as useful in predicting their compressive strengths as a function of deformation.

Extension of the model towards mechanical stresses and strain predictions from the microstructural morphological details such as density is attempted. This requires determining the relationship between the relative density and a mechanical property, which corresponds to the input strength gradient, in the finite element model. For example, the $E \sim \rho^2$ relationship holding for open cell foams [2], may not hold for free standing foam-types, whose complex hierarchical makeup, as well as friction, provoke a unique stress-strain response. It is reasonable to expect that the stiffness or modulus would depend on the number of inter-tubular/inter-cellular/inter-chain junctions in the network, as well as on the number density of the unit cells, load-bearing members, and their individual mechanical properties. The dependence of Young's modulus on a morphology-governed figure of merit, (density in this case), was determined by Astrom et al. [56]. They applied a modified semi-theoretical version of the Cox shear-lag model to foam mats and fibers. The statistical number of network contacts was taken into account, which can be altered by chemical or irradiation-induced cross-linking during the growth of sample. They reported that the effective modulus of a foam mat was linearly related to the average number of intersections. The number of fiber crossings increased with the greater number of fibers [57] and hence with the density, although this effect was not necessarily linear. This suggests that, to a first approximation, the stiffness of foams may be linearly related to their density, $E \sim \rho$. Such a linear correlation was experimentally verified by Bradford et al. [58] on foam arrays with varied densities and then measured compressive stresses as a function of compressive strain. Unloading elastic moduli as a function of density inferred from data reported in [58] shows a nearly linear E vs ρ dependence. There is a lack of any other conclusive experimental reports on the subject [59, 60]. In addition to the lack of reports, this only available line of reasoning suggests the

first speculation to be that the relationship between stiffness and relative density in polymeric foams is linear.

Hence, this relative variation in density might be correlated linearly with a gradient in a yield-like mechanical property gradient. Such a variation in the vertical property was input into the model, which revealed its direct effect on the location of the incipient folding, as well as on the slope in the stress-strain plateau of the model results [61, 62]. Axial gradients in E and σ_0 are incorporated into the material and the mechanical property gradient was represented by a strength multiplier, SM , which is the scaling multiplier ratio. This gives the spatial variations of E (Young's modulus) and σ_0 , where $SM = E/E_{bottom}$ and similarly for σ_0 . For example, $SM = 1$, corresponds to the case in which there is no gradient with z (height of the pillar). The height of each finite element is evaluated at the center for which the rescaled E and σ_0 values are being calculated. The strength gradient's importance is shown in its definition of the point of weakness and hence the start of localization of deformation. This over-ride the structurally weak center of the pillar (in the axisymmetric pillar code) under every simple mechanical test considered here. The point of deformation initiation affects the deformation mode and propagation as well.

This strength gradient input into the model is capable of predicting the position of instability initiation, its propagation, and the qualitative stress-strain data, all of which points to its capability to capture some of the key characteristics of the compressive deformation of foams. The strength gradient was also shown to be capable of explaining the slope of the plateau under the setting of a generic viscoplastic model.

3.5 Basis of Output Analysis

The computational results were analyzed in terms of (1) the true stress normalized by the reference stress vs. true strain, (2) the corresponding displacement contours of the outer edge of the sample, and (3) the plastic strain rate contour plots, all as functions of the deformation strain. The true stress was calculated as

$$\sigma_t = \frac{P}{\pi(R + u_r(R, H, t))^2} \quad (11)$$

where P is the normal compressive force computed from the quasi-static principle of virtual work, and u_r is the radial displacement of the cylinder as a function of its radius R , height H , and the time step t . This true stress was normalized by the reference yield stress σ_0 . The true strain was computed by

$$\varepsilon_t = -\ln(1 + \varepsilon_n) \quad (12)$$

with ε_n representing the nominal strain ($\varepsilon_n = \Delta H/H$), where ΔH is the top displacement, normalized by the initial height. The cumulative plastic strain contour plots are helpful in visualizing the deformation mechanism as an evolution of strain.

A physically speculative model, connecting the material property details into an isotropic macrostructure was hence developed. The initial success in capturing the deformation under compression compels one to further test the laws and intuitions of this continuum model at the length-scale of ten orders of magnitude smaller. This is tested under the four simple mechanical tests discussed before. The simplest of all tests is the uniaxial compression test. Therefore, it is the first test to be explored in the following chapter.

Chapter 4

Compression Test

4.1 Introduction

Uniaxial compressions enable straightforward analysis in terms of engineering stress and strain with a large collection of experimental reports in literature [5, 13, 17]. Hence, it was the first of the tests to be explored. Several questions directly followed the compression work [4] and this chapter attempts to answer them [61-63]. We explore the model to understand the relationship between material and mechanical responses under compression. Foam structures were considered as a motivation for this compression analyses as well.

4.2 Model Results vs. Experiments

Uniaxial compression experiments were carried out by post-doc S. Pathak and an undergraduate student, Elizabeth Decolvenaere, on a particular type of foam systems [62, 63], the free-standing network of Carbon Nanotubes.

4.2.1 Experimental Analysis

The experiments reported here were performed by post-doc S. Pathak, while the analysis of experimental results was carried out by post-doc S. Pathak and myself. Compression experiments were performed on two sets of VACNT micro-pillars. Both were grown by the same chemical vapor deposition (CVD) synthesis on the same Si substrate but located on different regions of the substrate (Figure 7). All of these tests were performed under the same experimental boundary condition

of a free-standing network, constrained at the bottom by the substrate and held free at the top. One set of VACNT foam micropillars was located close to the substrate edge. These samples are referred to as “pillars on substrate edge.” The second set was located in the substrate interior, referred to as “pillars on substrate interior.” The details and results of the same are published in [63].

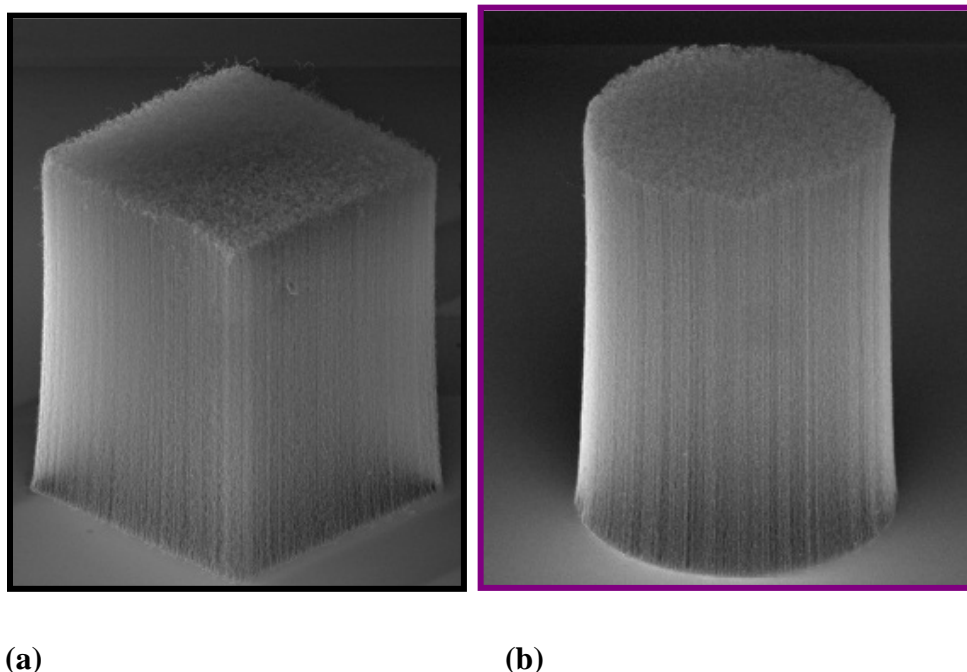


Figure 7(a&b): SEM images of the foam pillars taken at 60 deg tilt angle. (a) Square Pillars on the substrate edge, (b) Circular Pillars on the substrate interior (Reprint under permissions, ACS Nano.) [62].

Representative compressive mechanical response of each pillar type is shown in Figure 8. The results of the complete sample set space are given in Appendix B, showing the statistical consistency of the results. Stress-strain data for both pillar types exhibited three distinct regimes: (1) linear elastic loading, followed by (2) an oscillatory plateau extending to the strains of $\sim 80\%$, and (3) densification, characterized by a steep stress increase upon further compression. The post-elastic

stress plateau for both sets of pillars contained undulations, each of which corresponded to the consecutive buckling-like folding events.

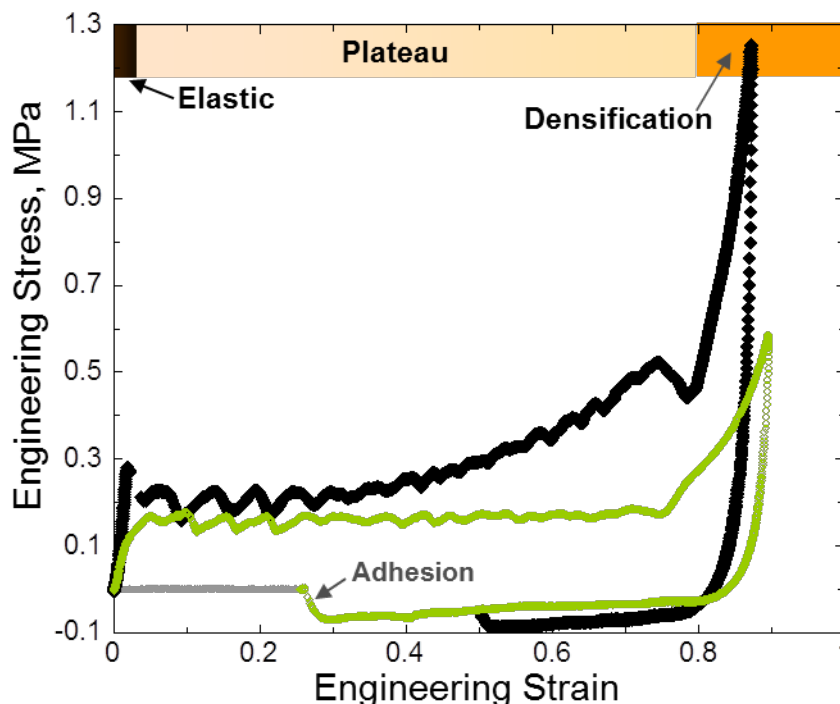


Figure 8: Comparison of the stress-strain responses of two VACNT pillar systems grown on the same substrate. While the square pillars in (a) show a heavily sloped plateau region, the same for the circular pillars shown in (b) is almost flat (as in foams) (Reprint under permissions, ACS Nano.)[62].

Several key differences between the two VACNT pillar types are apparent. Samples on substrate-interior had a nearly flat plateau (slope ~ 0.02 MPa) up to a strain of 75% (Figure 8). The stress plateau in the pillars on substrate edge had two separate slopes: a relatively flat section up to 30% strain, and a steeper region, with the slope of 0.65 MPa up to unloading at 75% strain. These differences in the stress plateaus between the two pillar types correlate with the stiffness change calculated from the initial unloading slope in stress-strain data.

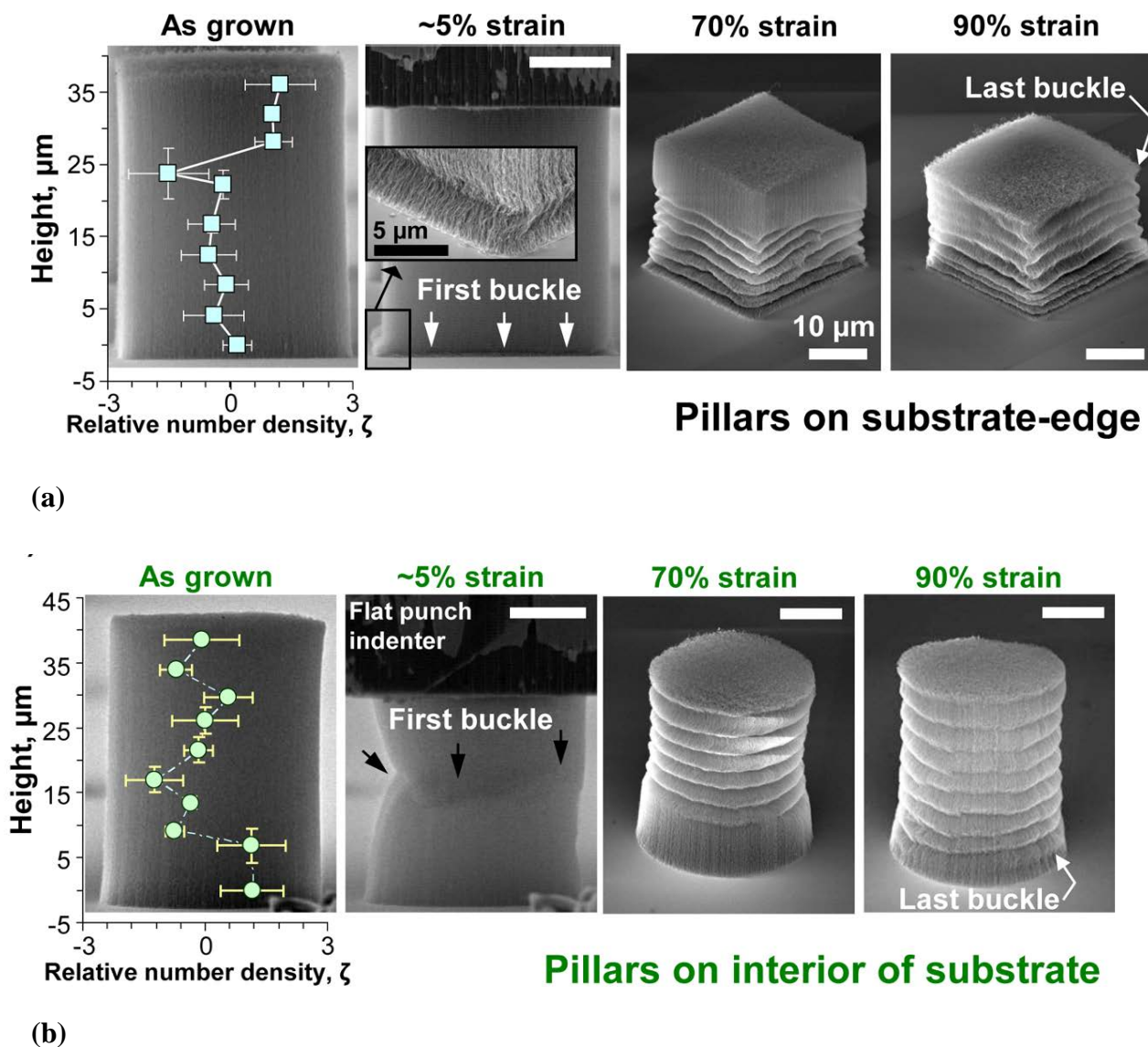


Figure 9: Evolution of deformation under compression shown as a series of SEM images at consecutive strains, for the two different material setups (a) pillars on the substrate edge, (b) pillars on the substrate interior (Reprint under permissions, ACS Nano.)[62].

The unloading stiffness for pillars on substrate-interior remained virtually constant when unloaded from within the stress plateau region ($E = 2.7 \text{ MPa}$). The stiffness of the pillars on substrate-edge increased from $E \approx 20 \text{ MPa}$ to $E \approx 31 \text{ MPa}$ as the strain increased beyond 30%. In general, pillars on substrate-edge appeared stiffer than pillars on substrate-interior. The two pillar sets also differed in the amount of

recovery when unloaded from the post-densification regime: pillars on substrate-interior showed an almost 45% higher recovery than those on substrate-edge. In situ uniaxial compression experiments on the two sets of VACNT samples conveyed that the sequence in the localized folds formation was unique for each sample type (Figure 9). In (8a), the pillars located on substrate-edge have a higher relative density ζ towards the top $\sim 10 \mu\text{m}$ of the pillar, and hence, expectedly buckles in this region of the pillar are the last to form.

Although two distinct pillar cross-sectional shapes (square and circular) are shown in Figure 7 (a&b), these different shapes do not appear to have any major influence on the mechanical behavior of the VACNTs (see Appendix B). Rather the relative location of the VACNTs on the Si substrate was found to play a key role in their resulting morphologies. Further details on the two material sample space and image analysis are found in Appendix B. They explain the reliability of the noted statistical effect in experiments.

Evolution of buckling enables the understanding of the mechanical deformation better. Buckling in these pillars follows a bottom-to-top sequence, as shown by the SEM images. Thus, the first buckle always forms at the bottom (indicated by white arrows), while the top half of the pillar is still undamaged when the sample is unloaded from a strain of $\varepsilon \sim 0.7$. The top buckles (in the region with the highest ζ values) are the last to form. On the other hand, in (b) the highest values of ζ are at the bottom $\sim 10 \mu\text{m}$ of the pillars located in the interior of the substrate. Thus, while the first buckle forms at the center for these pillars, where the ζ value is low (indicated by the black arrows), the buckles at the bottom are the last ones to form at higher strain levels ($\varepsilon \sim 0.9$), i.e., in the densification regime. At lower strains ($\varepsilon \sim 0.7$), the bottom section of these pillars are still free of buckles. The first buckling-like instability, which corresponded to the transition

from elastic loading to plateau in the stress-strain data, are always formed at the bottom of the sample in the pillars on substrate-edge. After initiation, the fold propagated laterally until it fully spanned the pillar width. Bottom to-top buckling occurred in succession, with each subsequent buckle initiating only after the completion of the previous one, below it. Unloading from a maximum compression of $\sim 70\%$ strain left the top third of the pillar relatively undeformed (Figure 9, third panel from left), and the buckle closest to the top always formed last (Figure 9, right-most panel). In contrast, SEM images of the post-compression substrate-interior pillars, unloaded from the same maximum strain of 70%, showed that it was the bottom third of the pillar that remained relatively undeformed (Figure 9b, third panel from left). The first instability in pillars on substrate- interior always formed somewhere at their mid-height (Figure 9b, second panel from left), and the buckle closest to the substrate always formed last (Figure 9b right-most panel). Unfortunately, the entire in situ deformation of pillars on substrate-interior could not be continuously visualized because of their central position on the substrate preventing unobstructed observation of their compression.

4.2.2 Deriving Relative Density: Image Analysis

Quantifying absolute density while concurrently capturing local fluctuations in the density of VACNTs is challenging because these samples are too complex for the typical image-based quantification methods [64, 65]. To overcome these difficulties, evaluation of the relative changes in the local VACNT density as a function of height was chosen rather than attempting to compute the absolute densities. Edge detection technique employing the Canny algorithm was used to systematically calculate the average relative number density, ρ , of tubes in each SEM image. Image analysis revealed that the two types of pillars exhibited opposite trends in relative density (Figure 9a&b). Pillars on substrate-edge had the

highest ρ in the top 10 μm , and their density profiles resembled a step function, where $\rho \approx 1$ for all locations above the height of $\sim 23 \mu\text{m}$, and $\rho = 0$ at all locales below. Maximum ρ in pillars on the substrate interior was located in the bottom $\sim 10 \mu\text{m}$, close to the substrate, and any changes in density within this region did not exceed the measurement error. Image analysis also revealed that the apparent density decreased in the midsection of all samples: at $\sim 23.7 \mu\text{m}$ in 36 μm tall pillars on substrate-edge and at $\sim 16.3 \mu\text{m}$ in 40 μm tall samples on substrate-interior.

Quantifying relative density differences between the two sample sets is useful in understanding their deformation mechanisms, and the knowledge of the relative density profiles can be used to predict the location of the initial buckling instability in a foam matrix. It is reasonable to expect the first folding/buckling event during compressions of foams to originate close to the substrate because of its rigid constraint. Hence, this mapping is shown in Figure 9(a & b), first panels, along with the error bars, showing the consistency of the trend. Pillars located on substrate-edge corroborated this notion (Figure 9a). In contrast, the incipient instability in pillars on sample-interior occurred somewhere in the middle of pillar height, at the locales with the lowest relative foam density. It appears that the lower relative density triumphs the constraining effects of the substrate in driving the location of the buckling instability in these sample-interior pillars. The last buckles in both sets of pillars occurred in the regions with the highest relative foam densities: near the top in the substrate-edge samples and at the base in the substrate-interior ones. Two significant limitations associated with the calculation are noted as follows, 1) it cannot differentiate between the edges of individual foams and foam bundles, and 2) possible differences in tortuosity of the foams are also unaccounted in here. So no comparison between two individual pillars might be made with just the local relative density profiles found here.

4.2.3 Compression Model Results

Examining the stress vs. strain response generated by the FE model, (whose formulation was introduced in Chapter 3) against the experimental results was the first validation analysis attempted. All of these calculations had defined set of hardening parameters as $h_1 = 5.0$, $h_2 = -1.5$, $h_3 = 1.5$, $\varepsilon_1 = 0.005$ and $\varepsilon_2 = 0.1$.

Using an equivalent linear variation in SM (strength multiplier, introduced in Chapter 3) for the corresponding variation in the relative CNT number density over the height, the simulation results were generated. It was assumed that the same linear spatial variation holds for the modulus, E , and for reference flow strength σ_0 . Four distinct cases were explored: case 1, SM is constant throughout the pillar height; case 2, SM increases linearly with pillar height; case 3, SM decreases linearly with pillar height; and case 4, SM has a step-increase at the midpoint of the pillar height, that is, at $z/H = 0.5$, where z is the coordinate along the pillar height. The absolute coefficient in the linear relation between density and mechanical property will affect the linearly varying SM cases (Figure 10) but is not critical when SM variation is a step function.

These plots revealed a direct linear relationship between the global hardening slope, θ , of the stress plateau and strength multiplier range ΔSM ($\Delta SM = |SM_{top} - SM_{bottom}| = 20\%$) (Figure 10). Comparing cases 2 and 3 revealed that a forward or reverse gradient in SM of the same magnitude led to the similar hardening plateau slope in the normalized stress-strain curve.

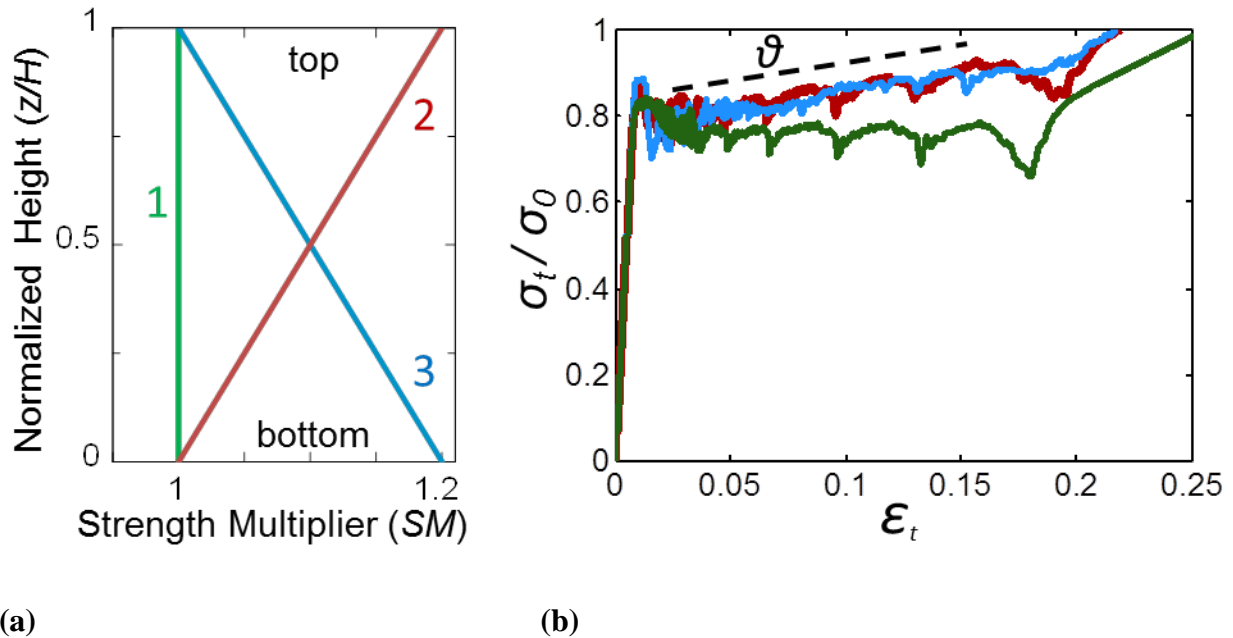


Figure 10: (a) Three variations of the SM function used in simulations and (b) their corresponding output stress-strain responses, reflecting a suggested reason for a sloped plateau phenomena to be the material inhomogeneity over the height of the pillar (Reprint under permissions, ACS Nano.)[62].

This lack of sensitivity to the direction in the gradient is likely due to the identical fixed boundary conditions in the axial direction (but not necessarily in the radial direction) at both ends of the sample in the model. When gradients of opposite signs are prescribed, the deformation would commence in the direction of weaker-to-stronger part of the pillar, that is, in the opposing directions. No distinction between stress-strain outputs would be expected because in both cases the stress is governed by the high-strain-rate front overcoming the progressively harder regions, regardless of their position within the pillar. Under such comparisons, it was apparent that the structural effects dominate this compression test. It could only predict the presence of strength gradient, but could not rather distinguish the direction.

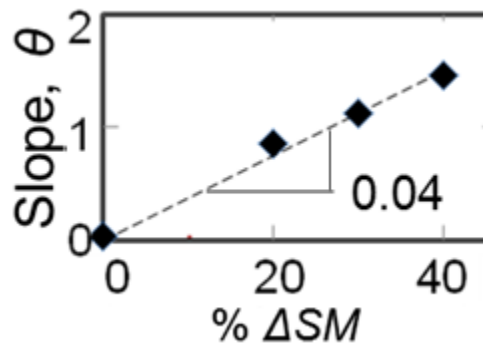


Figure 11: Plot of the hardening slope of the plateau regime vs. % ΔSM over the height of the pillar, showing a linear relationship. (Reprint under permissions, ACS Nano.)[62].

After quantifying the linear dependence of plateau slope on the strength gradient, the material equivalents of the two different sets of pillars are taken into the simulations. For the square pillars on the substrate edge, case 4 (Figure 12(a), case in black), is taken as the equivalent and for the circular pillars on the substrate interior, case 1 (Figure 12(a), case in green), is taken as the equivalent. For case 4 (Figure 12(a), case in black), where SM is represented as a step function along the sample height and matches the square pillars on substrate edge configuration most closely, a single value of slope was insufficient to characterize the stress-strain data. Two distinct slopes, θ_1 and θ_2 , correlated with the relatively porous (weaker) bottom part and the more densely populated (stiffer) top segment. The normalized stress-strain curve for case 4 (Figure 12(b), black curve) closely matched that for case 1 (constant property, no gradient) until ε_A . The second slope, θ_2 , between the strains of ε_A and ε_B , was significantly higher than θ_1 due to the abrupt shift to higher strengths in the middle of the pillar. The hardening slope in case 1, uniquely defined by a single value of θ , was lower compared to the two linearly varying cases (cases 2 and 3), which suggests a linear relation between output slope θ and input property variation, ΔSM . In all cases, the slope(s) of the stress-strain output generated by the FE model qualitatively reflected the shape of the input yield-like

property gradient. It is reasonable that this linear correlation can provide a quantifiable link between the measurable microstructural property i.e., density, and macroscopic mechanical response, i.e., stress, as a function of strain,

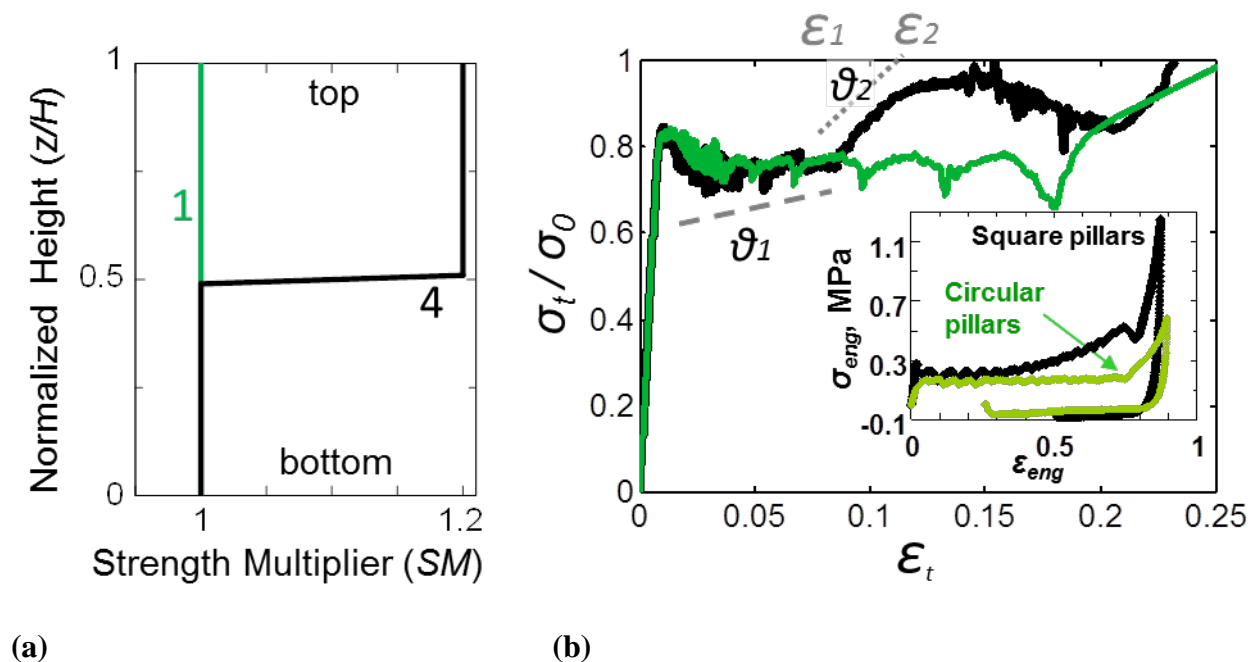


Figure 12: Comparison of case 1 (green curve, representing circular pillar) vs. case 4 (step variation in SM , representing square pillar) and their corresponding stress-strain responses with an inset of the experimental curves. (Reprint under permissions, ACS Nano.)[62].

Table 1 provides a matrix of input and output parameters for each studied case. Additional output figures of merit were amplitude, a , and wavelength, λ , of the outer surface displacement undulations or buckles, whose definitions are schematically shown in Figure 13. Table 1 demonstrates a close-to-50% drop in the amplitude of oscillations in case 3 (negative property gradient) compared to case 1 (no gradient). This is likely due to the substrate-like structural hindrance from the fixed radial displacement boundary condition at the bottom. As the instability progresses from the top toward the bottom of the sample, radial displacements are restricted, thus lowering the buckle amplitude.

<i>Case Number</i>	<i>Slope</i>	<i>Transition Strain</i>	<i>Buckle Amplitude (a/R)</i>	<i>Buckle Wavelength (λ/R)</i>
1	$\theta = 0.037$	$\varepsilon = 0.155$	0.022	0.092
2	$\theta = 0.862$	$\varepsilon = 0.155$	0.022	0.094
3	$\theta = 0.853$	$\varepsilon = 0.17$	0.014	0.086
4	$\theta_1 = 0.025,$ $\theta_2 = 3.6$	$\varepsilon_A = 0.089,$ $\varepsilon_B = 0.126$	0.013	0.043

Table 1: Comparison of the deformation characteristics measured for the four variations of the SM functions used.

The buckle wavelength remained unaffected because the axial boundary conditions at the top and bottom were similar among the cases. The presence of a step-shaped barrier in strength in case 4 reduces the effective length of the pillar to half of its real length, allowing only the lower half to undergo sequential folding, while the upper half has a single instability. In this case, both the amplitude and the wavelength of the outer surface displacements were lower than in all other cases. Assuming a linear correlation between the local density and yield-like strength at the same location, strength variations in the simulated cases 1 and 4 represent reasonable approximations to the density distributions gleaned from the uninformed image analysis for the two sets of pillars. Both experimental and simulated stress vs. strain relationships reflect the attributes of these input material strength variations.

The effect of a high-strain-rate front within the individual folding events was also evaluated. The folding instability appears to occur in two consecutive phases: initiation and propagation. The initiation of these instabilities is uniquely defined

by and is sensitive to the direction of the density gradient: the first fold/buckling-like instability always nucleated at the weakest point over the height.

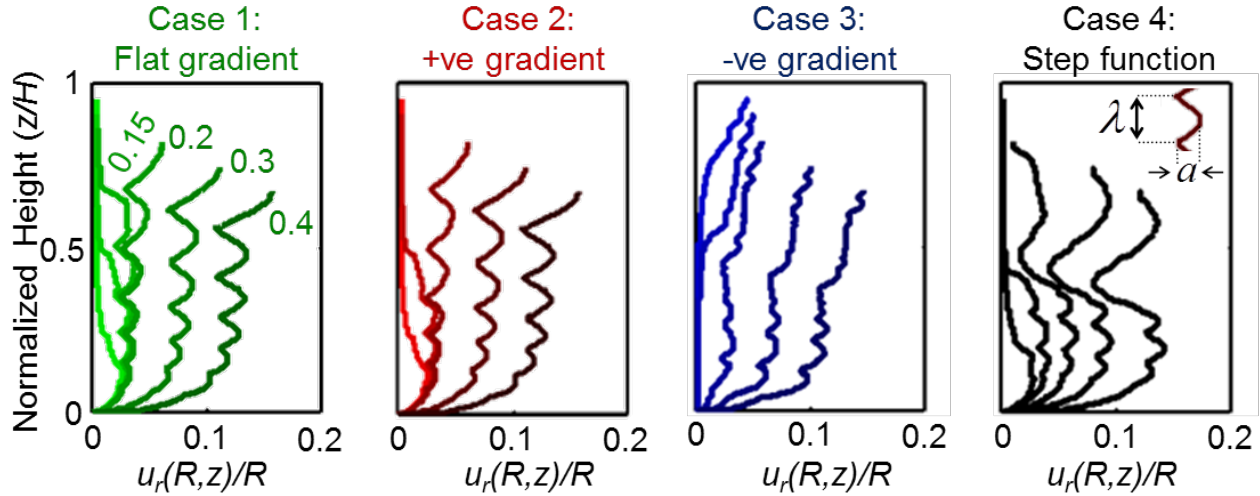


Figure 13: Simulation results showing the evolution of the outer deformation profiles corresponding to the four different *SM* functions shown before. The deformation profiles are shown at progressive strains of 5, 10, 20, 30 and 40%.

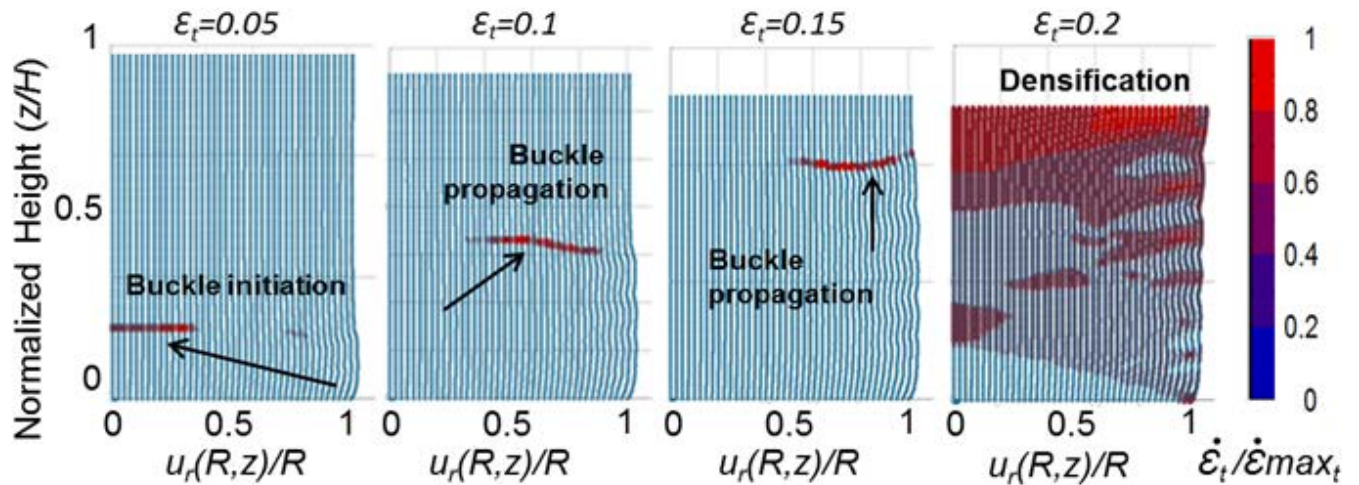


Figure 14: Strain rate contour plots for case 1 at four consecutive strains, showing the observed phenomena of the sequential buckling evolution.

This holds true in both the experiment (Figure 8) and the simulations (Figure 12). For case 2, where *SM* function is lowest at the bottom of the pillar, the first buckle

occurred at the pillar base, while the reverse holds true for case 3, which had the lowest SM value at the top of the sample. Case 4 in the simulations differed from all others because the sequential buckling propagated only in the relatively weaker bottom half of the pillar. The hardening slope θ_l from the initial loading to ε_A for case 4 (step function) was virtually equivalent to that for case 1 (uniform property), which implies that the high-strain-rate front had not yet reached the strength barrier at that point (see Table 1). Figure 11 shows the outer surface displacements for each of the studied cases at four progressively higher applied strains. Figure 12 shows the strain rate contour plots within the buckling phases for the no-gradient case (case 1).

These computational results revealed that in case 1 (no gradient) the first fold initiated at the bottom with a localized increase in strain rate, which initiated at the onset of the first buckling instability (Figure 13) and propagated laterally to the right while concurrently progressing toward the top. At each strain, only the part of pillar below the strain-rate front buckled, which led to the sequential formation of folds as the wave propagated through the structure. When the front reached the top of the pillar, the plastic strain in the entire sample shifted the response into the densification phase. This was indicated by the increased strain rate in the entire sample (Figure 13) and the steep increase in the normalized stress at strains greater than $\varepsilon_t = 0.2$ (Figure 12).

The combination of micro-compression experiments on VACNT cylinders, edge detection analysis of their images, and mechanical modeling revealed that the commencement of local failure events and compressive stress-strain responses were uniquely linked to relative density gradients. From the results under compression simulations, it was evident that the response was a combination of structural response interferences and the material response, to a lesser extent.

Hence, in the search for better tests to extract material properties, the next simplest test, the uniaxial tensile test results are discussed in the following chapter.

Chapter 5

Tension Test

5.1 Introduction

One of the key findings from compression tests is that the response in compression is the interplay of both structural and material responses, i.e., the observed overall compressive stress-strain relation does not directly reflect the intrinsic material properties. Extraction of material properties from the overall stress-strain response under compression is also complex and not unique [66]. The next natural simple test we would like to explore is uniaxial tension which might predict more about the intrinsic material property, either alone or in combination of the compression results. Tensile strength is an important mechanical parameter, but its nature is completely different from the strength in compression. Usually it involves bond reorganization in the atomic level. Hence, strength, and particularly tensile strength of a solid material, similar to that of elastic constants, must ultimately depend on the strength of its interatomic forces/bonds. However, this relationship is far less direct than in the case of elastic materials, and it is greatly affected by the intrinsic material morphology.

There are experimental results in macro-scale foams under tension: for example, tensile deformation of composites of foams [67] or that of ropes of compliant materials [68], or that of single CNTs [69]. However, they are not reflective of the meso-scale foam deformation. Particularly few experimental reports are available for foams, under meso- or nano-scale tensile results, likely

due to the complexities associated with conducting such experiments. Hence, modeling it would be an obvious first step to understand the tensile deformation dynamics, and this hardening-softening-hardening model has been taken up with the promising link of [46], as explained in Chapter 2.

Here we do not attempt to quantitatively capture the response of foams themselves, under uniaxial tension. Rather, we focus on assessing the relation between material parameters characterizing the hardening-softening-hardening hardness function in the constitutive formulation and the mechanical response. This, of course, presumes that the constitutive framework used in the calculations is appropriate for characterizing the foam tensile mechanical response

5.2 1D Model Analysis

It is known that for an elastic solid the states ahead and behind the neck transition can be obtained simply from the jump conditions governing continuity of mass, momentum and energy. Unlike the elastic solids, for any inelastic solid a full three-dimensional analysis must be performed to obtain the same information. Here, we first use a one-dimensional analysis to set the stage and then carry out finite deformation axisymmetric 2D finite element calculations using the constitutive framework under tensile loading. A simple one-dimensional model gives insight into the possible non-uniform deformation modes that can be expected under uniaxial tension for the type of constitutive relation used here. There is a significant body of literature on using one dimensional analysis to gain insight into tensile instabilities [70-73] on general elastic or plastic setups. The presentation here follows that in [74]. The possible non-uniform deformation modes predicted for materials of such viscoplastic setting considered are: (i) diffuse necking, (ii) localized deformation, and (iii) a propagating neck. Consider a

one-dimensional bar of initial length H_0 and cross-sectional area A_0 subject to a uniaxial force P . At the current stage of deformation the length of the bar is H , and its cross-sectional area is A . Equilibrium requires that P is uniform along the length of the bar. The force P can be written as

$$P = A_0 s = A \sigma, \quad (13)$$

where s is the nominal stress and σ is the true (or Cauchy) stress. We also define the Kirchhoff stress τ as

$$\tau = J \sigma = F s, \quad (14)$$

where $J = V/V_0 = HA/H_0A_0$ (V and V_0 are the deformed and undeformed reference volumes, respectively) and $F = H/H_0$. The maximum force is reached when $\dot{P} = 0$. From the expression of P , given in eq. (5), the condition is written down as,

$$A_0 \dot{s} = \dot{A} \sigma + A \dot{\sigma} = 0. \quad (15)$$

Detailed derivations of strain rate and current effective Poisson's ratio and such terms can be found in [75]. The main idea of this derivation was for rate independent response, $\tau = g(\varepsilon)$, so we end up solving for,

$$\dot{\varepsilon} [dg/d\varepsilon - \tau] = 0. \quad (16)$$

When derived in this way, the maximum load condition for a compressible solid has the same form as the Considère [70] condition for an incompressible solid. Within this one-dimensional context, attainment of a force maximum (or, equivalently, a maximum nominal stress) is regarded as a criterion for the onset of diffuse necking in a tensile specimen.

Next, consider the possible emergence of a localized band from a homogeneous deformation state. Continuing equilibrium requires that $[\dot{P}] = 0$ where $[\]$ denotes a jump. Under detailed derivation, as in [75], it is shown that in this one-dimensional context the conditions for the onset of diffuse necking and of deformation localization coincide. In a three dimensional model and for rate independent response, the localization condition involves a bifurcation under all displacement boundary conditions. The one-dimensional analog of this can be regarded as $\dot{A} = 0$ throughout the deformation history. Also, it is worth noting that $\dot{\sigma}$ can become negative even if τ is monotonically increasing.

The last type of instability is a propagating deformation band, which arises in a variety of contexts and with a variety of underlying physical mechanisms. By writing out the balance of linear momentum, energy, and the compatibility conditions, as in [75], it is seen that for a sufficiently slow propagating front, inertia plays a negligible role. Hence the nominal stress on each side of the propagating neck is equal. For a hardening-softening-hardening relation, A and B denote points on the two hardening branches, ϕ_A is the area under the maximum, and ϕ_B is the area above the minimum as in Figure 15.

A similar analysis is found in [76]. The cylindrical samples considered here are constrained at the substrate (bottom), so the initial deformation is not uniform. The material is rate dependent, so the simple expressions for rate- independent material response do not apply. The effect of the three-dimensional pillar geometry (axisymmetric in the analyses here) and material rate dependence can differ for the three potential instability modes.

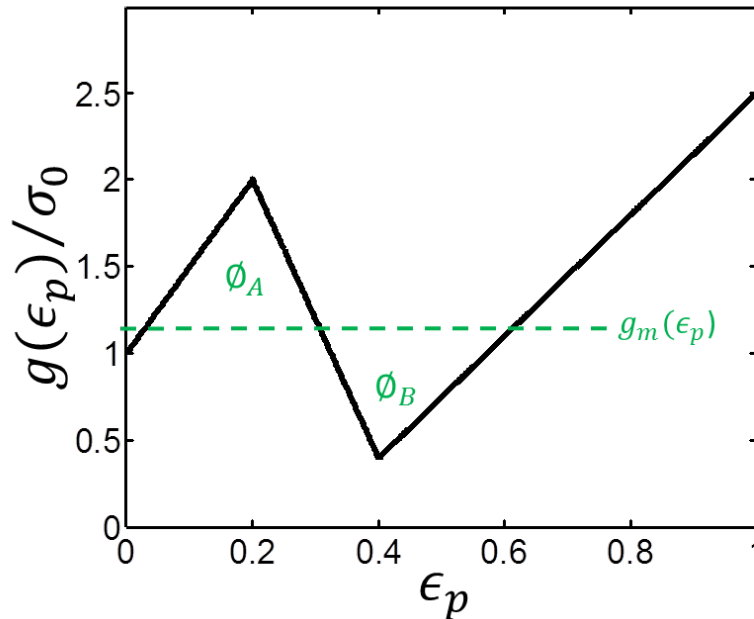


Figure 15: Plot of flow stress function with the Maxwell equivalent flow stress and the area equivalence terms shown.

The finite aspect ratio of the pillars is expected to delay the onset of diffuse necking to strains beyond that of attaining a maximum nominal stress [77]. The material rate dependence delays the onset of both the diffuse and the localized necking [29, 33].

The main focus of the simulations here is to quantify the dependence of the mechanical response of the pillars on several parameters (such as h_2 , h_3) that characterize the material function in Eq. 8 (see Chapter 3). The pillar geometry, the constraint-induced deformation inhomogeneity, and material rate dependence can all play a role in determining the instability mode and the post-instability response. The relation between the overall stress-strain response of the pillars and the material property set is of particular interest. Its importance is in showing the extent to which a uniaxial tension test can be used to determine material properties.

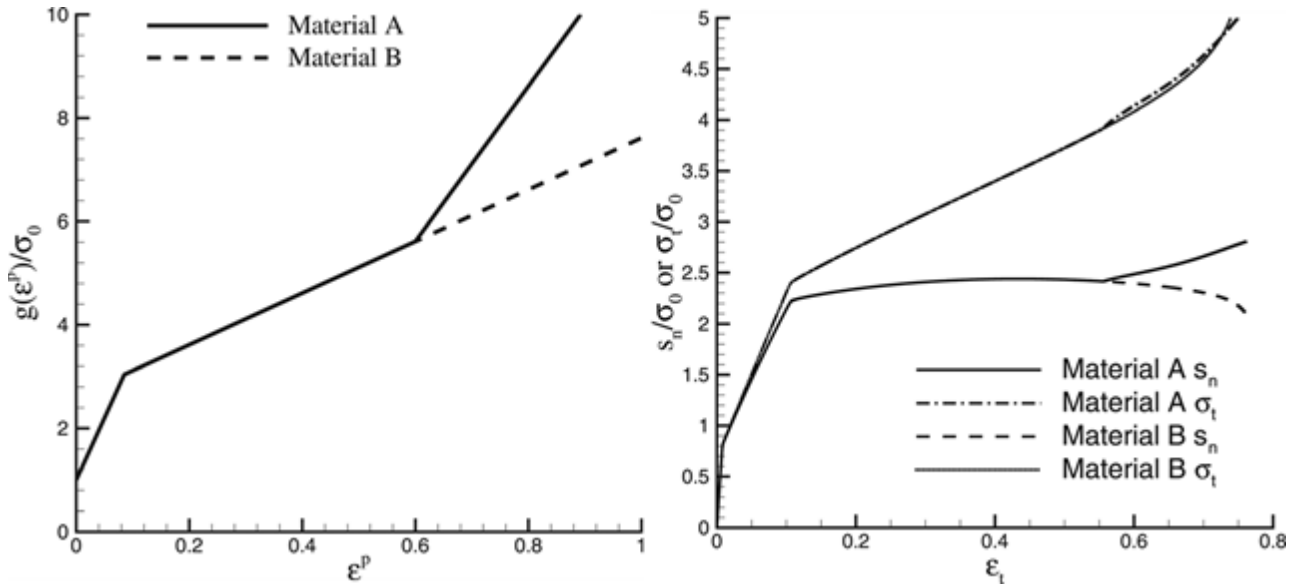
5.3 Instability Analysis

Unless specified otherwise, the parameters h_1 and ε_1 are fixed at 24 and 0.085, and the only parameters varied in the calculations are h_2 , h_3 , and ε_2 . There was no specific reason to fix h_1 at a higher value compared to the cases of compression, except that, under tension, a higher initial stiffening was needed for enough distinction among instabilities.

5.3.1 Diffuse Necking Instability

It was discovered that, under this model setup, in one case of uniaxial tension, the necking initiates at the peak stress in the global stress-strain response. It is to be remembered that the results are for any material exhibiting viscoplastic constitutive relationship. Several experimental data can be shown to demonstrate this well-known phenomenon [76]. This necking observation is consistent with the experimental observations of elongation via necking in some polymers and in many metals [78], though the modeling did not aim to simulate these materials. All calculations of diffuse and localized necking modes used a 30 x 90 quadrilateral mesh, which gives a uniform mesh of square elements in the reference configuration.

Here two cases are taken. Figure 16(a), shows the hardness functions for two materials: material A with $h_2 = 5.0$, $h_3 = 15.0$, and $\varepsilon_2 = 0.6$ and, for comparison purposes, material B with $h_2 = 5.0$, $h_3 = 5.0$, and $\varepsilon_2 = 0.6$. In terms of the variation of flow stress function with plastic strain, material A exhibits hardening-increased hardening, whereas material B has a constant hardening rate. The computed overall stress-strain curves for materials A and B are shown in Figure 16(b).



(a)

(b)

Figure 16: The hardness function as a function of plastic strain, (a) for material A ($h_2 = 5.0$, $h_3 = 15.0$, and $\epsilon_2 = 0.6$) and for material B ($h_2 = 5.0$, $h_3 = 5.0$, and $\epsilon_2 = 0.6$) and (b) their output stress-strain response.

The curves of σ_t vs. ϵ_t (true stress and true strain) are nearly identical for materials A and B. Also, the values of the nominal stress s_n are essentially identical for both materials up to $\epsilon_t = 0.55$ with a maximum in s_n occurring at $\epsilon_t = 0.43$. However, for $\epsilon_t > 0.55$, s_n increases for material A and decreases for material B. As a consequence, the evolution of the deformation distributions within the two specimens differs significantly, even if they deviated after significant strain of $\epsilon_t > 0.55$. For both materials A and B the true stress continues to increase strongly over the strain range shown while the nominal stress attains a shallow maximum.

Figure 17(a&b) shows the distribution of normalized plastic strain rate $\dot{\epsilon} = \epsilon_p/(W/H_0)$, where W is the imposed velocity and H_0 the total height of the pillar. The strain of $\epsilon_t = 0.50$ was chosen, as it was at a strain a little higher than the strain at maximum nominal stress.

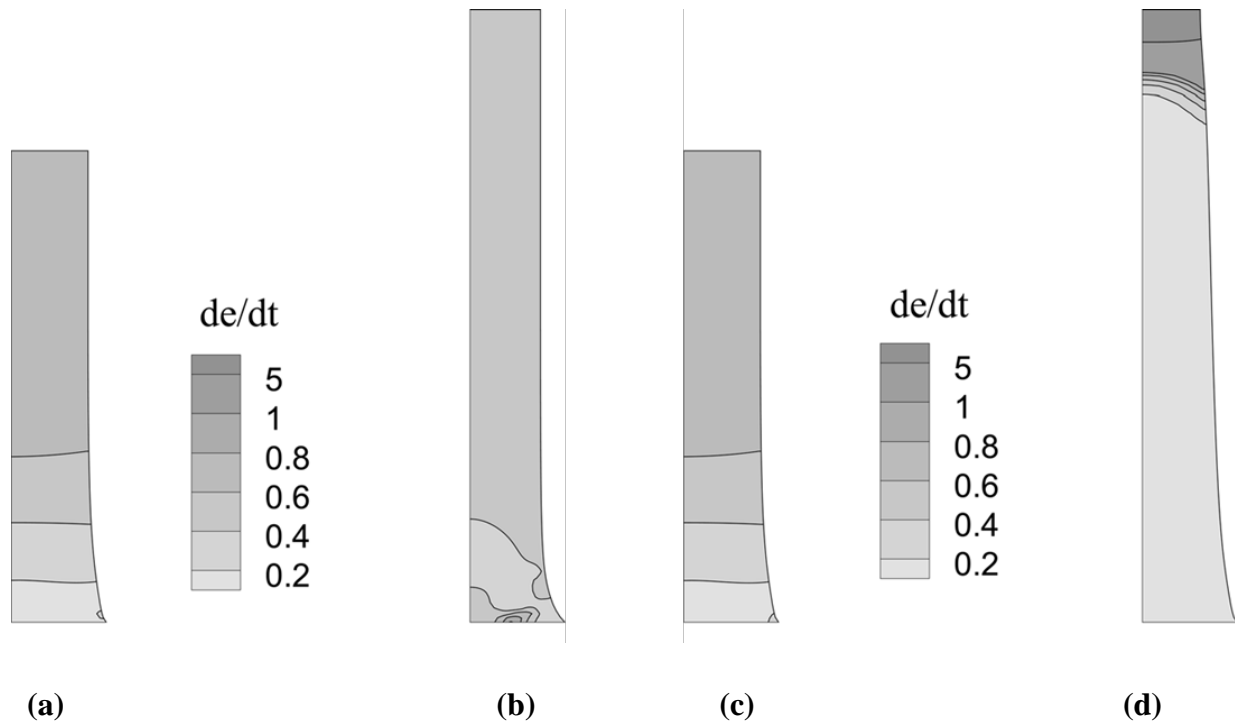


Figure 17: Distributions of normalized plastic strain rate for material A(a& b) and B(c & d): (a) $\varepsilon_t = 0.50$ and (b) $\varepsilon_t = 0.76$.

A very shallow neck forms at the end, $z = H_0$, where the maximum value of $\varepsilon_t = 0.76$. Subsequently, the plastic strain value locally exceeds 0.6 in the incipient neck and the material stiffens there, since $h_3 = 3h_2$. The deformation, and therefore the stiffening, propagates down the bar at the last stage of deformation at around, $\varepsilon_t = 0.76$ shown in Figure 17(b). While most of the bar is uniformly straining with $\dot{\varepsilon} = 0.4$, the substrate constraint at $z = 0$ leads to a strongly inhomogeneous higher strain rate distribution near that end. Distributions of normalized plastic strain rate are shown in Figure 17(c & d) for material B, at the same two values of ε_t as before. The plastic strain rate distribution at $\varepsilon_t = 0.50$ in Figure 17(a) is essentially the same as that for material A. However, without the increased hardening of material A, the diffuse neck continues to develop, as seen in Figure 17(b), where the maximum plastic strain rate $\dot{\varepsilon} = 9.5$ is in the neck. Thus, the additional third hardening acts to suppress diffuse necking. Till this point, we have explored only

the regimes within which diffuse necking happens, and the intensity of diffusion is reasoned out due to the flow stress function.

A diffuse neck forms when the slope of the middle regime h_2 is sufficiently positive for a maximum nominal stress to be attained. When the slope of the middle regime h_2 is increased further, the deformation becomes more uniform. In both cases in Figure 16, the nominal stress (which is directly measured in experiments) can be related to the intrinsic material response if the geometry change due to necking is accounted for.

5.3.2 Localized Necking Instability

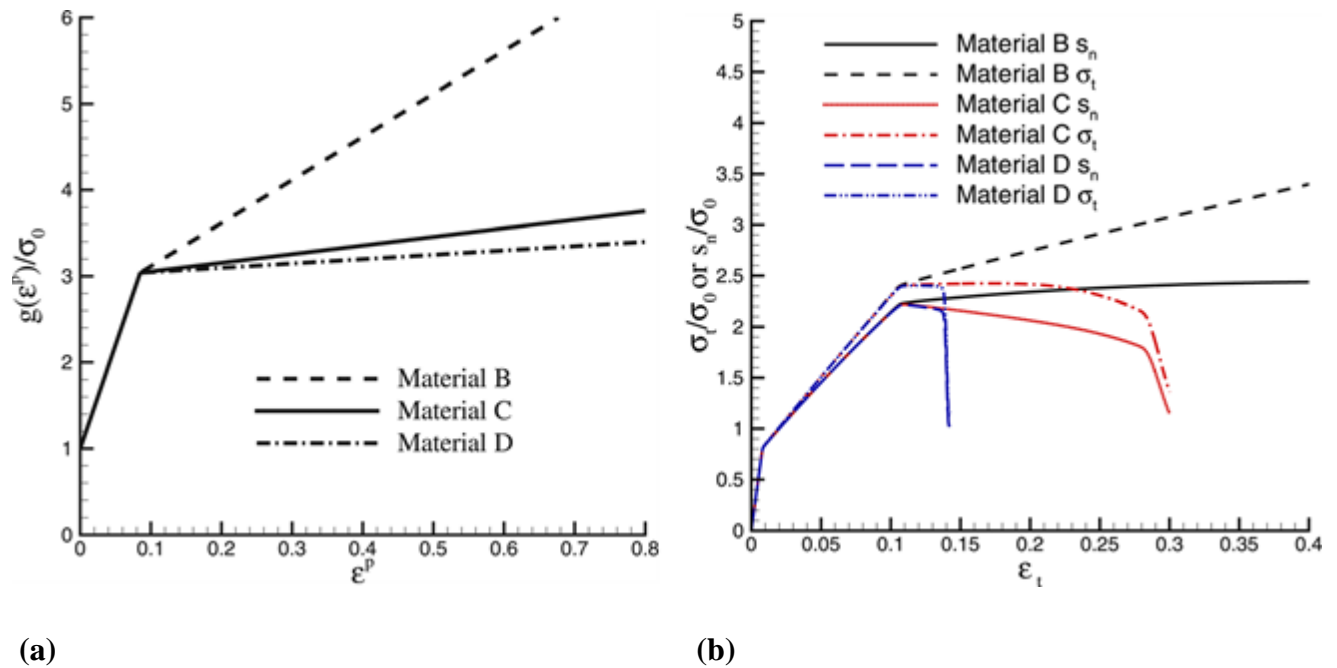


Figure 18: (a) The hardness function for material B ($h_2 = 5.0$, $h_3 = 5.0$, and $\epsilon_2 = 0.6$), material C ($h_3 = h_2 = 1.0$) and material D ($h_3 = h_2 = 0.5$) and (b) their respective output response.

Now transitioning into localization mode, we consider hardening relations for which true stress attains a maximum. Figure 18(a) shows the hardness functions for

material C, $h_3 = h_2 = 1.0$ and material D, $h_3 = h_2 = 0.5$. Material B has also been included for comparison. The overall stress-strain curves for materials B, C, and D are shown in Figure 18(b). For materials C and D the overall true stress σ_t , as well as the overall nominal stress s_n , reaches a maximum. For material C a sharp drop in the stress-strain curves occurs at a relatively small strain, $\varepsilon_t = 0.14$, and the values of σ_t and s_n nearly coincide. For material D, the sharp drop in the overall stress values occurs at a much larger value of ε_t , and there is a clear difference between the values of σ_t and s_n until the sharp drop occurs.

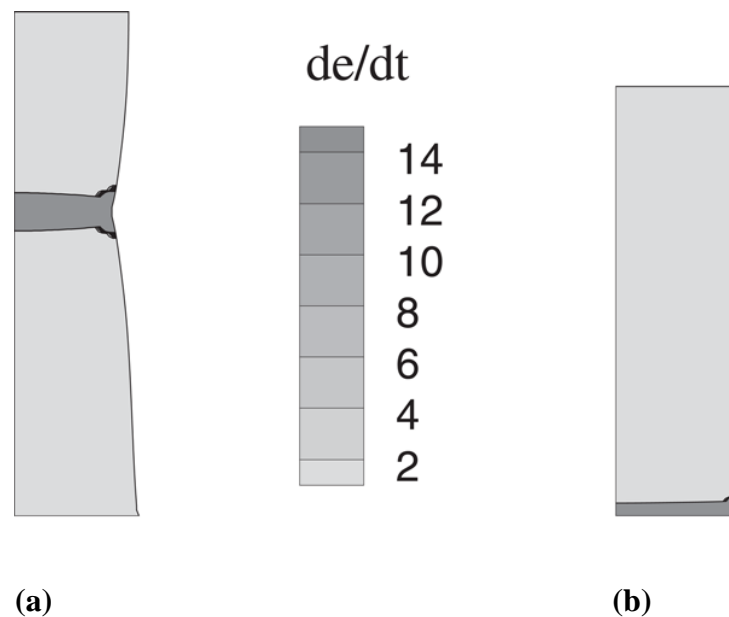


Figure 19: Distributions of normalized plastic strain rate (a) material C at $\varepsilon_t = 0.3$ and (b) material D at $\varepsilon_t = 0.14$.

For material C considerable necking has taken place before the strain rate has localized into a band. Whereas for material D, the strain concentration due to the constraint at $z = 0$ precipitated a localized band before any significant necking has taken place. Although dynamic calculations are carried out, material inertia plays a rather small role in the overall response in the calculations for materials A, B, C, and D. For example, for material D the latter stages of straining are characterized

by the rapidly localized deformations. The major reassuring result, related to the rate dependence feature of the model, is that with plastic normality and rate-independent material response, localization requires strongly negative hardening. Whereas plastic non-normality, as in the constitutive relation here, promotes localization [79]. Rate dependence, as also included in the constitutive relation here, was found to be a stabilizing factor [72]. On the other hand, for slight rate sensitivity the main qualitative features of the rate-independent constitutive response are preserved.

From the simple one-dimensional model relation for linear hardening, the value of the true stress eventually decreases and can become negative at a sufficiently large strain. The possibilities then include the true stress decreasing to essentially zero or the eventual emergence of a localized deformation mode. The degree of rate dependence and the extent of the deviation from normality play essential roles in determining which of these deformation modes occurs. The increased hardening at large strains, as for material A, acts to delay both of these outcomes.

In short, for a sufficiently large negative slope h_2 , the deformations can localize into a narrow band at relatively small strains. The condition for this involves an interplay among the slope of the hardness function, plastic non-normality (destabilizing), and material rate dependence (stabilizing). Nevertheless, when such a localization occurs in uniaxial tension, the strain at which it occurs gives a qualitative indication of the form of the hardening response.

5.3.3 Propagating Band Instability

The calculations for a propagating band used a 40 x 60 quadrilateral mesh for reduction in numerical wiggles. The reason for the choice of this mesh stems from

the observation of Ballarin et al. [80] that mesh-induced oscillations in the overall stress-strain response occur for a propagating band deformation mode. The amplitude of the oscillations depends on the orientation of the mesh boundaries. It was found that the 40 x 60 rectangular mesh setup led to a noticeable reduction in the oscillation amplitude, as compared to a square quadrilateral mesh. In addition, the mesh was also oriented oblique to the direction of band propagation, to reduce numerical artifacts. The band propagation stress correlated directly with the Maxwell flow stress function that was input to the model, as predicted by the 1D simplification.

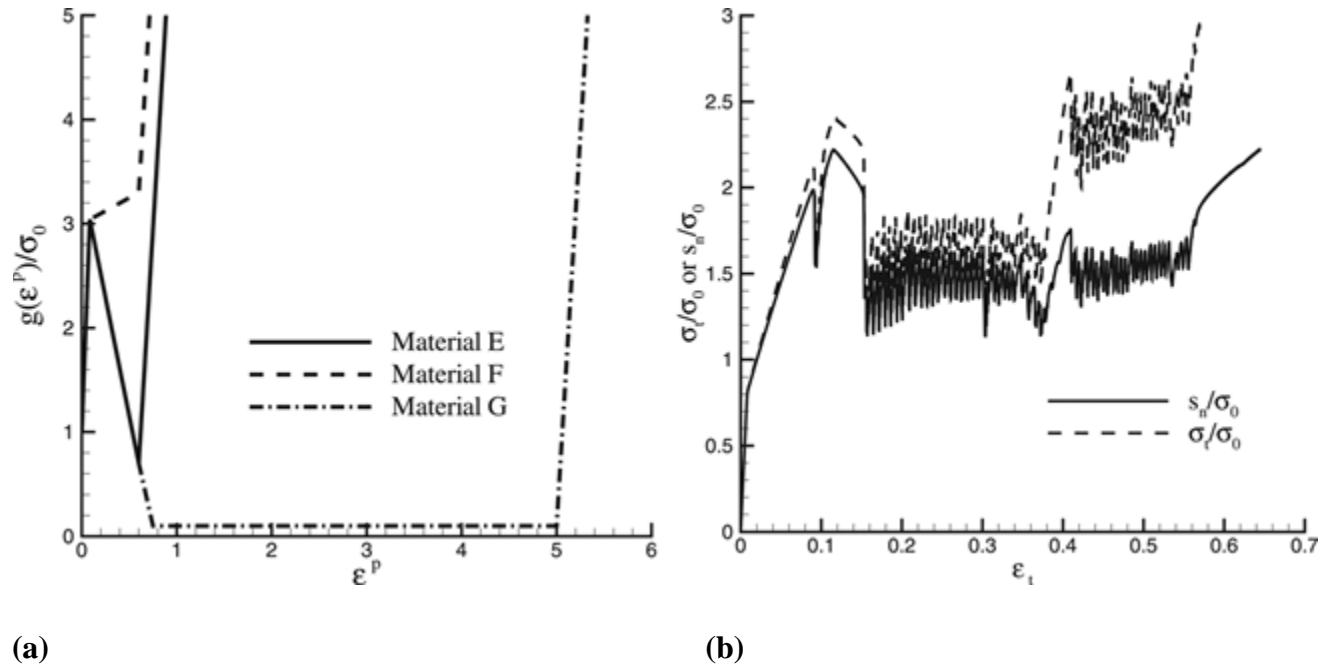


Figure 20: (a) The hardness function for material E ($h_2 = -3.90$, $h_3 = 5.0$, $\epsilon_2 = 0.6$), material F ($h_2 = 0.5$, $h_3 = 15.0$, $\epsilon_2 = 0.6$), material G ($h_2 = -3.90$, $h_3 = 15.0$, $\epsilon_2 = 5.0$), and (b) the output response for Material E.

Figure 20 shows the computed stress-strain response for material E ($h_2 = -3.90$, $h_3 = 5.0$, $\epsilon_2 = 0.6$). There is an initial peak, indicating the initiation of the band followed by oscillations of both σ_t and s_n about a plateau, where it propagates, with

a mean value of about $1.4 \sigma_o$ for s_n and $1.8 \sigma_o$ for σ_t until $\varepsilon_t = 0.37$, at which point there is a much larger increase in σ_t than in s_n . The oscillations continue until $\varepsilon_t = 0.56$ and vanish at higher strains. Equating nominal stress on either ends of the band with $\tau = g$ gives a Maxwell stress of $1.26 \sigma_o$, which is a bit smaller than the mean oscillating value of $s_n = 1.4 \sigma_o$. The oscillations in the overall stress-strain response are associated with the deformation mode being the propagation of a band of increased strain rate.

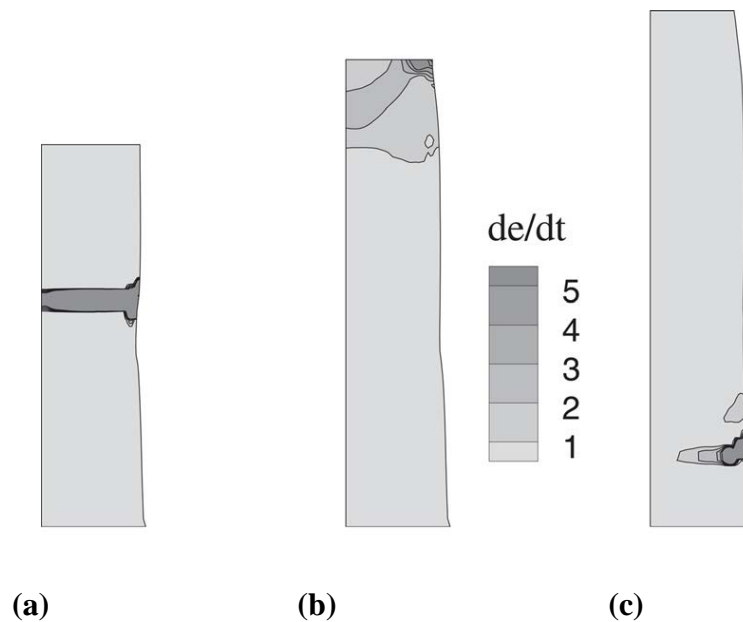


Figure 21: Distributions of normalized plastic strain rate material E (a) at $\varepsilon_t = 0.2$ (b) at $\varepsilon_t = 0.3$ and (c) at $\varepsilon_t = 0.5$.

Figure 21 shows contours of the normalized strain rate $\dot{\varepsilon} = \varepsilon_p / (W/H_0)$ at three values of overall strain. At $\varepsilon_t = 0.2$, the band of high strain rate has propagated about $2/3^{rd}$ the length of the pillar. The strain rate contours at $\varepsilon_t = 0.4$, revealing that the reason for the sharp increase in the value of overall true stress σ_t is mainly due to the decrease in area that occurs when the high-strain-rate band has reached at $z = H_0$. At $\varepsilon_t = 0.5$, the band has propagated down to near the pillar base,

and the magnitude of the strain rate in the band is smaller than in the earlier stage of deformation at $\varepsilon_t = 0.2$. The oscillations in the overall stress-strain curves disappear when the band propagation dies out. The responses for Material F and G give more insight into the material characterization [75]. The three modes of instability captured are explained, and the next sections deal with the material inhomogeneity effects.

To summarize, for a sufficiently large negative slope h_2 , the deformations can localize into a narrow band at relatively small strains. The condition for this involves an inter-play between the slope of the hardness function, plastic non-normality (destabilizing) and material rate dependence (stabilizing). Nevertheless, when such a localization occurs in uniaxial tension, the strain at which it occurs can give at least a qualitative indication of the form of the hardening response. The situation when band propagation occurs is more complex. However, at least within the constitutive framework considered here, band propagation is a direct consequence of the hardening-softening-hardening profile of the hardness function.

5.4 Material Gradient Effects

The effects of property variation were explored under tension tests in the model. Three different cases of SM variation were studied within the propagating band deformation mode (Figure 22(a)). The three cases of strength gradient that were considered are as follows: Case 1): a uniform strength function over the entire height of the pillar, and Cases 2 and 3): linearly increasing and decreasing strengths with height.

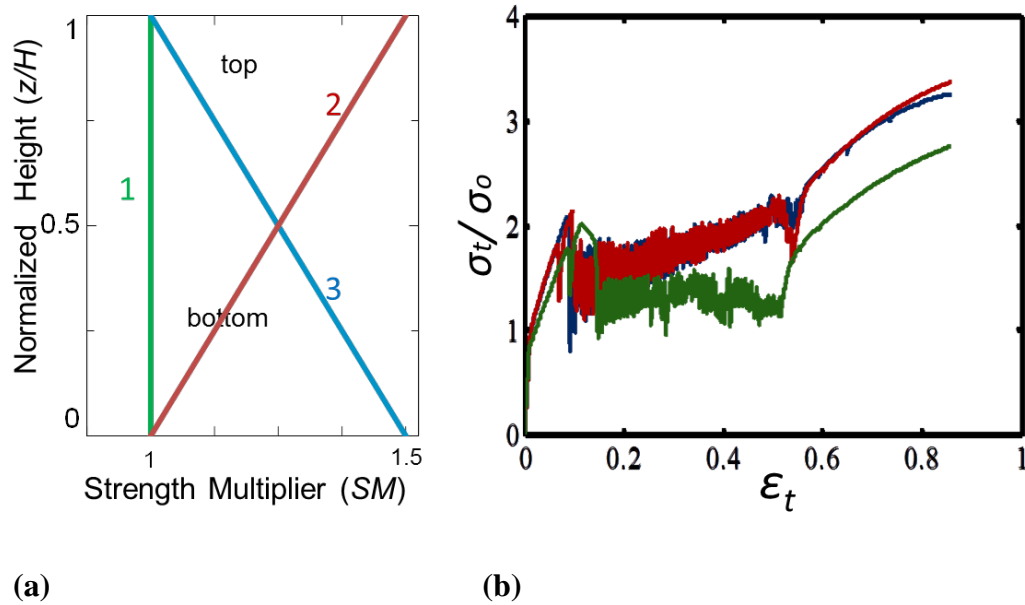


Figure 22: Three Cases:1-3. (a) SM functions input, (b) the respectively normalized stress-strain curves of the three cases plotted.

The output global stress-strain responses demonstrated that the slope(s) of the plateau regions qualitatively mimicked the shape of the input yield-like property gradient for all cases considered (Figure 22(b)). The outer deformation profiles of the pillars indicated that the location of band initiation was consistently observed at the point of lowest strength. After an incipient band was formed at the weakest point, it expanded out into the regions of higher stiffness, which is manifested as the positive slope of the stress plateau. Keying a reverse gradient also shows the same trend of the band initiating at the weakest point. This indicates a similar lack of sensitivity to gradient sign (which is at the top for $-ve$ gradient and the bottom for $+ve$ gradient cases). Again, under tensile tests, only the presence of strength gradient could be predicted, not the direction of gradient, showing the influence of structural effects. Of course, the strain rate contours over evolving strains could help in distinguishing the gradient direction. This cannot be a convincing answer, as our aim here is to extract material functions only from simple mechanical data

such as the stress-strain response. In the case of uniform strength along the sample height (Case 1), the plateau remained flat, as expected. The quantitative results will be summarized in the final chapter.

5.5 Summary of Tensile Results

The three typical modes of deformations can be schematically represented below (Figure 23).

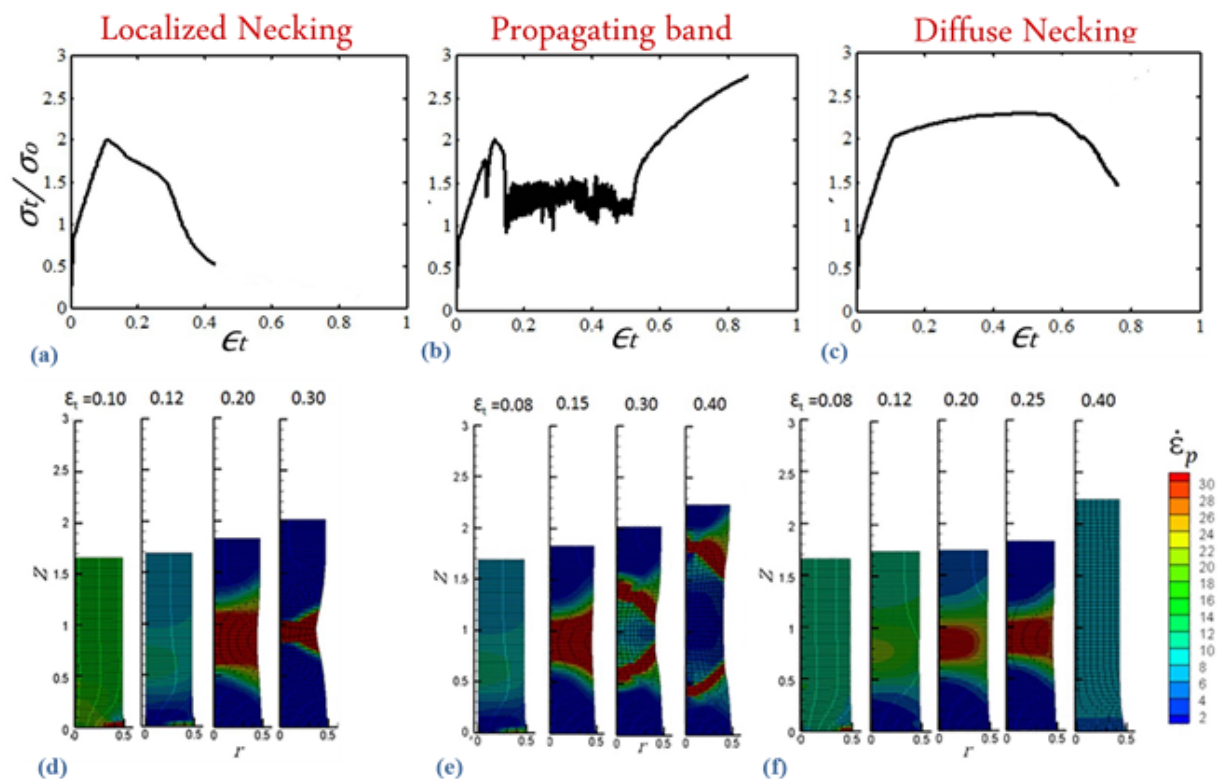


Figure 23: The typical stress-strain response of three modes of tensile deformation shown in the first row (a, b & c). The normalized plastic strain rate contour plots show the three distinct modes of instability in the second row (d, e & f).

The difference in stress-strain response between the compressive and tensile result stems also from the influence of the hydrostatic pressure found to be decreasing in the case of tensile experiments and increasing in the case of

compression experiments. One advantage of the tensile test was that there were distinct rules that the hardening function complied with under each mode of deformation. Therefore, tensile tests give a minimum guarantee to predict the trend or shape of the hardening material function with better accuracy than compression. Hence, it proved to have lesser structural interferences compared to compression. However, it was still not a convincing test and thus the next set of tests was carried on to find their efficiency at capturing only the material property. The 3D indentation simulation was the next preferred simple test in order. This test would have additional 3D effects and free surface effects, possibly influencing the results in reducing the structural interferences.

Chapter 6

Nanoindentation

6.1 Introduction

By the end of the first two uniaxial test result analyses, it was evident that the difference in the physicality of the two tests leads to completely different deformation mechanisms. Therefore, this also leads to different stress-strain responses completely. However, in spite of this difference, the intrinsic material response capturing capabilities of the uniaxial tests were qualitatively similar (e.g., material gradient effects, hardening function to plateau slope correlations). Quantitatively, the sensitivity scales remained in the same order too (summarized in Appendix A, Table 4). It would be worth restating the finding that one of the advantages of tensile results analysis was the existence of distinct hardening parameter relations for each mode of tensile instabilities; for example, localization instability at lower strains corresponded with lower second softening flow stress. Thus, there was a minimum assurance from a tensile test result to predict the trend or profile of the hardening function with better accuracy, which was not the case under compression. To summarize uniaxial tests, the tensile results were found to be a step better than compression in providing predictions of the hardening function (material response). However, it should be taken into account that the tensile response still had structural interferences of lesser degree, i.e., the observed overall tensile stress-strain relation did not directly reflect the intrinsic material properties back. Thus, to include 3D effect, non-uniform stress distribution, and

free surface effects, the next simple and obvious test to cross-compare was indentation. It was subsequently checked for helping in reduction of the structural effects coming into play.

Indentation is a frequently used test to measure the hardness of materials and to derive information on mechanical properties such as the yield strength and the elastic modulus. The hardness test measures the mean contact pressure when an indenter is pressed into the surface of a flat specimen, providing simple means of testing the resistance to plastic deformation. Uniaxial compression involves uniform stress distribution, whereas nanoindentation allows for non-uniform stress and deformation state and free surface effects. Due to these additional effects, the mechanical response of the material under indentation technique is expected to respond differently, and thereby, capture multiple material properties with different sensitivities. In particular, for elastic-plastic materials, there is a simple relation between yield strength and hardness; see, for example, [8]. Extracting the ratio for this particular elastic-viscoplastic constitutive setup here is also covered here. Many reports on indentation end with the hardness measurement, but in this work, we try to investigate this unique deformation mechanism of viscoplastic material setup under indentation. Hence, the correlation between the salient signatures in stress vs. strain response, and the material deformation mechanism, which was captured through a series of cumulative plastic strain contours is also reported here.

As emphasized earlier, it is not attempted to quantitatively model the response of foams themselves, under indentation. Rather, the main focus is on assessing the relation between material parameters characterizing the hardening-softening-hardening flow stress function in the constitutive formulation in [66, 81], and the indentation mechanical response. This response uses figures of merit such as

1. the indentation hardness,
2. other deformation characterizing parameters including the ratio of true to nominal area under punch, and
3. the plastic zone propagation features.

This includes an obvious presumption that the particular constitutive framework used in the calculations is appropriate for characterizing the nanoindentation mechanical response of foams considered.

This nanoindentation modeling was also motivated by the lack of understanding of indentation behavior of foams. Though there are many micro and macro-scale experimental reports on indentation of foam-type materials, few experimental reports on meso-scale indentation exist, e.g., on metallic foam nanoindentation [82]. As a part of this research work, a relevant experimental nanoindentation study on VACNT foams was conducted [61] and the characteristics are described in here. We observed three distinct regimes in their indentation stress–strain curves (Figure 24) under flat-punch nanoindentation:

- 1) a short elastic regime, followed by
- 2) a sudden instability, which resulted in a substantial rapid displacement burst manifested by an instantaneous vertical shearing of the material directly underneath the indenter tip, and
- 3) a positively sloped plateau for higher displacements, as shown in [61].

The qualitative stress-strain signatures stated here hold in general for the type of compliant foams considered here.

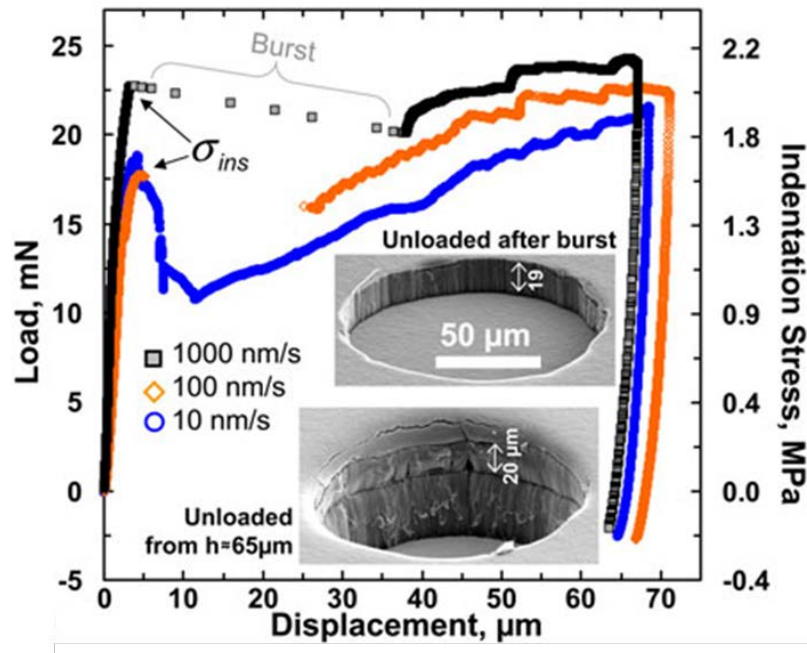


Figure 24: Experimental indentations at different displacement rates showing a large displacement burst and more pronounced buckling signatures at the faster rates for foams. The inset images show the residual impressions of indentation [61].

6.2 3D Model Setup

The aim is to model the quasi-static response of a half-space block ($l \times l \times l$) indented by a rigid indenter. However, for numerical convenience dynamic analyses are carried out, but with the loading rates chosen to minimize inertial effects. In particular, a dynamic finite element formulation is used to avoid forming a large stiffness matrix. The imposed indentation rate is chosen such that inertia effects do not play a significant role. Also, a full three dimensional finite element formulation is used even though for a conical indenter the quasi-static solution exhibits axisymmetry because the aim is to use this code in the future to analyze indentation for other indenter shapes as well. The main focus of this section is the simulation results on three different representative material setups (hardening flow-stress functions), wide enough to cover the broad spectrum of

results, subjected to quasi-static loading of indenters with conical & flat punch tips. Though the test calculations are carried out dynamically for ease of numerical convergence, the loading is preferably kept as quasi-static to avoid inertial effects.

Calculations are carried out for two indenter shapes: (i) a conical indenter with a circular cross section, and (ii) an indenter with a fixed square cross section. A significant difference between these two shapes is that for the conical indenter the contact area increases with indentation depth. However, the contact area is fixed for the indentation with flat punch indenter with the square cross section. In both cases, perfect sticking is assumed as soon as the block comes into contact with the indenter. The results of interest here are for indentation depths significantly larger than the element size but small enough so that the finite block size does not significantly affect the response. The boundary conditions include traction free lateral surfaces and $u_3 = 0$, with zero shear tractions on the remote surface initially parallel to the indented surface.

The constitutive setup of the model remains the same as before [4, 66]. One of the expected physicality differences between the two tests of uniaxial compression and indentation is as follows. Non-uniform stress-state under indentation also arises from the lower hydrostatic stress generated in the proximity of indentation and that increases away from the indenter tip. It is to be noted that the yield stress criterion involves the hydrostatic stress term implicitly in the constitutive formulation.

The output response was quantitatively compared in terms of hardness vs. indentation depth plots and the value of the A/A_{nom} to show the effect of pile-up or sink-in due to indentation near the tip. If the ratio is lesser than unity, it indicates that sink-in has occurred with an actual contact area smaller than the nominal contact area and vice versa. In general indentation, the small strain region of the

indentation test involves a largely elastic stress field with small volumes of plastically deformed material near the corner of the indenter.

In the calculations of a rigid cone indenting a half space, the finite element mesh consists of $26 \times 26 \times 26$ elements. 20 node parallelepiped elements with a $16 \times 16 \times 16$ fine uniform mesh in the vicinity of the indenter tip were used.

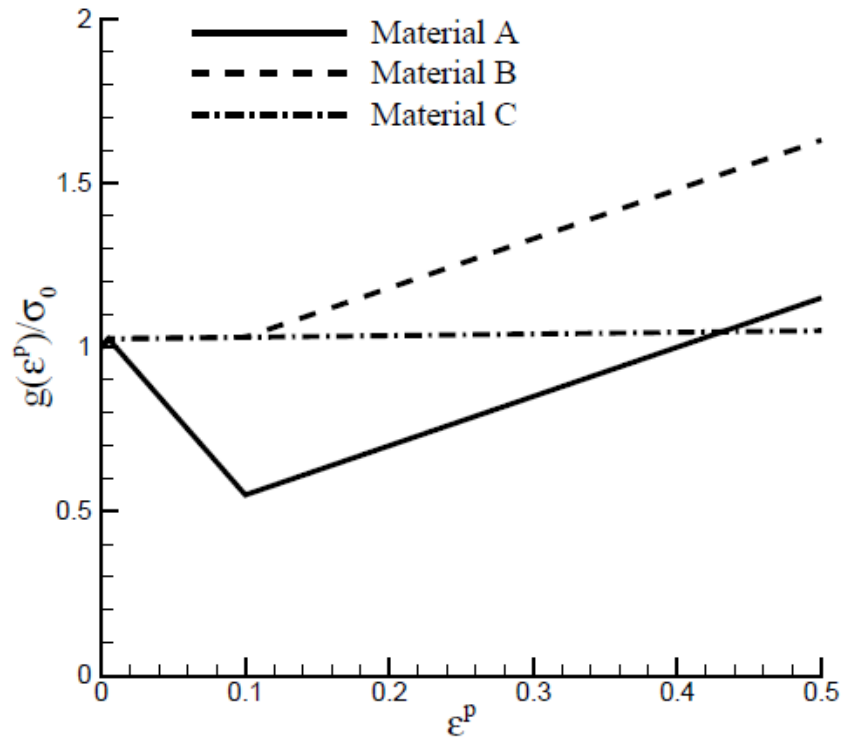


Figure 25: Plot of the normalized hardening functions $g(\epsilon_p)$ used in the calculations.

Calculations are carried out for the same three hardening functions $g(\epsilon_p)$ as in [77], which was found efficient enough to cover the spectrum space of responses quite well. Plots of these hardening functions are shown in Figure 25. These are referred to as material A, material B and material C. For all three materials $h_1 = 5.0$, $\epsilon_1 = 0.005$ and $\epsilon_2 = 0.1$. Material A is the reference material considered in [4], for which $h_2 = -5.0$ and $h_3 = 1.5$. Material B has $h_2 = 0.05$ and $h_3 = 1.5$, while material C has $h_2=h_3 = 0.05$. The mechanical parameters are fixed during the verification process to ensure the consistency of the results and are set as follows:

$E = 100 \text{ MPa}$, $\nu = 0.25$, $\sigma_0 = 1 \text{ MPa}$, $\rho = 1.12 \times 10^{-7} \text{ MPa}/(\text{m/s})^2$, $\dot{\epsilon}_0 = 5000 /s$, $m = 0.02$, $\alpha_p = 0.20$ and $\beta_p = 0.28$. The velocity imposed is 30 m/s , and the rise time is set to be $10 \times 10^{-3} \text{ s}$.

6.3 Conical Indentation

The contact area is taken to be the surface area of the material in contact with the conical indenter projected onto the contact plane. With h denoting the indentation depth and ϕ denoting the angle that the cone makes with the initially flat surface that is indented, the nominal contact area is given by

$$A_{nom} = \pi a_{nom}^2, \quad a_{nom} = h/\tan \phi.$$

Note that with this definition of ϕ , larger values of ϕ correspond to sharper indenters.

Results for an indenter with $\phi = 19^\circ$ were given in [66]. Here, we add the results for indenters with $\phi = 9.5^\circ$ and $\phi = 24.7^\circ$. Results under simulation of polymer indentation with these same three cone angles were presented in [83]. Figure 26 (a&b) & Figure 27 show curves of normalized nominal hardness, H_{nom} , (the ratio of indentation force divided by the nominal contact area) versus indentation depth h for materials A, B and C with $\phi = 9.5^\circ$, $\phi = 19^\circ$ and $\phi = 24.7^\circ$. Although the actual solution is scale independent, numerically a scale independent hardness is not achieved until sufficient finite element nodes are in contact with the indenter. This occurs at $h/l = 0.02$. Qualitatively similar curves of hardness H_{nom}/σ_0 versus h/l are obtained with $\phi = 9.5^\circ$ and $\phi = 19^\circ$ as in Figure 26 (a&b) and Figure 27.

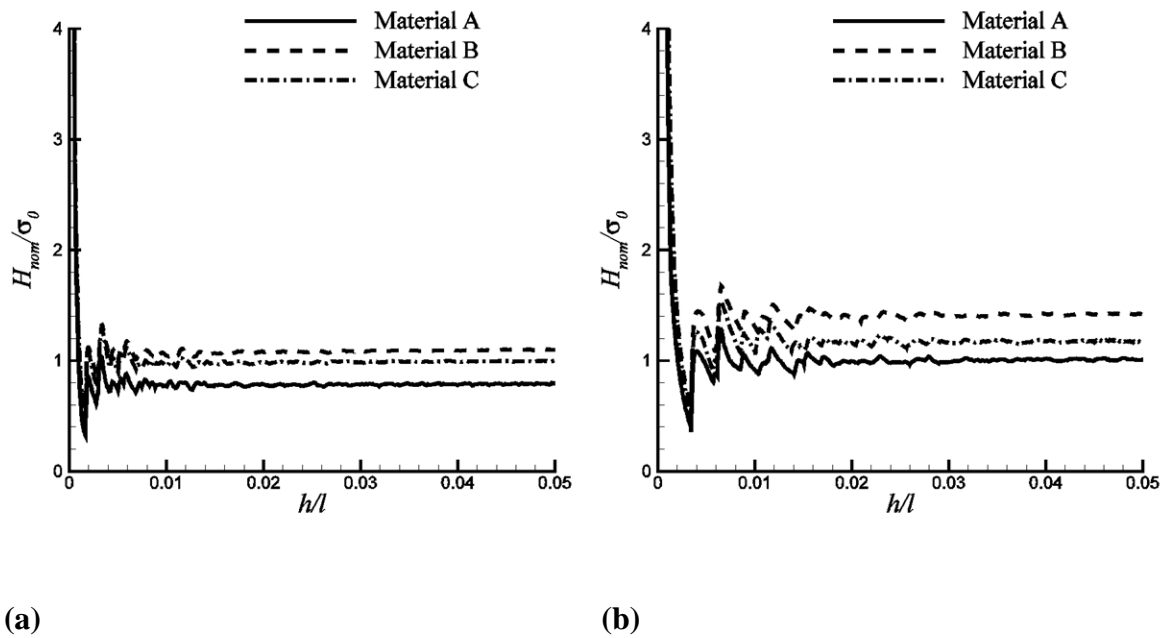


Figure 26: Nominal hardness, $H_{nom} = P/A_{nom}$, versus normalized indentation depth h/l , for a conical indenter with (a) $\phi = 9.5^\circ$, and (b) $\phi = 19.0^\circ$.

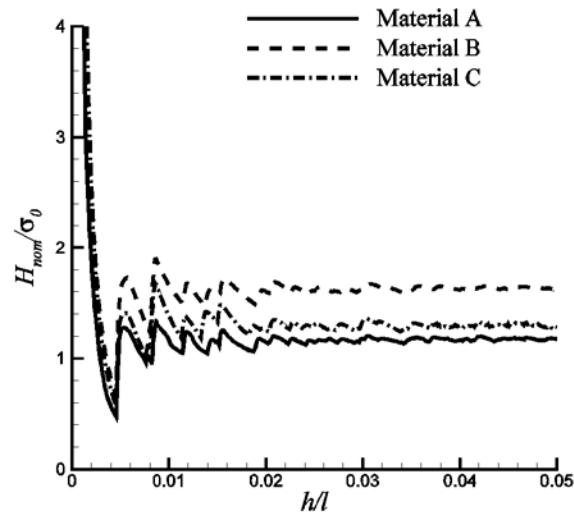


Figure 27: Nominal hardness, $H_{nom} = P/A_{nom}$, versus normalized indentation depth h/l , for a conical indenter with $\phi = 24.7^\circ$.

For all three values of ϕ , as could be expected, material A (softening) has the smallest value of H_{nom}/σ_0 , while material B (hardening) has the largest value. The

difference between materials is greatest for the sharper indenters (larger values of ϕ), indicating that sharper indenters are better at distinguishing the three material setups. The solutions to conical indentation are self-similar, though initially the hardness from calculations is found to shoot up due to the limits of negligible area when the indenter tip touches in the material. Later with increasing punch displacement, the hardness converges to a single value as soon as the self-similarity initiates (Figure 26(a&b) and Figure 27). The values of H_{nom}/σ_o for all the cone indentation results obtained are tabulated in Table 2.

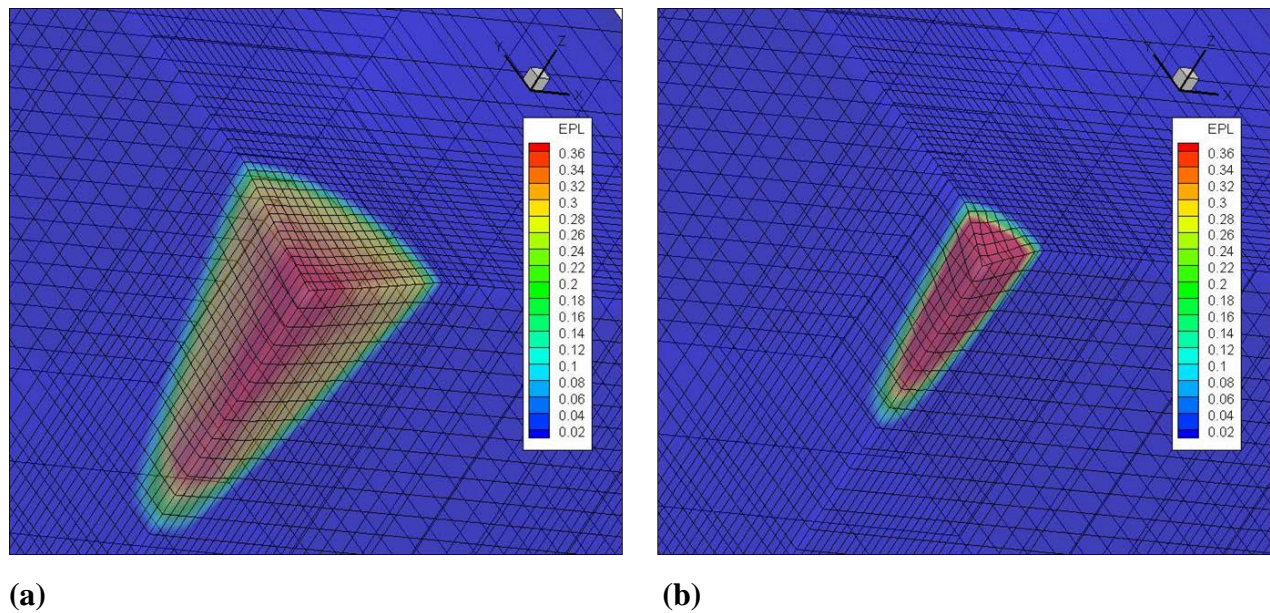


Figure 28: Contour distributions of the normalized plastic strain rate in the proximity of the indenter for (a) Mat. A with $\phi = 9.5^\circ$ and $h/l = 0.04$, (b) Mat. A with $\phi = 24.7^\circ$ and $h/l = 0.04$.

Figure 28 compares the plastic ring development for two cases at the same punch displacement of $h/l = 0.04$, well after the hardness converges in Figure 26(a) and Figure 27. It shows the distribution of normalized plastic strain rate, $\dot{\epsilon}_p = \epsilon_p / (W/H_0)$ to aid in visualizing the deformation mechanism. The plots show that for a wider plastic ring development due to smaller cone angle of $\phi = 9.5^\circ$, a smoother spatial gradient of a plastic ring is induced, as in Figure 28(a). A sharper

spatial gradient in the case of $\theta = 24.7^\circ$ (Figure 28 (b)) is also seen. Interpreting this with respect to the hardness plots of Figure 26(a&b) and Figure 27, implies that for a larger area under punch, and of course, a smoother spatial plastic gradient, the indentation hardness is lower. This would be intuitive, supporting the previous statements on the hardness plots. All three materials setups (though they might have differences among themselves) unanimously agree on this physical observation.

For indentation of an incompressible linear elastic solid by a rigid cone, the ratio A/A_{nom} is independent of cone angle, and equal to 0.405, in [84]. Here, we consider compressible solids, and the ratio A/A_{nom} is strongly dependent on cone angle; hence, the study also includes cone angle effects, as shown in Figure 29(a&b) and Figure 30.

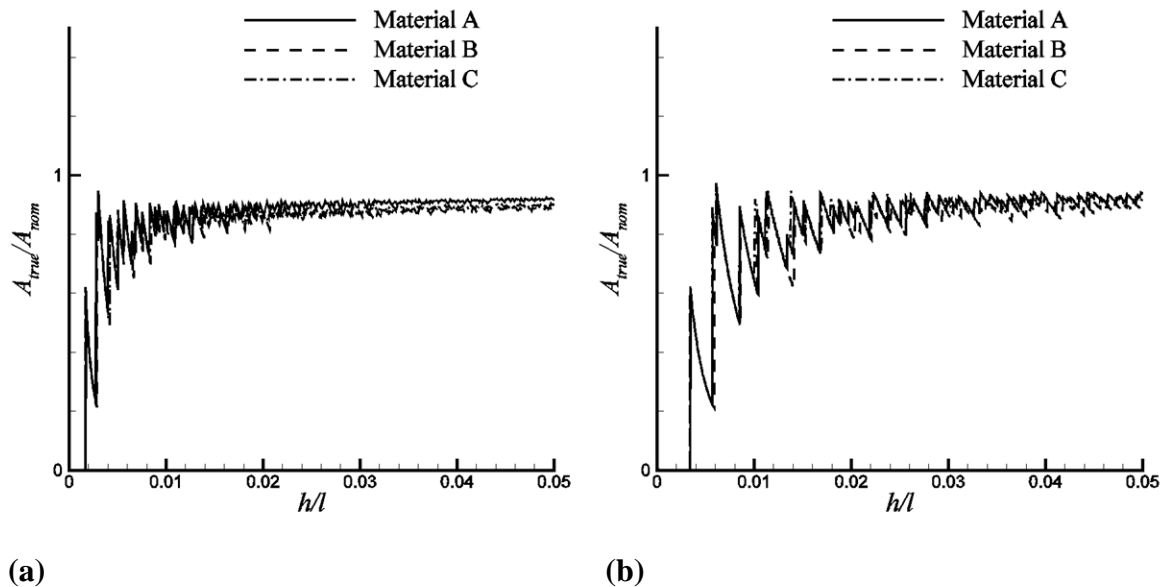


Figure 29: Ratio of true to nominal contact area, A/A_{nom} , versus indentation depth h/l , for a conical indenter with (a) $\theta = 9.5^\circ$, and (b) $\theta = 19.0^\circ$.

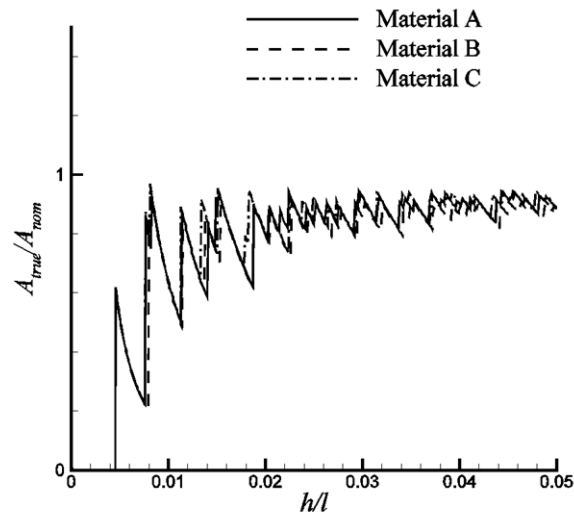


Figure 30: Ratio of true to nominal contact area, A/A_{nom} , versus indentation depth h/l , for a conical indenter with $\phi = 24.7^\circ$.

Figure 29(a&b) and Figure 30 show curves of the ratio of true contact area, A_{true} , to nominal contact area, A_{nom} , for the calculations with $\phi = 9.5^\circ$, 19.0° & 24.7° . Compared with nominal hardness versus indentation depth curves in Figure 16, a larger indentation depth is needed to achieve a more or less constant value of A_{true}/A_{nom} . Because of the oscillations over the indentation depths calculated, the values of A_{true}/A_{nom} in Table 2 are approximate to within ± 0.02 . For all three values of ϕ , A_{true}/A_{nom} is slightly smaller than one, ~ 1.0 , indicating a small amount of sink-in. This contrasts with the behavior for an incompressible Mises solid, where there is substantial pile-up compliant material indentation occurring in [83]. Also, as a consequence of the small amount of sink-in, the true hardness (indentation force divided by A_{true}) is 10-12% greater than the nominal hardness for all three values of ϕ .

Material	$\phi = 9.5^\circ$		$\phi = 19^\circ$		$\phi = 24.7^\circ$	
	H_{nom}/σ_0	A/A_{nom}	H_{nom}/σ_0	A/A_{nom}	H_{nom}/σ_0	A/A_{nom}
A	0.77	0.90	0.99	0.92	1.14	0.91
B	1.08	0.87	1.39	0.86	1.60	0.87
C	0.98	0.88	1.16	0.90	1.25	0.91

Table 2: Tabulated results of the effective hardness of materials under conical indentation under each case.

In Figure 26(a&b), Figure 27, and in Table 2, the nominal hardness is normalized by σ_o , which has the same value of 1MPa for all three materials.

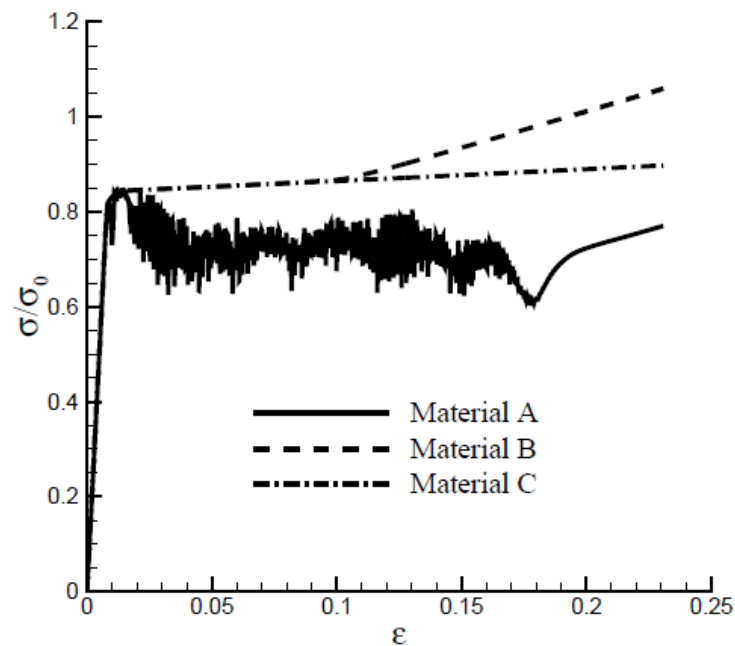


Figure 31: Overall stress-strain response in uniaxial compression for materials A, B and C [66].

For comparison purposes, computed true stress (force/current area) versus logarithmic strain curves in uniaxial compression are shown in Figure 31. As discussed in [66], for materials B and C the overall stress-strain response directly reflects the form of the flow-stress function, while for material A the overall stress-

strain response and the form of flow-stress function differs significantly again, This reassures that the overall response in uniaxial compression is a combination of structural response and material response, to a lesser account. However, for all three materials the effective strengths are less than the reference strength σ_o . For materials B and C it is $Y = 0.86 \sigma_o$, whereas for material A the oscillations center at about $Y = 0.75 \sigma_o$. Thus, computing the ratio of the indentation hardness (H_{nom}) to effective strength(Y) for the specific viscoplastic material here leads to the following results: for material A, the values of H_{nom}/Y are 1.02, 1.32 and 1.52 for $\phi = 9.5^\circ$; 19° and 24.7° , respectively. The corresponding values of H_{nom}/Y are 1.77, 1.62 and 1.86 for material B and 1.14, 1.35 and 1.45 for material C. The experimentally measured value for one such foam is 1.5 as from [61] and in range of the simulated results.

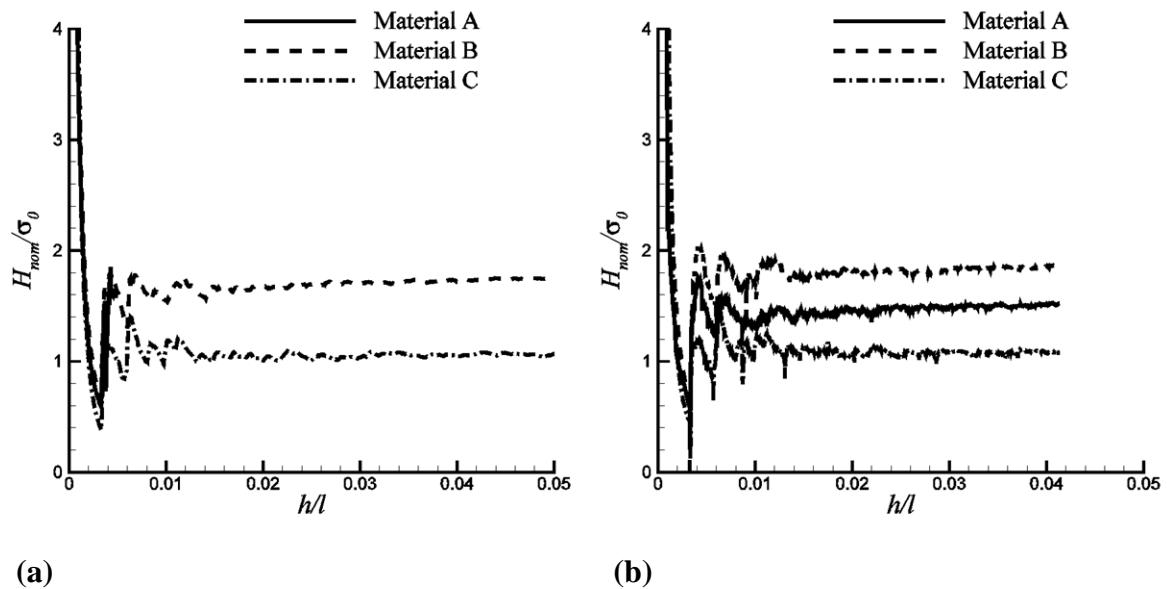


Figure 32: Nominal hardness, $H_{nom} = P/A_{nom}$, versus indentation depth h/l , for a conical indenter with $\phi = 19^\circ$, (a) with plastic incompressibility ($\beta_p = 0.33$) and (b) with near incompressibility ($\beta_p = 0.33$, $\nu = 0.49$).

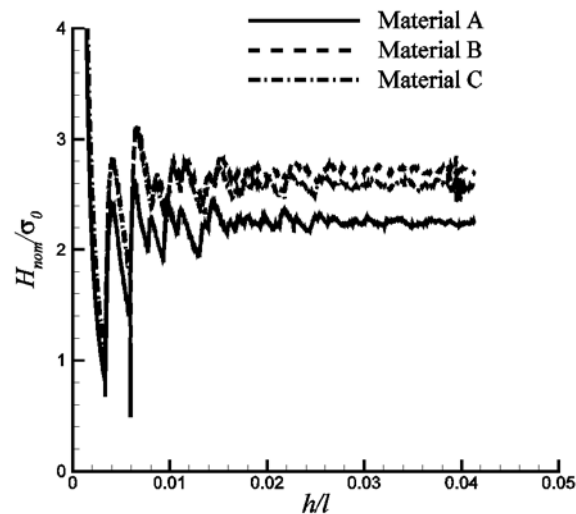


Figure 33: Nominal hardness, $H_{nom} = P/A_{nom}$, versus indentation depth h/l , for a conical indenter with $\phi = 19^\circ$, with near incompressibility ($\alpha_p = 0.33$, $\beta_p = 0.33$ & $\nu = 0.49$).

Thus, when the hardness (nominal or true) is normalized by the compressive flow strength there is essentially no difference between the nearly zero hardening solid material C and the hardening-softening-hardening solid material A for the two sharper conical indenters.

For a slightly hardening (lower hardening slopes of the hardening function) Mises elastic-plastic solid used to model metal plasticity, the ratio of indentation hardness to flow strength is $H_{nom}/Y = 3$, as found in [66], with $\phi = 19^\circ$ using the same formulation as used in the calculations here. Material C differs from such a conventional Mises solid in three respects:

- 1) plastic compressibility;
- 2) plastic non-normality; and
- 3) a relatively soft elastic stiffness, $\sigma_o/E = 0.01$.

To explore the relative roles of these on affecting the ratio H_{nom}/σ_o , calculations were carried out with $\phi = 19^\circ$ for materials similar to A and C. In one case they were nearly incompressible and in the other case they satisfied plastic normality.

The values of the material parameters used to obtain the results in Table 2 will be referred to as the reference values of material parameters.

The material parameters changed to model nearly incompressible material response are $\nu = 0.49$ and $\beta_p = 0.33$. All other material parameters, in particular $g(\epsilon_p)$, remain the same as the reference values for materials A and C, respectively. For the incompressible material A, $H_{nom}/\sigma_o = 1.50$, while $H_{nom}/\sigma_o = 1.07$ for the incompressible material C. Thus, for these nearly incompressible materials, material A has greater values of indentation hardness than does material C; the opposite is found for the corresponding compressible materials. The difference in indentation hardness also reflects the difference in hydrostatic stress levels under the indenter. For the incompressible material A, the maximum magnitude of $-tr(\tau)/3\sigma_o$ is 2.06, while for the incompressible material C, the maximum magnitude of $-tr(\tau)/3\sigma_o$ is 0.96. The values of A/A_{nom} for materials A and C are 0.91 and 0.98, respectively. The nearly incompressible and compressible versions of material A have almost the same amount of sink-in whereas, sink-in is almost absent for the nearly incompressible material C.

For the calculations with plastic normality, the values $\alpha_p = \beta_p = 0.28$ were used with all other material parameters fixed, so that only β_p was changed from its reference value. For the plastic normality material A, $H_{nom}/\sigma_o = 1.20$ while for the plastic normality material C, $H_{nom}/\sigma_o = 1.51$. In this case, the ordering of the values of H_{nom}/σ_o is the same as in Table 2. The value of A/A_{nom} is 0.91 for both the plastic normality materials A and C and it is essentially the same as for the corresponding materials (A and C) with the reference (default) values of material properties, showing that plastic normality does not affect the equivalence of materials A and C observed before. By these calculations, various material mechanisms, which influence the conical indentation resistance, were identified.

For validation, the presented results were cross-checked against the experimental indentation results of foams in [85], and it was able to capture the mechanical response.

6.4 Flat-Punch Indentation

The half-space model is indented under a flat-square indenter, and hence the area of contact remains constant with increasing indentation depth ratio h/l , unlike under a conical indenter (hence the results are scale-dependent, and the solutions are no more self-similar). Because of the usage of small strain theory and to make sure the results do not include unwanted substrate effects of sample size effects, a suitable value of punch displacement has to be selected here. A value of punch displacement, greater than a mesh element and still smaller than the whole sample size was used and the simulations were carried out only until small h/l ratios of ≤ 0.05 .

<i>Material</i>	<i>Defaultvalues</i>	$\beta_p = 0.33$	$\beta_p = 0.33, \nu = 0.49$	$\beta_p = 0.33, \alpha_p = 0.33, \nu = 0.49$
A	19		60	40
B	43	75	95	75
C	8	15	17	55

Table 3: Tabulated values of the plateau slopes of materials under flat punch indentation under each case.

Results for flat-square indentation are shown in Figure 34 and Figure 35 as before. Unlike for conical indentation, the punch displacement h , here is normalized with the scale factor of the punch width of w to account for scale dependence. Under conical indentation, the area of contact starts self-similarly increasing with punch displacement, and hence the hardness (indentation force/area of contact) curve comes down to stabilize to a plateau. In contrast, the area is constant here and the indentation resistance keeps increasing with

indentation depth h . Hence, this case is scale-dependent with the reference scale of punch width being 0.1406 and the area of punch being 0.0197. Out of the half-space area being, 1×1 , the punch area is less than 2% of the total area. Initially hardness increases linearly, elastic followed by the plateau, due to plasticity which is formed around $h/l = 0.002$. The plateau region starts at $H_{nom}/\sigma_o = 0.8$ for Material A and is distinctively higher at $H_{nom}/\sigma_o = 1$ for Materials B and C, which corresponds to a lower second hardening slope h_2 of flow stress definition of Material A compared to Materials B and C.

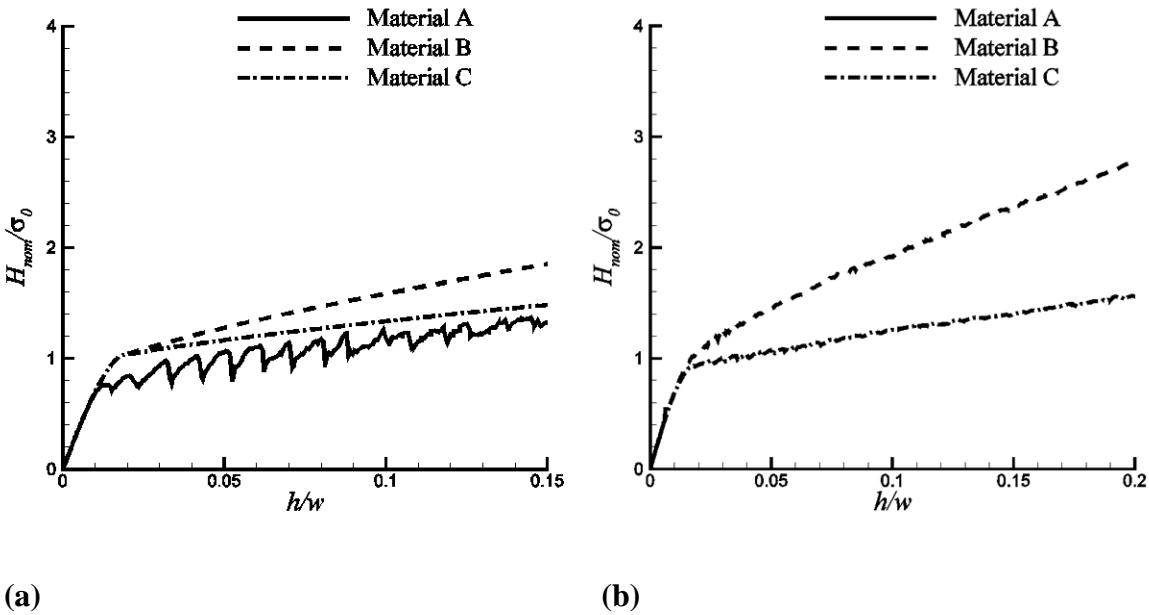


Figure 34: Nominal hardness, $H_{nom} = P/A_{nom}$, versus normalized indentation depth h/w , for a flat square indenter with (a) default $\beta_p = 0.28$, and (b) $\beta_p = 0.33$.

As noted in the Table 3, the higher plateau slope of material B than material C corresponds to the higher third hardening slope of flow-stress function h_3 in Figure 34(a). The plateau slope of Material A is the least, followed by that of material C and finally material B, which follow the respective flow-stress function slopes trend. The oscillations noted in material A under default settings were unique to

only the default setup of plastic compressibility and non-normality. Hence, Figure 34(a) was cross-checked with the contour distributions of plastic strain rate to understand the undulations. The plastic ring formation looked normal or these undulations were not high enough to cause any instability to be noted in the deformation evolution.

With $\beta_p = 0.33$ (plastic incompressibility) the influence of the flow-stress function on the plateau slope increases for all three materials. Material B has a significant increase in slope compared to changes in other two materials, as it has a higher flow stress from the second hardening strain level, as shown in Table 3.

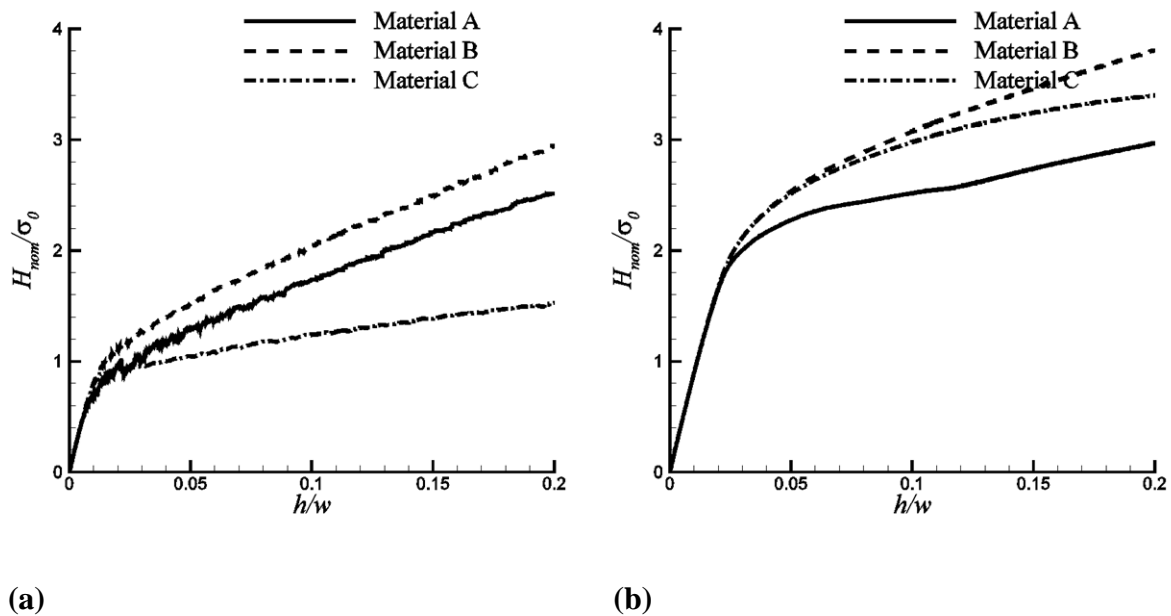
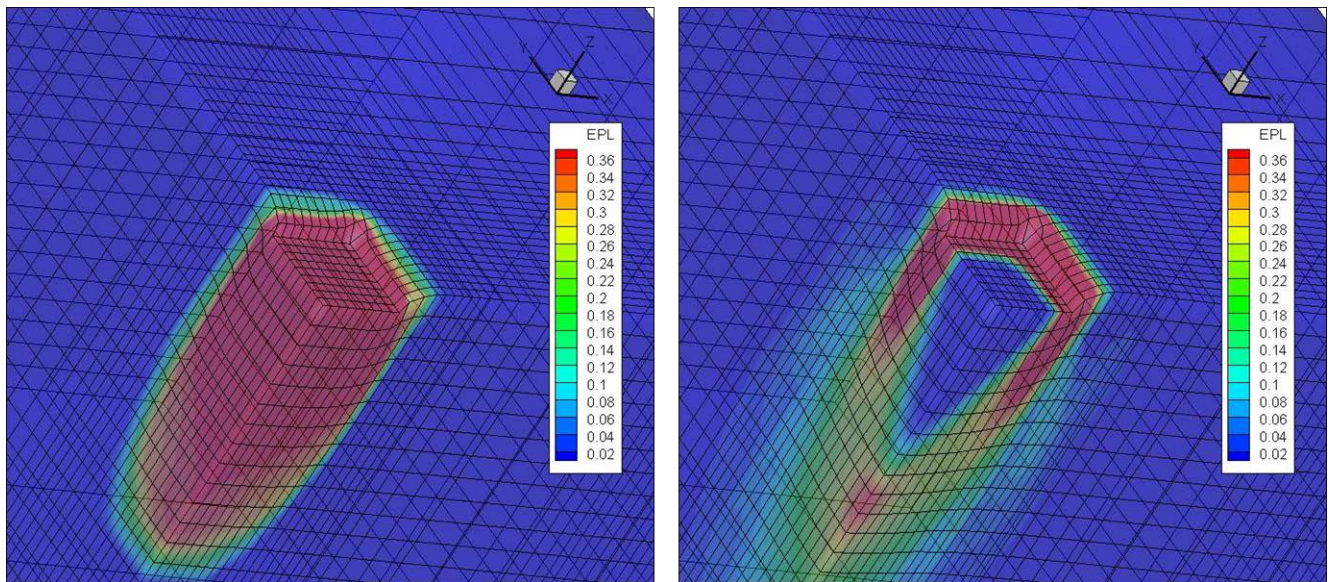


Figure 35: Nominal hardness, $H_{nom} = P/A_{nom}$, versus normalized indentation depth h/w , (a) for a flat square indenter near incompressibility, and (b) with plastic normality.

Under $\beta_p = 0.33$ and $\nu = 0.49$, which is the near-incompressibility condition, there is even more increase in the plateau slopes. Under near incompressibility and plastic normality, $\alpha_p = 0.33$, $\beta_p = 0.33$ and $\nu = 0.49$ (the Mises condition), the plateau initiating hardness levels increase for all three materials to $H_{nom}/\sigma_0 = 2$,

nearly twice that of previous conditions. This is clearly an effect of normality, as seen before. To further investigate this, the contour distributions of the plastic strain rate, $\dot{\epsilon} = \epsilon_p/(W/H_0)$ were analyzed. Interestingly, the plastic ring evolution with strain looked like the self-similar expansion of the ring for the default case of Material A in Figure 33(a). The same was found for Material A with near incompressibility and plastic normality conditions in Figure 35(b). It showed that the plastic ring was pushed towards the boundary of the general ring, forming only a bounding high concentration plastic ring, right from the initiation as seen in Figure 36(b).



(a)

(b)

Figure 36: Contour distributions of the normalized plastic strain rate in the proximity of the indenter for (a) Mat. A, default at $h/w=0.28$, (b) Mat. A with incompressibility and plastic normality at $h/w=0.28$.

Flat punch indentation proved much better at distinguishing among the three material setups than conical indentation, which was unable to distinguish, even qualitatively. This might be due to the sharp conical indenter not allowing any substantial area under punch to resist taking in any material effects initially. Thus,

the further explorations are carried out with material effects only in the case of flat-punch indentations.

6.5 Material Inhomogeneity: Strength Gradient Effects

To extend the analysis of strength gradient effects under indentation, the *SM* function was recalled here to simulate materials with a strength gradient in the vertical direction, over the height of the film considered. A positive gradient denotes a material of lower strength at the bottom and linearly increasing strength towards the top, and vice versa for a negative gradient material. If the compression results are tried to be extended here intuitively, it would also be required to take into account the non-uniform stress distribution under indentation over the height, unlike the uniform compression. High stress concentration noted directly beneath the indenter fades out with depth. Hence, it would be expected to give rise to different responses under positive and negative gradient materials, unlike in compression. This means that the indentation deformation path can be expected to be sensitive to the gradient direction, unlike the uniaxial tests.

The effect is shown in terms of the hardness observed at consecutive punch displacement with different gradients in Figure 37 (as there is not a clear distinction of the slope of the plateau region which grows in a concave manner, it is preferable to use hardness at successive distinct points of punch displacements for comparison). As described beforehand, in contrast to compression, gradient sign symmetry breaks down under indentation, due to localized plastic flow from the top. Hence, when the material is stronger at the top, it resists more.

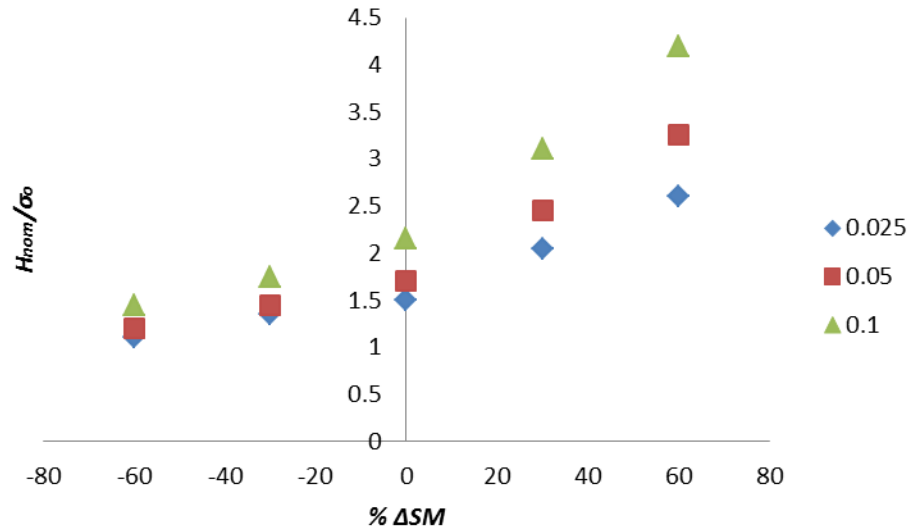


Figure 37: Plot of normalized hardness noted at a series of different punch displacements (legends indicate the hardness as a series at consecutive normalized punch displacement, h/l) vs. the percent of strength variation over the height of the material.

This creates a higher hardness for the plastic zone initiated to overcome this strength barrier. If the material is weaker at the top, it is even easier for the plastic zone initiation than in a default material with uniform strength. Hence, the negative slope (~ -0.01) for the negative gradient and a higher positive slope (~ 0.03) in stress levels for the positive gradient is noted as shown in Figure 37.

6.6 Material Space (Flow Stress) Exploration

The simplified, three-piecewise nature of the flow strength curve lends itself well to a systematic study of changes in behavior with variations in its slopes and transition strains as discussed in this section, in the same spirit as under [4]. Hence we try to move the minima around, by changing a single parameter to investigate their individual respective effects, while fixing all other parameters. To start with, the first hardening piece was set at $h_1 = 5.0$, $\epsilon_1 = 0.005$ and the second softening

piece (h_2, ϵ_2) was varied, changing the depth and width of the minima ($\frac{g(\epsilon_2)}{\sigma_0}$), as shown in Figure 38.

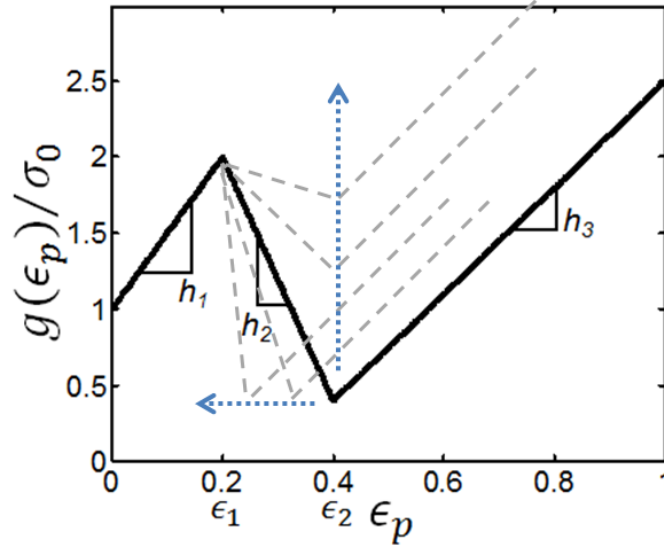


Figure 38: A schematic showing the methodology used to move the minima position in the directions of the arrows, indicating changes in depth and width of the minima.

The third hardening slope was kept constant as $h_3 = 1.5$. As we are dealing with length-scale sensitive results, it should be mentioned that the punch width in all these calculations was kept as 0.15, and the punch area was thereby 0.0225 out of the half-space area which was, 1.6 x 1.6. The depth $\frac{g(\epsilon_2)}{\sigma_0}$ of the minima is denoted by ‘G’, and the width is given by the second transition strain $E_2(\epsilon_2)$. The output response of hardness is as shown (u/p , punch displacement/punch width, normalized by the length-scale) in Figure 38. The hardness response is seen to have a lot of oscillations with deeper minima, and the oscillations die down with increasing ‘G’ value (the increased material hardening). This is due to the hardening providing stability to the material.

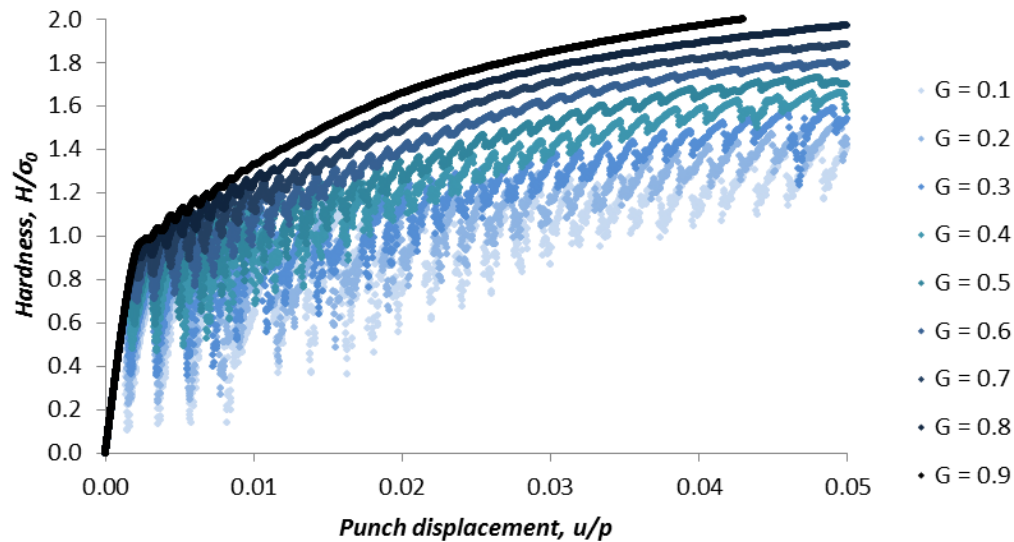


Figure 39: Plot of normalized hardness (H/σ_0) vs. normalized punch displacement (u/p), with each colored curve representing responses of individual cases of G (depth of minima).

The initiating region of the plateau has a few undulations due to the inertia of plastic ring formation. Another interesting observation is that the trend and slopes of the hardness do not vary considerably with the minima position. However, the plateau converges to a hardness value of $\sim 1\sigma_0$ for the deepest minima case, whereas it keeps increasing with ‘ G ’ and reaches $\sim 2\sigma_0$ for the highest ‘ G ’ value, which is similar to the Maxwell stress correspondence noted in tensile results as well (Figure 18).

The figures of merit used to quantify the output results were

- 1) the hardness vs. displacement plots and
- 2) the radial(r) and the axial (d) growth limits of the plastic zone, propagating in the material from the indenter punch area towards the bottom and outwards observed in simulations, as shown in Figure 40.

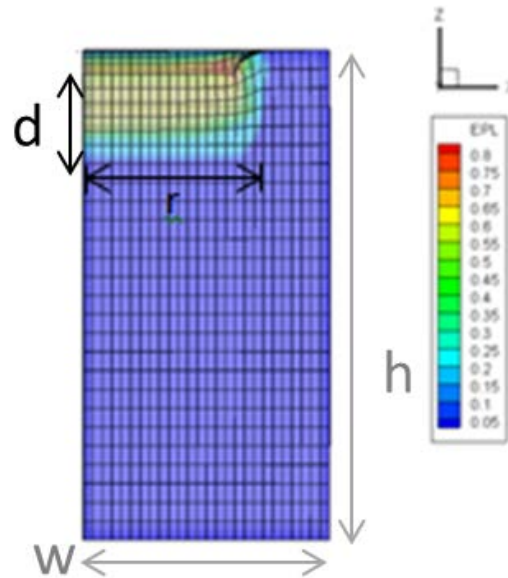
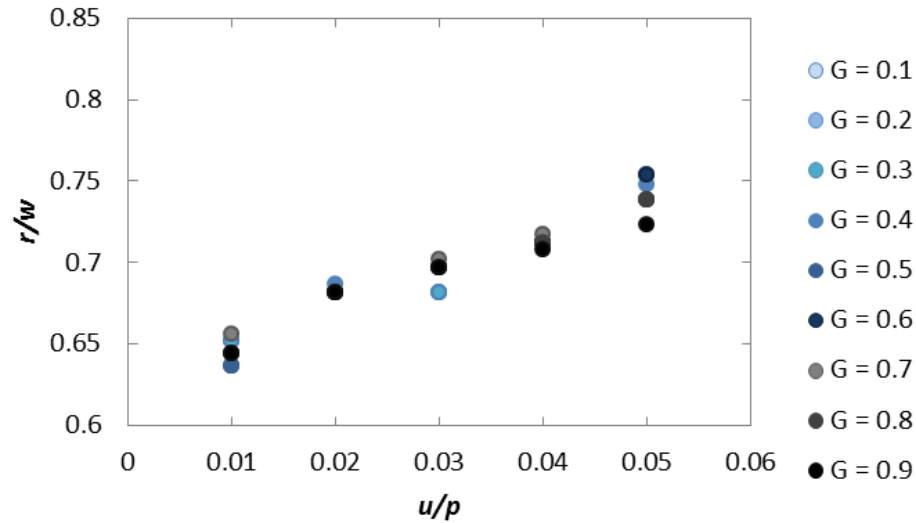


Figure 40: The side view schematic of the 3-D contour plot of the cumulative plastic strain shown. The radius, r and depth, d of the plastic zone are shown, normalized with the side length, w and total height, h of the model respectively.

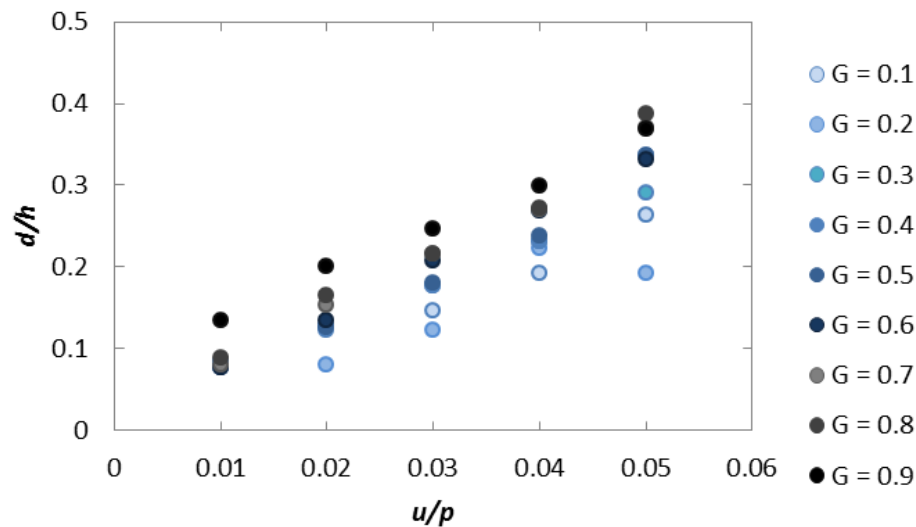
As expected, with increasing hardening (as we go from ‘G=0.1’ to ‘G=0.9’) the radial and axial propagation of the plastic ring reduces as seen in Figure 41. The radial propagation at u/p of 0.05 attains the maximum value of 0.77 and comes down to 0.65 of normalized hardness, which is a significant amount of change. A similar change is found for the axial propagation. The curves tend to be concave for the softer materials (G=0.1), indicating the gradual reduction in propagation. It transitions to be a linear, undiminishing growth for higher hardening. But the calculations here could not be performed to better accuracy to affirm this, as the point of the plastic ring front was not distinct.

Figure 42 shows similar effects observed due to an increase in minima width alone. The minima position is varied from strains of 0.1 to 0.5. With the minima width being lower, the third hardening resumes at earlier strains, restricting the propagation of the plastic zone. Hence, a concave reduction in radial propagation could be noticed. However, with increasing minima width, i.e., with

longer strain range for softening, the propagation has a linear, undiminishing growth. The details under this section could be qualitatively captured only trend-wise.

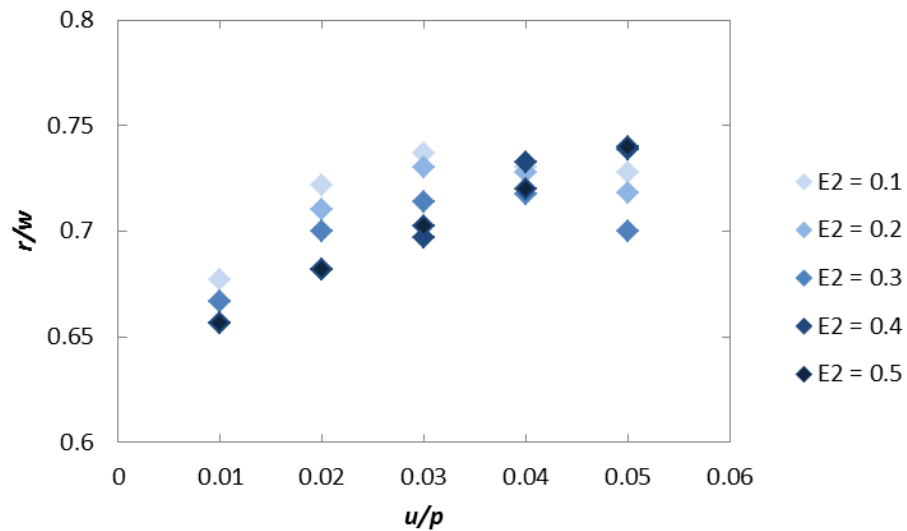


(a)

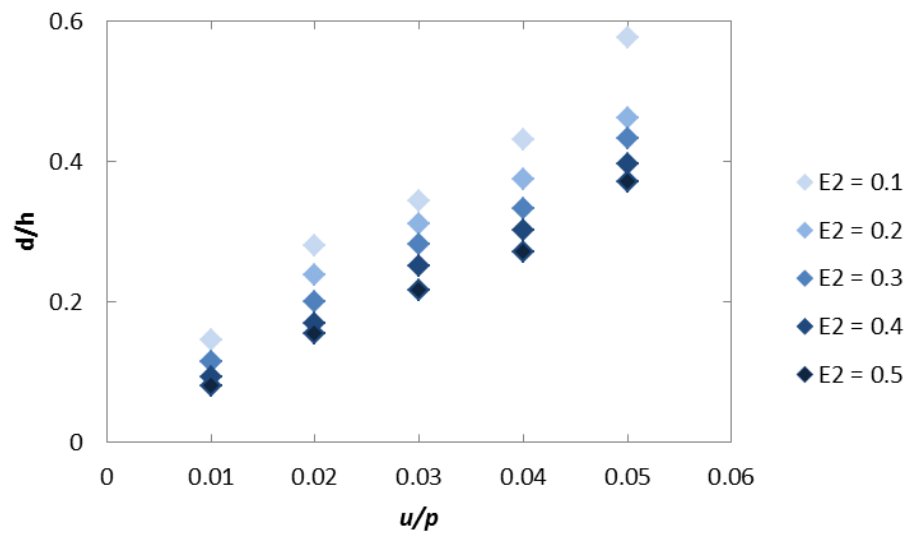


(b)

Figure 41: The plot of (a) normalized radius, r/w vs. punch displacement, u/p and (b) normalized depth, d/h of the ring of plastic zone formed vs. the normalized punch displacement, u/p as a series with respect to the minima depth increasing from 'G=0.1' to 'G=0.9'.



(a)



(b)

Figure 42: The plot of (a) normalized radius, r/w vs. punch displacement, u/p and (b) normalized depth, d/h of the ring of plastic zone formed with the normalized punch displacement, u/p as a series with respect to the minima width increasing from 'E2=0.1' to 'E2=0.5'.

It is due to the different quantitative observations under different settings of other parameters. For example, if h_1 & ε_1 are set to be different and if the same minima exploration using h_2 & ε_2 is repeated, only the qualitative observations would hold, but the quantitative correlations is found to vary significantly. Hence, quantitative results are not reported here, as the main focus is to derive qualitative correlations. It is also to be noted from both Figure 41 and Figure 42 that the axial propagation also tends to be always lower than the radial propagation by one-third, which is explained by the higher level of hydrostatic stress in the radial direction than in the axial direction underneath the indenter.

Experimental flat punch nanoindentation results of a compliant foam [61] exist to compare with in the case of flat-punch indentation simulations. It is observed that the indentation output from simulations captured the salient features as shown from an experimental stress-strain curve, except for the nano-shearing effect of vertically aligned tubes, which could not be captured by a continuum model with mesh compatibility conditions. This conical and flat punch indentations are of course demonstrated by several previous models as well [86] & [45] respectively. This model was able to capture the experimental response of foam-type materials. The additional information obtained from this model is the extraction of material response in terms of compressibility and other factors.

Chapter 7

Comparative Study and Conclusions

7.1 Introduction

We have carried out finite element analyses of uniaxial tests and indentation using a constitutive relation for strain rate-dependent, plastically compressible solids with plastic non-normality. The flow rule was expressed in terms of the effective Kirchhoff stress, and the hardness function had three piece-wise linear regimes. This was formulated to be of the hardening-softening-hardening type. The slope and the extent of the second softening linear regime were varied. Depending on the parameters characterizing this regime, the deformation modes that emerge under each simple loading condition were explored. With the results explained, at least in principle, the simulated overall stress-strain response gave considerable insights into the plastic properties of the material. Together with the plastic strain contour plots, which depict the evolution of instabilities, this provided deeper insights.

The material hardening response is found to be a coupled effect of physicality of both the test and the material effects. Determining the underlying physics of the experimental observations requires rigorous multi-scale material modeling. However, some of these phenomena are suggested to arise due to the differences in boundary conditions among the desired loading configurations (i.e. indentation vs. compression vs. tension).

7.2 Summary

We now summarize the major findings of the data reduction scheme for extracting the material properties. First, the model was capable of extracting the material property from simple mechanical test data (e.g., predictions about hardening response from the stress vs. strain response). Evaluation of the tests based on their sensitivity to characterize the material is also outlined here. The tests are ranked from the highest sensitivity to the lowest. Tension and compression here denote the uniaxial tension and compression results. These results hold only for the particular viscoplastic constitutive setup considered here and may not hold universally.

Deformation modes under each test are expectedly unique such as sequential buckling under compression, propagation band formation, diffused and localized necking under tension. Only plastic zone propagation is found to occur under both indentation tests. The tests were carried out changing one of the parameters while keeping others constant at default values (see Chapter 3). Therefore, the quantified relationships here may have slight changes with respect to another set of material parameters, although the order of the relations remains the same. The most quantitatively sensitive test would have the least multiplier of the stress-strain feature, on the right side of the equations mentioned below. In all the rankings below, the ability of the tests to qualitatively distinguish the material property is given a higher priority, than their quantitative distinguishing ability. It is to be noted that all stress and hardness terms mentioned below are normalized with respect to reference strength and hence the proportionality constants do not have units.

7.2.1 Strength Gradient

The uniaxial tests are insensitive to the direction of strength gradient in the material, due to an approximately uniform stress distribution. Hence the different directions of strength gradients have similar stress-strain response. Only with the help of cumulative strain contours evolution maps, the direction of gradient can be predicted. The point of instability initiation from such contours, indicates the point of the weakest strength.

Taking the simplest cases of linear strength gradient in a material setup over the height, the plateau stress is found to be affected by the gradient. The percentage of strength difference between the heights of a pillar ($\% \Delta SM$) is related to the plateau slope ($P.S$) under compression as,

$$\% \Delta SM \approx (C) P.S,$$

where, C is a constant with no units in this case. Under compression, C takes the value of 26. The same under tension is given by 16.6. However, the indentation simulations have non-uniform distribution and hence the flat punch indentation is found to be sensitive to the direction of the strength gradient. For positive gradients, the same ratio is given as follows.

$$\% \Delta SM \approx 28.5 P.S.$$

For negative gradients, it's given by,

$$\% \Delta SM \approx -40 P.S,$$

implying C values of 28.5 and -40 in the two cases respectively. Flat Punch Indentation is able to qualitatively distinguish the direction of gradients and hence ranked number one, though the quantitative sensitivity to gradients of both signs

seems comparatively less significant to that of other tests. Quantitatively, tensile tests are found to be the most sensitive and hence ranked second. Hence the ranking in capturing strength gradient is given as

- 1) Flat Punch Indentation
- 2) Tension
- 3) Compression
- 4) Conical Indentation

7.2.2 Hardening Function

Flow stress inducing instabilities under uniaxial compression requires a hardening-softening-hardening condition, whereas under uniaxial tension, different instabilities occur under different types of three piece-wise linear functions. However, the deformation paths exhibiting the plastic zone propagation under conical indentation and flat-punch indentation do not require any conditions on the flow stress function. Hence, to sum up, only uniaxial compression instability required the hardening-softening-hardening condition of the flow stress function.

The plateau slope of the compressive stress-strain response was proportional to the II^{nd} softening slope ($II^{nd} H.S$).

$$II^{nd} H.S \approx (D) P.S$$

where, D is the proportionality constant, unit-less in this case and found to be 0.035. It is to be noted that this result holds only within the small window of the hardness function, which produces sequential buckles. In the case of uniaxial tension, the plateau slope ($P.S$) of the propagating band instability mode correlated with the equivalent Maxwell flow stress ($F.S_m$). Hence, the linear relation between them is given as

$$F.S_m \approx (E) P.S$$

where, E is a constant unit-less, 0.9. Other modes of instability under tension did not exhibit any significant dependence on the flow stress slopes quantitatively, but rather predicted the trend, as under the 1D simplified model. Therefore, it is found to be qualitatively better than the compression test.

Conical indentation is not qualitatively sensitive to the hardening function slopes and the quantitative difference noted in plateau hardness is also not significant to be relied upon. Flat punch indentation was found capable of distinguishing between the hardness setups (representative materials A, B and C). Flat punch indentation, exhibits the linear relationship as,

$$III^{rd} H.S \approx 0.0414 P.S$$

The ranking of tests below reflects from the above results. The additional points given to tension than compression, comes from the fact that the tensile tests predict the trend of the hardening function better, though not for their individual slopes. Tension test hence leads compression in the ranking system.

- 1) Flat Punch Indentation
- 2) Tension
- 3) Compression
- 4) Conical Indentation

7.2.3 Near and Plastic Compressibility

Compressibility adds to interplay with hardness function and it is important to reinstate here that the flat hardening functions are insensitive to the compressibility changes. All the relations reported here, hold for the hardening or softening setups

only (Materials A and B are taken here for reference). This also means that with a different hardening setup the sensitivities to compressibility change, but the order of the relationships is found to hold good.

The compressibility is changed by varying the parameter, β_p . A material setup with $\beta_p = 0.33$, allows plastic incompressibility, whereas, when the value of β_p is lowered, the plastic compressibility increases. The parameter space was varied from 0.1 to 0.33, thereby examining the relation of β_p with the stress-strain response. The uniaxial tests are insensitive to the changes in β_p , within the considered range of operation. The stress-strain responses do not show appreciable differences. Whereas, under conical indentation, the normalized effective hardness (H) was correlated to the change in ($\Delta\beta_p$) as follows,

$$\Delta\beta_p \approx (F) H,$$

where, F is again unit-less and has a value of 0.2 here. There is no slope associated with conical indentation hardness responses, only a flat plateau is noted with expected self-similar solutions. The flat punch indentation, related the slope of the hardness response ($S.H$), to the changes in compressibility ($\Delta\beta_p$) is as follows,

$$\Delta\beta_p \approx 0.002 S.H$$

Similar was the case under near compressibility where along with $\beta_p = 0.33$, the elastic poissons' ratio was also set at $\nu_e = 0.49$. For Compressibility, the ranking of deformation paths hence follows as:

- 1) Flat Punch Indentation
- 2) Conical Indentation
- 3) Tension and Compression

7.2.4 Plastic Normality

With plastic normality also contributing to the interplay, the effects get amplified. The normality condition in general for all tests tends to increase the stress response levels. The correlations between the effective hardness (H) or the slope of hardness (SH) and the change in β_p , ($\Delta\beta_p$) respectively under each deformation path is as given below.

No significant change was noted under uniaxial tests, except for the reduction of oscillations in the curves with increased normality. Under conical indentation,

$$\Delta\beta_p \approx 0.1 H$$

Under flat punch indentation,

$$\Delta\beta_p \approx 0.0014 SH$$

The qualitative trend of the responses was not distinguishable. Therefore, the ranking of deformation paths is given as:

- 1) Flat Punch Indentation
- 2) Conical Indentation
- 3) Tension and Compression

A more detailed outline of the evaluating strategy is given in Appendix A.

7.3 Conclusion and Future Work

Developing a straightforward relation between the mechanical stress-strain response and material morphological details from this constitutive setup is difficult. Hindrances exist due to the missing links in the setup, such as the exact relations between material morphological details (i.e. the relative density, cell

waviness, etc.) and the material responses (i.e., hardening function, strength gradient, compressibility etc.). However, mathematically updating the constitutive setup of continuum-scale model, with some suggestions taken from smaller-scale simulations [46] can help in the material response (property) characterization. It is to be reiterated that the results presented here are specific to the materials pertaining to this particular constitutive setup, thereby restricting the material response characterization only to such materials.

Although many other plasticity [87] models have already captured some of the explained instabilities, the ability of this model to extract material response in terms of four different material properties comes to be its advantage. This is possible due to the specific formulation in terms of material properties such as the hardening response, plastic compressibility and such, which serve as the material inputs. Interestingly, considering the results from another work [88], the experimental flat-punch test data could be fitted more closely to a spherical cavity model, in polymeric systems. The plastic properties of the sample extracted from such a flat punch indentation model and experiment are thus reported to be measured accurately from point to point. This work also suggests flat-punch to be one of the best methods for capturing plastic properties. The results support our finding that flat-punch indentation captures the material properties better than other simple mechanical tests considered here.

As the relevant experiments of foam-type materials revealed isotropic nature, the anisotropic setup was not explored. This model could be extended to be anisotropic in nature and explored as a future work, if the anisotropic effects are observed under a different scale of testing. Removing the symmetry conditions and extending the model to be non-axisymmetric pillar type and of infinite space for 3D indentation would be an extension of this work to explore the anti-symmetric

deformation modes. This is expected to affect the pile-up/sink-in conditions under indentation as well.

Appendix A

The tables shown below summarize the material aspects and the sensitivity of the tests on them, respectively. Some of the material aspects (analyzing criteria) which could be quantified were expressed in figures in brackets, while others were very subjective to other parameter changes, and thus only the qualitative correlations are shown. The figures in brackets denote the slope of the figure of merit (under ‘compression,’ ‘tension’ columns) under each column, with respect to the variation of parameters shown in the first column, in corresponding rows (under the ‘Features’ column).

Table 4: Summary of comparison of the test results- I

Features	Compression	Tension	Conical Indentation	Flat Indentation	Punch Indentation
Flow Stress on Instability 1)Required condition 2)Plateau slope	1)HSH necessary 2)Qualitatively proportional to the II softening slope	1)HSH not necessary 2)Qualitatively proportional to the maxwell flow stress	1)NA 2)Qualitative trend unaffected by flow stress.	1)NA 2)Qualitatively proportional to the II softening slope.	
Gradient effects 1)Sym/anti-sym 2)Plateau slope	1)symmetrical 2)Linearly increasing with gradient (0.045)	1) symmetrical 2)Linearly increasing with gradient(0.06)	1)NAC 2)NAC	1)Anti-symm 2)Linear, +ve gradient,(0.035), -ve grad (-0.025)	

Deformation Mode	Sequential buckling	Band formation, diffused and localized Necking	Plastic zone propagates from top to bottom	Plastic zone propagates from top to bottom
Overall flow stress effects: increase in 1)I hardening peak point 2)II softening 3)III hardening	1)Instability Initiating stress increases(0.6) 2) Plateau slope increases 3)Plateau slope increases	1)Instability Initiating stress increases(0.65) 2)Affects maxwell stress and thereby the plateau 3)Diffuses out localization	1)NAC 2)NAC 3)NAC	1)Instability Initiating stress increases(0.85) 2)Plateau slope increases 3)Plateau slope increases

Table 5: Summary of comparison of the test results- II

Features	Compression	Tension	Conical Indentation (slope of mentioned figure of merit vs. β_p)	Flat Punch Indentation(slope of mentioned figure of merit vs. β_p)
Plastic Incompressibility	NAC	NAC	Effective hardness proportionally increased.(~5) Difference among three materials(A,B and C) get higher. (1.5 times)	Effective hardness slope proportionally increased. (~600)
Near incompressibility	NAC	NAC	Effective hardness linearly increased.(~10) Difference among three materials(A,B and C) get higher. (2	Effective hardness slope proportionally increased. (~1040)

			times)	
Plastic normality + near incompressibility	NAC	NAC	Effective hardness proportionally increased. (~30) Plateau initiating stress increased (~2.3) Difference among three materials(A,B and C) get higher.(1.5 times)	Effective hardness slope proportionally increased. (~700) Plateau initiating stress increased (~2)

** NAC – No Appreciable Change.

NA -- Not Applicable.

HSH -- Hardening-Softening-Hardening type flow stress function.

Appendix B

Image Analysis Protocol

In the experimental compression tests reported in Chapter 4, the experiments were carried out by Dr. Siddhartha Pathak, and the experimental analysis was carried out together. The image analysis and following sections were carried out under collaboration with Dr. Siddhartha Pathak and Elizabeth Decolvenaere. Further details on the methodology and reliability of such testing methods are given under this section. Figure B1 shows the details of the protocol followed for the image analysis on the VACNT micro-pillars. During imaging, the samples were tilted to 30° with respect to the direction of the electron beam and 9-10 images at evenly spaced intervals were taken along the height of each pillar, as shown in Fig B1a. The imaging conditions were fixed at 100 kX magnification, 10 kV accelerating voltage, at a working distance of 6 mm. This allowed a large enough representative area of the VACNT forest to be imaged while maintaining an adequate resolution of the individual CNTs and bundles. Further attention is needed during image-capture since subsequent analysis of the images by the Canny algorithm [89] requires that the intensity spectrum of the images be captured in its entirety. This was achieved by maintaining a constant contrast value for all of the images along the sample height. Only the brightness was adjusted (if needed) in order to ensure that the intensity spectrum was not clipped off.

To avoid any loss in resolution due to the 30° tilt of the samples, only the central 10% of each image was used for image analysis, as demonstrated in Figs. B1c and e. Each image was first converted to grayscale (Figs. B1b and c), and then analyzed using edge detection technique.

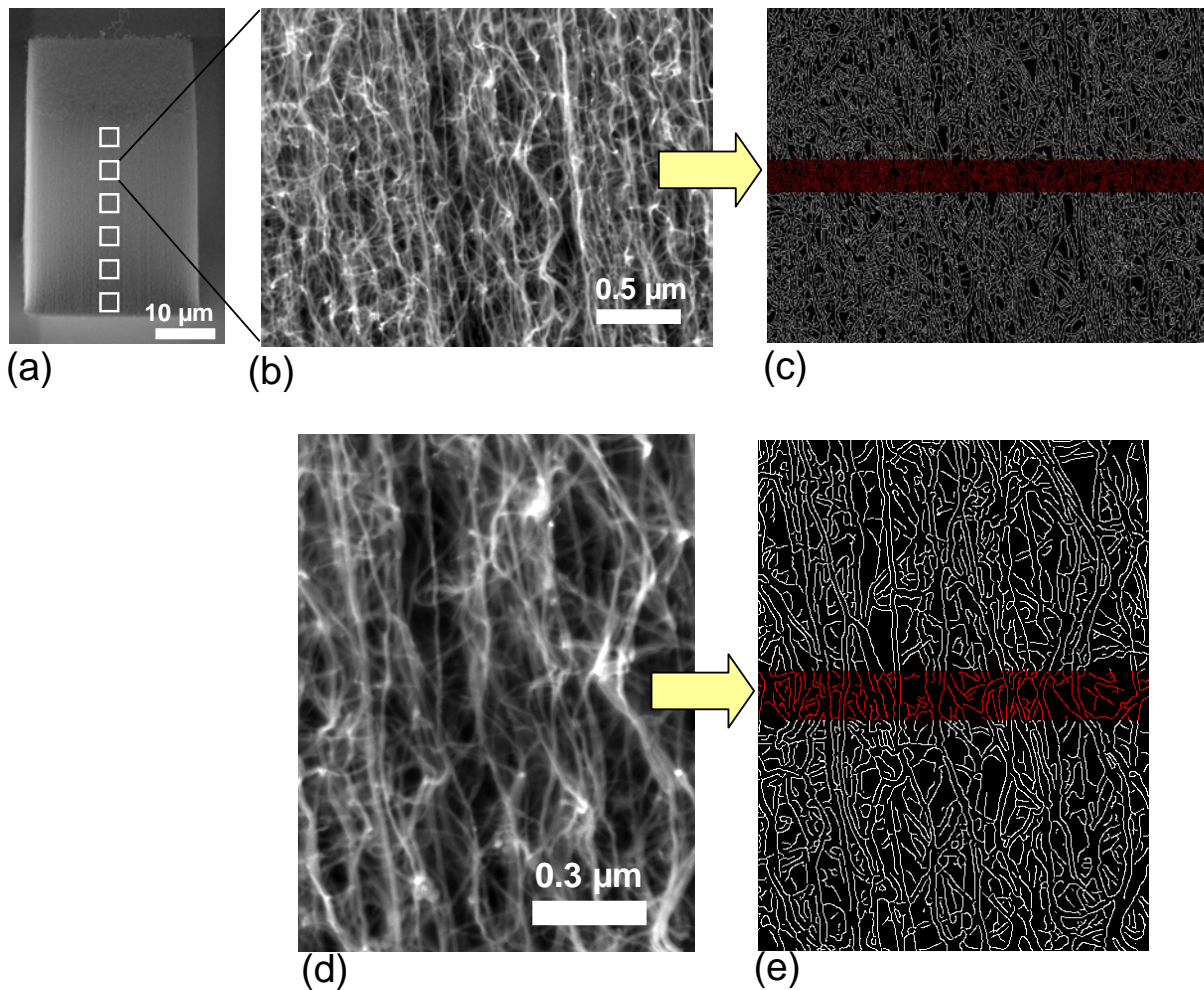


Figure B1. (a) For image analysis 9-10 images at evenly spaced intervals were taken along the height of each pillar. To compute the CNT number density, each captured image (b) was converted to grayscale, and the edges were isolated using the Canny algorithm [89] (c). A magnified version is shown in (d) and (e). To avoid any loss in resolution due to the 30° tilt of the samples, only the central 10% of each image was used for image analysis, as demonstrated by the red strips in (c) and (e). The SEM images were taken at a 30 deg tilt angle

Verification of the Image Analysis Protocol

The efficacy of density as a reliable figure of merit for representing the CNT number density was verified by crosschecking the values obtained from Canny Algorithm with manual counting procedures. For this purpose, a series of

additional SEM images of the same samples were taken at a higher magnification of 200 kX and analyzed via the method described in Fig. S2 using a pixel radius of 6. These same images were overlaid with five horizontal lines, and the crossings between these lines and tubes in the images were manually counted. Some examples of this comparison are shown below in Fig. B2.

While there are some differences in the values calculated from the manual counting technique vs. the edge detection algorithm, the trends and the peaks/valleys in the data seem to match pretty well between the two techniques, as shown in Figs. B2a & b. This suggests that the Canny method may represent an accurate approach to determine the relative local tube number density variation within the same sample.

The repeatability of our image analysis techniques is also a concern, since a slight change in the session-to-session SEM imaging conditions can potentially cause a large variation in ζ . Moreover the edge-detection algorithm works only at a high enough magnification where individual CNTs can be resolved. Thus a site-to-site variation in the ζ values is also a possibility if a very high magnification is used. In order to assuage both these concerns a multi-day imaging protocol was followed, where the same pillar was imaged over different SEM sessions (over multiple days). Images taken over multiple days displayed the same trends Fig. B3. It is interesting to note that while the absolute numbers do vary somewhat between the two data-sets (as is expected), both datasets show the same sudden drop at around a pillar height of 25 μm .

Moreover in this work the reported data (shown in Figure 8(a & b), of the thesis) has been averaged over 3 pillar sets for each case. This averaging is expected to mitigate any minor fluctuations in the individual datasets. Data was obtained from over 60 images on 6 pillars in this work via the image analysis technique described above, and the consistent nature of these values strongly

suggests that the observed trends are real. The image analysis was not taken forward for all the sets of pillars due to a variety of issues needed to be taken care of to maintain the consistency of the image contrast, intensity spectrum etc.

The image analysis technique was also applied across the width of the VACNT pillars. As shown in Fig. B4, the absolute tube number counts are more or less constant – they range within 80-85 counts – across the width of the imaged square pillar. This ensures that there are no significant variations in the values of ζ in the lateral direction.

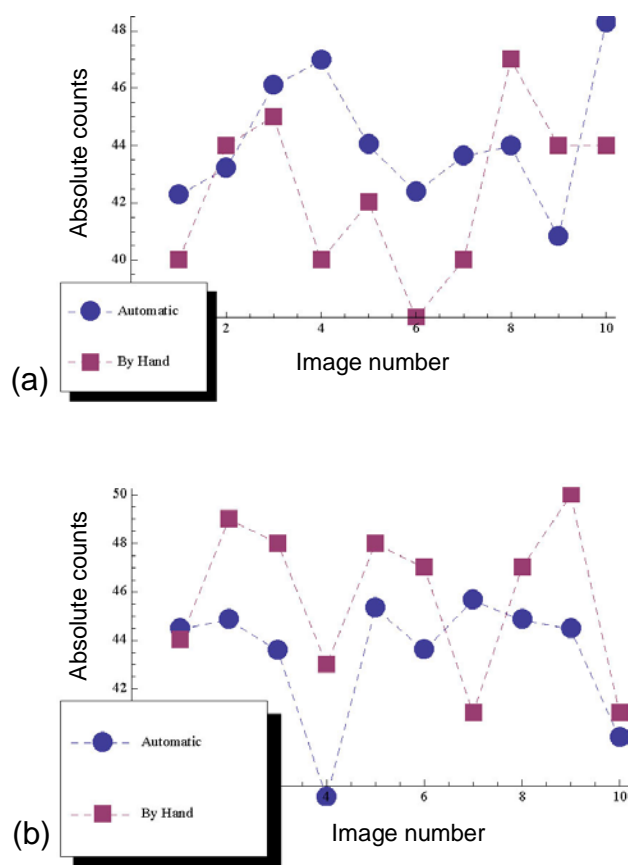


Figure B2. Crosschecking the values obtained using the edge detection technique vs. manual counting procedures for (a) pillars on the substrate interior and (b) pillars on substrate edge. The x-axis denotes the image numbers along the pillar height where image #1 is at the top of the pillar and #10 is at the bottom. Note that these counts are just for a set of 10 images over the height which does not cover the whole height of the pillar.

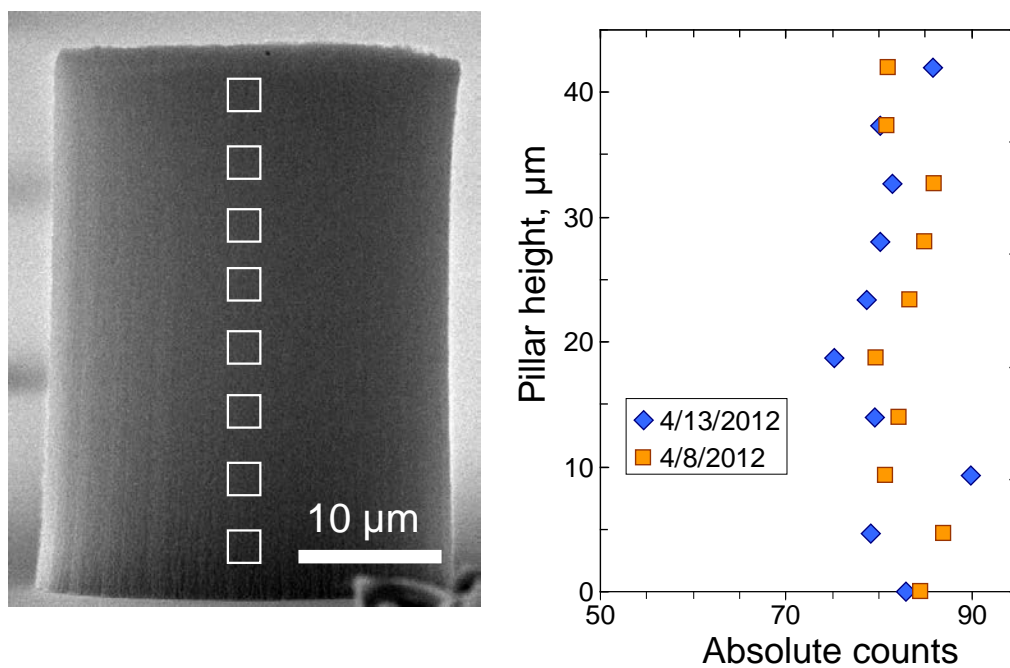


Figure B3. Results of the edge detection technique over different SEM sessions on two different days from SEM images taken along the pillar height, for the circular pillars.

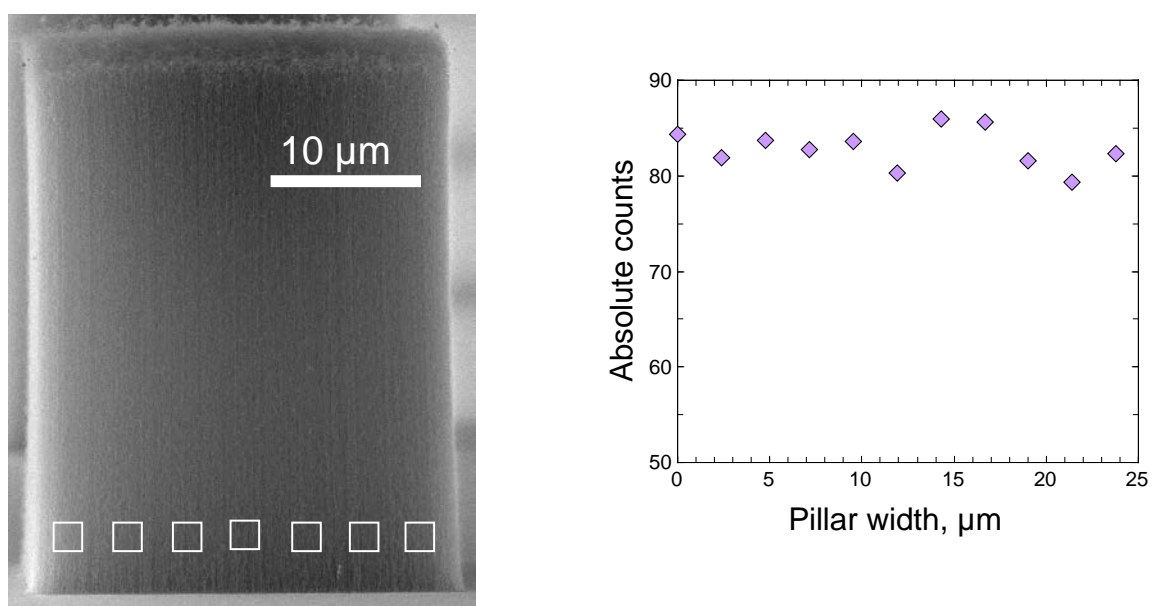


Figure B4. Variations in the absolute tube number counts across the lateral width of a pillar of square cross-section located on the edge of the Si substrate

Relationship Between The Location Of The VACNT Micro-Pillar On The Substrate To Its Deformation Morphology And Stress-Strain Response

Although two distinct pillar cross-sectional shapes (square and circular) are shown, these different shapes do not appear to have any major influence on the mechanical behavior of the VACNTs (see Fig. S8). Rather the relative location of the VACNTs on the Si substrate was found to play a more key role in their resulting morphologies. This effect is demonstrated in Figs. B5 and B6 below.

In terms of their buckling behavior and the general shape of their stress-strain curves, two distinct classifications were noticed: “pillars on substrate edge” and “pillars in substrate interior”. The pillars on the substrate edge had a bottom-to-top buckling sequence, with the top buckle forming last, and a positively sloped plateau in their stress strain curve. On the other hand the buckling sequence for the pillars in the interior of the substrate was markedly different, with the bottom buckles forming last, and the plateau region in their stress-strain curve was also nominally flat (see Figure 8).

In terms of the location on the substrate, the “pillars on substrate edge” classification was confined to only the three rows of pillars at the extreme edge of substrate (a total of 51 pillars, three rows of 17 pillars each, Fig B6b, marked in red). Co-incidentally these pillars were square in cross-section. All the remaining pillars (including the remaining square pillars which were situated in a slightly more interior location as shown in Fig B6c, and the circular pillars shown in Fig. S9d) showed a deformation behavior characteristic of the “pillars in substrate interior” type. A total of 114 pillars showed the “pillars in substrate interior” behavior – including 34 pillars of square cross section (Fig. B6c, marked in blue) and all pillars of circular cross section (Fig. B6d, marked in green).

The square pillars on the edge of the substrate (Fig. B6b) show a sequential bottom-to-top buckling pattern as described in the manuscript (see Figure 8), where the first buckle is nucleated close to the substrate and each subsequent buckle initiates above the previous one. If the sample is unloaded from a maximum compression of $\sim 70\%$ strain, the top third of the pillar remains virtually unscathed (Fig. B6b, left panel), and the buckle closest to the pillar-top is always the last one to form (Fig. B6b, middle panel). The stress-strain signatures of these pillars show a heavily sloped plateau region. This leads to the presumption that the density profiles of all of these pillars would look similar, though only three of them were processed through image analysis. All three of them show consistent trend of upper half having a higher density and also show similar stress-strain trend explained above. Hence this upper half higher density trend is taken to be consistent for all pillars on the edge samples showing this distinct stress-strain behavior.

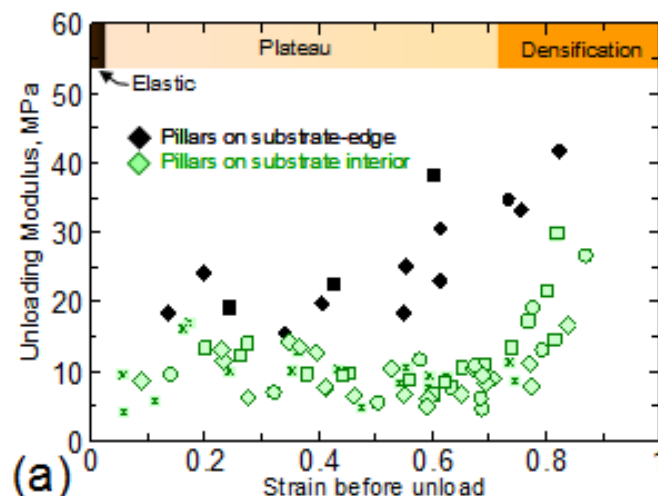
However a different deformation signature is observed for the pillar sets on the substrate-interior (Figs. B6c and d). For these pillars the buckling no longer starts at the bottom – rather when unloaded from $\sim 70\%$ strain the bottom is completely unscathed and undeformed. For both these pillar sets, the fold at the pillar bottom (closest to the substrate) is the last buckle to form. Note also the similarity of the stress-strain response and the flatness of the plateau region between these two pillar sets shown in Figs. B6c and d, as well as their higher recovery as compared to those shown in Fig. B6b. It is worthwhile to reiterate here that both of the pillar-sets in Figs. B6c and d show a very similar response in spite of the obvious differences in their cross-sectional shape (square vs. circular).

Figure B5c shows the comparison between the pillars of square vs. circular cross section as a function of location on the substrate. All pillars shown in this figure are located in the substrate-interior. As evident from this figure, there are no

major differences between the pillars based on their cross-sectional shape. When located in the substrate-interior, pillars of both cross-sections show a similar range of plateau stress values (0.15 – 0.3 MPa), with the plateau stresses showing an increasing trend with faster loading rates.

In all the samples tested, we did not find any significant difference between the deformations of the square vs. circular pillars within the “pillars in substrate interior” type. The significant difference in the mechanical response was observed between the pillars located on the substrate edge, which happened to have square cross-sections, and those in the substrate interior, which had both square and circular cross-sections.

We note that literature reports have shown buckling initiation in VACNT micro-pillars to be dictated by a combination between the local stress distribution (influenced by the shape) and the local density [90]. However as seen from Fig.B6, for this current work the shape of the pillar cross-sections can be ruled out as a potential reason for their differences in mechanical behavior and deformation morphology. Thus it is reasonable to believe here that the key distinction between the various pillar types is in their local density and its variation along the pillar height, which is apparently affected by their relative locations on the substrate. We hypothesize that the neighborhood effect, i.e. the effect of having another VACNT growth nearby, has a marked effect on their density during synthesis. More work is needed to determine the exact cause of these interesting synthesis effects.



(b)	Pre-densification (plateau) regime	Post-densification regime
Pillars on substrate-edge	$R = 63.4 \pm 4.1\%$	$R = 39.8 \pm 3.9\%$
Pillars on substrate interior	$R = 65.6 \pm 1.4\%$	$R = 57.9 \pm 0.9\%$

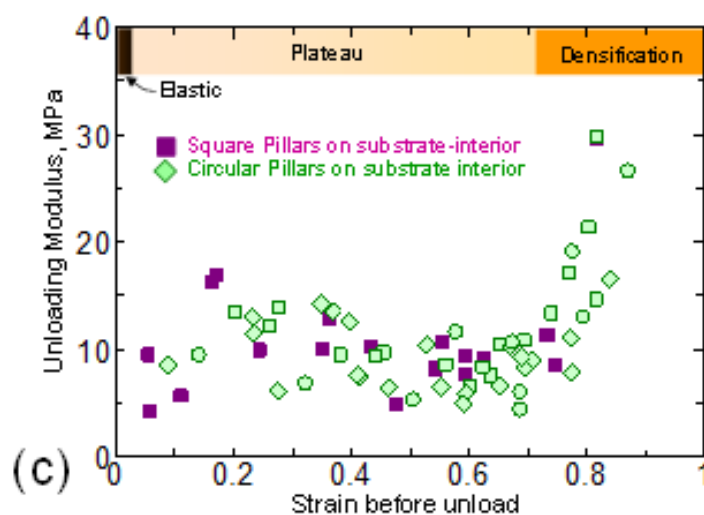


Figure B5. (a) Changes in the unloading modulus at varying maximum strains for the pillars on substrate edge vs. on substrate-interior showing a response similar to their respective stress-strain behavior. Tests across three loading rates 1000 nm/s (squares), 100 nm/s (diamonds) and 10nm/s (circles) are shown in this figure. (b) Table showing the % recovery (R) values in the two pillar types in their pre- and post-densification regimes. Note that the pillars on the substrate-edge were of square cross-section, while those on substrate interior includes data for both square and circular cross-sections.

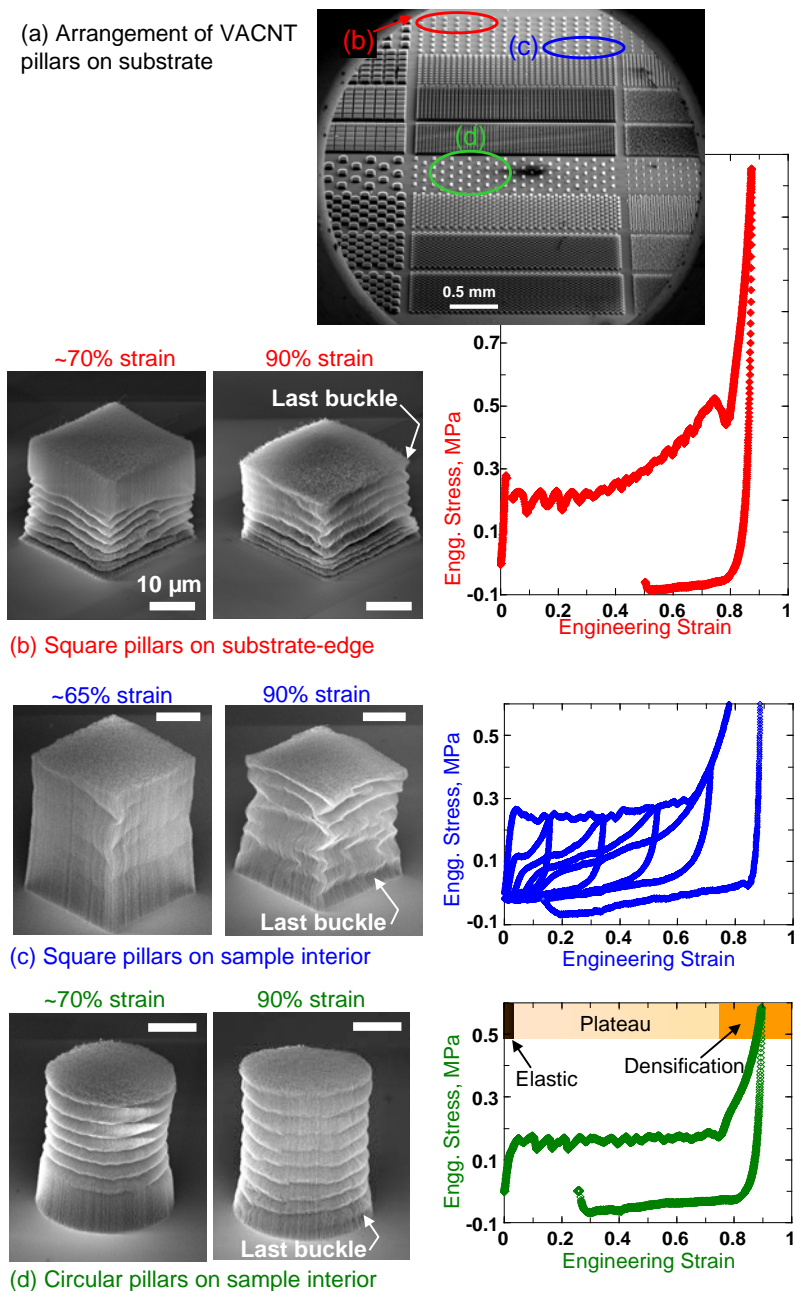


Figure B6. (a) Relative locations of the three pillar sets on the Si substrate. (b) The three rows of pillars (of square cross-section) located towards the edge of substrate show a sequential bottom-to-top buckling pattern where the top buckles are the last to form. Their stress-strain curves show a positively sloped plateau region. On the other hand all other pillar sets located on the substrate-interior, including those marked in (c) square and (d) circular pillars, showed a distinctly different buckling behavior, where the bottom buckle is the last one to form. These pillars show a flat (~zero slope) plateau region, as well as higher recovery as compared to (a). The SEM images were taken at a 60 deg tilt angle.

Bibliography

- [1] B. J. Alder and T. E. Wainwright, "Phase Transition for a Hard Sphere System," *The Journal of Chemical Physics*, vol. 27, pp. 1208-1209, 1957.
- [2] M. F. A. Lorna J. Gibson, "Cellular Solids: Structure and Properties " *Cambridge Solid State Science Series*, 1999.
- [3] W. Bradley, L. Brian, and R. Ryne, "High Radiation Tolerance of Carbon Nanotube Matrices for Space Power Applications," in *2nd International Energy Conversion Engineering Conference*, ed: American Institute of Aeronautics and Astronautics, 2004.
- [4] S. B. Hutchens, A. Needleman, and J. R. Greer, "Analysis of uniaxial compression of vertically aligned carbon nanotubes," *Journal of the Mechanics and Physics of Solids*, vol. 59, pp. 2227-2237, 10// 2011.
- [5] S. B. Hutchens, L. J. Hall, and J. R. Greer, "In situ Mechanical Testing Reveals Periodic Buckle Nucleation and Propagation in Carbon Nanotube Bundles," *Advanced Functional Materials*, vol. 20, pp. 2338-2346, 2010.
- [6] D. S. P. a. D. S. B. Hutchens, *personal communication*, 2011.
- [7] J. T. M. D. H. a. C. A. Brebbia., "Surface Effects and Contact Mechanics XI," *WIT Transactions on Engineering Sciences*, vol. 78, p. 336, 2013.
- [8] K. L. Johnson, "The correlation of indentation experiments," *Journal of the Mechanics and Physics of Solids*, vol. 18, pp. 115-126, 4// 1970.
- [9] A. F. Bower, "Applied Mechanics of Solids," *CRC Press*, 2009.
- [10] D. C. B. U. P. R. Drucker. (1957). *A DEFINITION OF STABLE INELASTIC MATERIAL*. Available: <http://handle.dtic.mil/100.2/AD143756>
- [11] T. B. Stoughton and J. W. Yoon, "Review of Drucker's postulate and the issue of plastic stability in metal forming," *International Journal of Plasticity*, vol. 22, pp. 391-433, 3// 2006.
- [12] M. Hütter, D. J. A. Senden, and T. A. Tervoort, "Comment on the use of the associated flow rule for transversely isotropic elasto-viscoplastic materials," *International Journal of Plasticity*, vol. 51, pp. 132-144, 12// 2013.

- [13] A. Cao, P. L. Dickrell, W. G. Sawyer, M. N. Ghasemi-Nejhad, and P. M. Ajayan, "Super-Compressible Foamlike Carbon Nanotube Films," *Science*, vol. 310, pp. 1307-1310, 2005.
- [14] L. Ge, S. Sethi, L. Ci, P. M. Ajayan, and A. Dhinojwala, "Carbon nanotube-based synthetic gecko tapes," *Proceedings of the National Academy of Sciences*, vol. 104, pp. 10792-10795, 2007.
- [15] L. F. Boesel, C. Greiner, E. Arzt, and A. del Campo, "Gecko-Inspired Surfaces: A Path to Strong and Reversible Dry Adhesives," *Advanced Materials*, vol. 22, pp. 2125-2137, 2010.
- [16] S. Pathak, Z. G. Cambaz, S. R. Kalidindi, J. G. Swadener, and Y. Gogotsi, "Viscoelasticity and high buckling stress of dense carbon nanotube brushes," *Carbon*, vol. 47, pp. 1969-1976, 7// 2009.
- [17] M. Xu, D. N. Futaba, T. Yamada, M. Yumura, and K. Hata, "Carbon Nanotubes with Temperature-Invariant Viscoelasticity from -196° to 1000°C ," *Science*, vol. 330, pp. 1364-1368, 2010.
- [18] SuhrJ, VictorP, CiL, SreekalaS, ZhangX, NalamasuO, *et al.*, "Fatigue resistance of aligned carbon nanotube arrays under cyclic compression," *Nat Nano*, vol. 2, pp. 417-421, 07//print 2007.
- [19] J. R. Raney, F. Fraternali, A. Amendola, and C. Daraio, "Modeling and in situ identification of material parameters for layered structures based on carbon nanotube arrays," *Composite Structures*, vol. 93, pp. 3013-3018, 10// 2011.
- [20] A. Misra, J. R. Greer, and C. Daraio, "Strain Rate Effects in the Mechanical Response of Polymer-Anchored Carbon Nanotube Foams," *Advanced Materials*, vol. 21, pp. 334-338, 2009.
- [21] C. Daraio, V. F. Nesterenko, S. Jin, W. Wang, and A. M. Rao, "Impact response by a foamlike forest of coiled carbon nanotubes," *Journal of Applied Physics*, vol. 100, pp. -, 2006.
- [22] A. D. Mulliken and M. C. Boyce, "Mechanics of the rate-dependent elastic-plastic deformation of glassy polymers from low to high strain rates," *International Journal of Solids and Structures*, vol. 43, pp. 1331-1356, 3// 2006.
- [23] V. S. Deshpande and N. A. Fleck, "Isotropic constitutive models for metallic foams," *Journal of the Mechanics and Physics of Solids*, vol. 48, pp. 1253-1283, 6/1/ 2000.
- [24] A. Qiu, D. F. Bahr, A. A. Zbib, A. Bellou, S. D. Mesarovic, D. McClain, *et al.*, "Local and non-local behavior and coordinated buckling of CNT turfs," *Carbon*, vol. 49, pp. 1430-1438, 4// 2011.
- [25] F. Fraternali, T. Blesgen, A. Amendola, and C. Daraio, "Multiscale mass-spring models of carbon nanotube foams," *Journal of the Mechanics and Physics of Solids*, vol. 59, pp. 89-102, 1// 2011.
- [26] T. Blesgen, F. Fraternali, J. R. Raney, A. Amendola, and C. Daraio, "Continuum limits of bistable spring models of carbon nanotube arrays accounting for material damage," *Mechanics Research Communications*, vol. 45, pp. 58-63, 10// 2012.
- [27] B. I. Yakobson, C. J. Brabec, and J. Bernholc, "Nanomechanics of Carbon Tubes: Instabilities beyond Linear Response," *Physical Review Letters*, vol. 76, pp. 2511-2514, 04/01/ 1996.

- [28] C. Q. Ru, "Effective bending stiffness of carbon nanotubes," *Physical Review B*, vol. 62, pp. 9973-9976, 10/15/ 2000.
- [29] J. B. E. M. A. Duchaineau, A. V. Hamza, T. Dittrich, T. Diaz de la Rubia, Farid F. Abraham, "Compaction dynamics of metallic nano-foams: A molecular dynamics simulation study," *cond-mat.mtrl-sci*, vol. 1, p. 7, 2011.
- [30] L. K. Hu YG, Wang Q., "Nonlocal continuum model and molecular dynamics for free vibration of single-walled carbon nanotubes.," *J Nanosci Nanotechnol.* , vol. 11, p. 7, 2011.
- [31] S. Root, T. A. Haill, J. M. D. Lane, A. P. Thompson, G. S. Grest, D. G. Schroen, *et al.*, "Shock compression of hydrocarbon foam to 200 GPa: Experiments, atomistic simulations, and mesoscale hydrodynamic modeling," *Journal of Applied Physics*, vol. 114, pp. -, 2013.
- [32] A. A. Zbib, S. D. M. , E. T. L. , D. M. , and J. J. , D F Bahr, "The coordinated buckling of carbon nanotube turfs under uniform compression," *Nanotechnology*, vol. 19, p. 7, 2008.
- [33] X. Yang, P. He, and H. Gao, "Competing elastic and adhesive interactions govern deformation behaviors of aligned carbon nanotube arrays," *Applied Physics Letters*, vol. 101, pp. -, 2012.
- [34] C. Chen, T. J. Lu, and N. A. Fleck, "Effect of imperfections on the yielding of two-dimensional foams," *Journal of the Mechanics and Physics of Solids*, vol. 47, pp. 2235-2272, 9// 1999.
- [35] M. A. Di Prima, K. Gall, D. L. McDowell, R. Guldborg, A. Lin, T. Sanderson, *et al.*, "Deformation of epoxy shape memory polymer foam: Part II. Mesoscale modeling and simulation," *Mechanics of Materials*, vol. 42, pp. 315-325, 3// 2010.
- [36] M. S. Nathanael Durr, "Mesoscale modeling of failure in partially sintered metals and homogenisation to macroscale," *LS-DYNA Forum*, p. 12, 2010.
- [37] H. Mae, M. Omiya, and K. Kishimoto, "Effects of strain rate and density on tensile behavior of polypropylene syntactic foam with polymer microballoons," *Materials Science and Engineering: A*, vol. 477, pp. 168-178, 3/25/ 2008.
- [38] M. M. J. Treacy, T. W. Ebbesen, and J. M. Gibson, "Exceptionally high Young's modulus observed for individual carbon nanotubes," *Nature*, vol. 381, pp. 678-680, 06/20/print 1996.
- [39] S. A. M. Leton C. Saha, and Joonkyung Jang, "Molecular Dynamics Simulation Study on the Carbon Nanotube Interacting with a Polymer," *Molecular Dynamics Simulation Study on the Carbon Nanotube*, vol. 33, p. 4, 2012.
- [40] Y. X. a. J. J. V. Xi Chen, "Novel technique for measuring the mechanical properties of porous materials by nanoindentation," *Journal of Materials Research* vol. 21, p. 10, 2005.
- [41] H. J. Qi, K. B. K. Teo, K. K. S. Lau, M. C. Boyce, W. I. Milne, J. Robertson, *et al.*, "Determination of mechanical properties of carbon nanotubes and vertically aligned carbon nanotube forests using nanoindentation," *Journal of the Mechanics and Physics of Solids*, vol. 51, pp. 2213-2237, 11// 2003.

- [42] W. C. O. a. G. M. Pharr, "Measurement of hardness and elastic modulus by instrumented indentation: Advances in understanding and refinements to methodology," *Journal of Materials Research*, vol. 19, p. 17, 2004.
- [43] M. F. Doerner and W. D. Nix, "A method for interpreting the data from depth-sensing indentation instruments," *Journal of Materials Research*, vol. 1, pp. 601-609, 1986.
- [44] Y. Lu and D. M. Shinozaki, "Microindentation testing of inhomogeneous microstructures in welded polyethylene," *Polymer Engineering & Science*, vol. 37, pp. 1815-1824, 1997.
- [45] H. Radhakrishnan, S. D. Mesarovic, A. Qiu, and D. F. Bahr, "Phenomenological constitutive model for a CNT turf," *International Journal of Solids and Structures*, vol. 50, pp. 2224-2230, 7// 2013.
- [46] J. Wang, T. Kemper, T. Liang, and S. B. Sinnott, "Predicted mechanical properties of a coiled carbon nanotube," *Carbon*, vol. 50, pp. 968-976, 3// 2012.
- [47] C. Tekog̃lu, L. J. Gibson, T. Pardoen, and P. R. Onck, "Size effects in foams: Experiments and modeling," *Progress in Materials Science*, vol. 56, pp. 109-138, 2// 2011.
- [48] M. Mazière and S. Forest, "Strain gradient plasticity modeling and finite element simulation of Lüders band formation and propagation," *Continuum Mechanics and Thermodynamics*, pp. 1-22, 2013/12/29 2013.
- [49] F. C. Bardi, H. D. Yun, and S. Kyriakides, "On the axisymmetric progressive crushing of circular tubes under axial compression," *International Journal of Solids and Structures*, vol. 40, pp. 3137-3155, 6// 2003.
- [50] M. Kuroda and V. Tvergaard, "A phenomenological plasticity model with non-normality effects representing observations in crystal plasticity," *Journal of the Mechanics and Physics of Solids*, vol. 49, pp. 1239-1263, 6// 2001.
- [51] T. Belytschko, R. L. Chiapetta, and H. D. Bartel, "Efficient large scale non-linear transient analysis by finite elements," *International Journal for Numerical Methods in Engineering*, vol. 10, pp. 579-596, 1976.
- [52] J. G. Crose and H. H. Fong, "Finite element analysis of a finite-strain plasticity problem," *Nuclear Engineering and Design*, vol. 78, pp. 389-404, 4/2/ 1984.
- [53] A. Needleman, "Material rate dependence and mesh sensitivity in localization problems," *Computer Methods in Applied Mechanics and Engineering*, vol. 67, pp. 69-85, 3// 1988.
- [54] D. Peirce, C. F. Shih, and A. Needleman, "A tangent modulus method for rate dependent solids," *Computers & Structures*, vol. 18, pp. 875-887, // 1984.
- [55] J. Mandel, "Conditions de Stabilité et Postulat de Drucker," in *Rheology and Soil Mechanics / Rhéologie et Mécanique des Sols*, J. Kravtchenko and P. Sirieys, Eds., ed: Springer Berlin Heidelberg, 1966, pp. 58-68.

- [56] J. A. Åström, A. V. Krasheninnikov, and K. Nordlund, "Carbon Nanotube Mats and Fibers with Irradiation-Improved Mechanical Characteristics: A Theoretical Model," *Physical Review Letters*, vol. 93, p. 215503, 11/17/ 2004.
- [57] L. Y. Berhan, Y. B.; Sastry, A. M, "Effect of nanorope waviness on the effective moduli of nanotube sheets," *Journal of Applied Physics*, vol. 95, p. 8, 2014.
- [58] P. D. Bradford, X. Wang, H. Zhao, and Y. T. Zhu, "Tuning the compressive mechanical properties of carbon nanotube foam," *Carbon*, vol. 49, pp. 2834-2841, 7// 2011.
- [59] C. M. McCarter, R. F. Richards, S. D. Mesarovic, C. D. Richards, D. F. Bahr, D. McClain, *et al.*, "Mechanical compliance of photolithographically defined vertically aligned carbon nanotube turf," *Journal of Materials Science*, vol. 41, pp. 7872-7878, 2006/12/01 2006.
- [60] H. Malik, K. J. Stephenson, D. F. Bahr, and D. P. Field, "Quantitative characterization of carbon nanotube turf topology by SEM analysis," *Journal of Materials Science*, vol. 46, pp. 3119-3126, 2011/05/01 2011.
- [61] S. Pathak, N. Mohan, P. P. S. S. Abadi, S. Graham, B. A. Cola, and J. R. Greer, "Compressive response of vertically aligned carbon nanotube films gleaned from in situ flat-punch indentations," *Journal of Materials Research*, vol. 28, pp. 984-997, 2013.
- [62] S. Pathak, E. J. Lim, P. Pour Shahid Saeed Abadi, S. Graham, B. A. Cola, and J. R. Greer, "Higher Recovery and Better Energy Dissipation at Faster Strain Rates in Carbon Nanotube Bundles: An in-Situ Study," *ACS Nano*, vol. 6, pp. 2189-2197, 2012/03/27 2012.
- [63] S. Pathak, N. Mohan, E. Decolvenaere, A. Needleman, M. Bedewy, A. J. Hart, *et al.*, "Local Relative Density Modulates Failure and Strength in Vertically Aligned Carbon Nanotubes," *ACS Nano*, vol. 7, pp. 8593-8604, 2013/10/22 2013.
- [64] M. S. P. Shaffer, X. Fan, and A. H. Windle, "Dispersion and packing of carbon nanotubes," *Carbon*, vol. 36, pp. 1603-1612, 11// 1998.
- [65] L. Ghasemi-Mobarakeh, D. Semnani, and M. Morshed, "A novel method for porosity measurement of various surface layers of nanofibers mat using image analysis for tissue engineering applications," *Journal of Applied Polymer Science*, vol. 106, pp. 2536-2542, 2007.
- [66] S. B. H. A. Needleman, N. Mohan, J. R. Greer, "Deformation of plastically compressible hardening-softening-hardening solids," *Acta Mechanica Sinica*, pp. 1115-1124, 2012-08-25 2012.
- [67] Y. S. Tomo Takeda , Fumio Narita and Yuya Mito, "Tensile Characterization of Carbon Nanotube-Reinforced Polymer Composites at Cryogenic Temperatures: Experiments and Multiscale Simulations," *MATERIALS TRANSACTIONS*, vol. 50, p. 9, 2009.
- [68] Z. W. Pan, S. S. Xie, L. Lu, B. H. Chang, L. F. Sun, W. Y. Zhou, *et al.*, "Tensile tests of ropes of very long aligned multiwall carbon nanotubes," *Applied Physics Letters*, vol. 74, pp. 3152-3154, 1999.
- [69] e. a. Chunyu Li., "Modeling of carbon nanotube clamping in tensile tests," *Composites Science and Technology* vol. 65, p. 8, 2005.

- [70] A. Considère, "L'Emploi du fer et de l'acier," *Ann. Ponts Chaussées*, vol. 9, p. 201, 1885.
- [71] R. Abeyaratne and J. K. Knowles, "A continuum model of a thermoelastic solid capable of undergoing phase transitions," *Journal of the Mechanics and Physics of Solids*, vol. 41, pp. 541-571, 3// 1993.
- [72] J. W. Hutchinson and K. W. Neale, "Influence of strain-rate sensitivity on necking under uniaxial tension," *Acta Metallurgica*, vol. 25, pp. 839-846, 8// 1977.
- [73] R. James, "Co-existent phases in the one-dimensional static theory of elastic bars," *Archive for Rational Mechanics and Analysis*, vol. 72, pp. 99-140, 1979/06/01 1979.
- [74] A. Needleman, "Plastic strain localization in metals," *Integration of material, process and product design*
Symposium, Integration of material, process and product design, p. 12, 1999.
- [75] N. Mohan, J. Cheng, J. R. Greer, and A. Needleman, "Uniaxial Tension of a Class of Compressible Solids With Plastic Non-Normality," *Journal of Applied Mechanics*, vol. 80, pp. 040912-040912, 2013.
- [76] J. W. Hutchinson and K. W. Neale, "Neck propagation," *Journal of the Mechanics and Physics of Solids*, vol. 31, pp. 405-426, // 1983.
- [77] and J. W. Hutchinson, Miles, J. P., "Bifurcation analysis of the onset of necking in an elastic/plastic cylinder under uniaxial tension," *J. Mech. Phys. Solids*, vol. 22, p. 10, 1974.
- [78] V. Ballarin, A. Perlade, X. Lemoine, O. Bouaziz, and S. Forest, "Mechanisms and Modeling of Bake-Hardening Steels: Part II. Complex Loading Paths," *Metallurgical and Materials Transactions A*, vol. 40, pp. 1375-1382, 2009/06/01 2009.
- [79] J. W. Rudnicki, and Rice, J. R., "Bifurcation Analysis of the Onset of Necking in an Elastic/Plastic Cylinder Under Uniaxial Tension," *J. Mech. Phys. Solids*, vol. 23, p. 23, 1975.
- [80] V. Ballarin, M. Soler, A. Perlade, X. Lemoine, and S. Forest, "Mechanisms and Modeling of Bake-Hardening Steels: Part I. Uniaxial Tension," *Metallurgical and Materials Transactions A*, vol. 40, pp. 1367-1374, 2009/06/01 2009.
- [81] S. B. Hutchens, A. Needleman, and J. R. Greer, "Erratum to "Analysis of uniaxial compression of vertically aligned carbon nanotubes" [Journal of the Mechanics and Physics of Solids 59 (2011) 2227–2237]," *Journal of the Mechanics and Physics of Solids*, vol. 60, pp. 1753-1756, 10// 2012.
- [82] A. Jung, S. Diebels, A. Koblischka-Veneva, J. Schmauch, A. Barnoush, and M. R. Koblischka, "Microstructural Analysis of Electrochemical Coated Open-Cell Metal Foams by EBSD and Nanoindentation," *Advanced Engineering Materials*, vol. 16, pp. 15-20, 2014.

- [83] V. Tvergaard and A. Needleman, "Polymer indentation: Numerical analysis and comparison with a spherical cavity model," *Journal of the Mechanics and Physics of Solids*, vol. 59, pp. 1669-1684, 9// 2011.
- [84] A. F. Bower, N. A. Fleck, A. Needleman, and N. Ogbonna, "Indentation of a Power Law Creeping Solid," *Proceedings: Mathematical and Physical Sciences*, vol. 441, pp. 97-124, 1993.
- [85] U. Ramamurty and M. C. Kumaran, "Mechanical property extraction through conical indentation of a closed-cell aluminum foam," *Acta Materialia*, vol. 52, pp. 181-189, 1/5/ 2004.
- [86] J. J. Y. X. Xi Chen; Vlassak, "Novel technique for measuring the mechanical properties of porous materials by nanoindentation," *Journal of Materials Research*, vol. 21, p. 10, 2006.
- [87] H. Tsukahara and T. lung, "Finite element simulation of the Piobert-Luders behavior in an uniaxial tensile test," *Materials Science and Engineering: A*, vol. 248, pp. 304-308, // 1998.
- [88] Y. Lu and D. M. Shinozaki, "Deep penetration micro-indentation testing of high density polyethylene," *Materials Science and Engineering: A*, vol. 249, pp. 134-144, 6/30/ 1998.
- [89] J. Canny, "A computational approach to edge detection," *IEEE Transactions on Pattern Analysis and Machine Intelligence*, vol. PAMI-8, pp. 679-98, 1986.
- [90] M. R. Maschmann, G. J. Ehlert, S. J. Park, D. Mollenhauer, B. Maruyama, A. J. Hart, *et al.*, "Visualizing Strain Evolution and Coordinated Buckling within CNT Arrays by In Situ Digital Image Correlation," *Advanced Functional Materials*, vol. 22, pp. 4686-4695, 2012.